AD-768 919

STRESS WAVE PROPAGATION THROUGH EARTH-
WATER SYSTEMS

Carl J. Constantino

City College Research Foundation

Prepared for:

Advanced Research Projects Agency

September 1973

ARPA Order Number: 1408   Program Code Number: 9F10

Contract Number: DAHC19-69-C-0032

Contractor: The City College Research Foundation

The City College of the City University of New York

Convent Avenue at 138th Street

New York, New York   10031

Title: STRESS WAVE PROPAGATION THROUGH EARTH-WATER SYSTEMS

FINAL REPORT

SEPTEMBER, 1973

Principal Investigator: Professor Carl J. Costantino

212-621-2228

Contract Dates: 1 September 1969 to 31 August 1972

Amount of Contract: $76,123.

i,

TABLE OF CONTENTS

1.0 INTRODUCTION

This report is the final report on Contract No. DAHC 19-69-C-0032 with the Advanced Research Projects Agency entitled "Stress-Wave Propagation Through Earth-Water Systems." The fundamental objective of this study is to develop numerical techniques to treat the general two-dimensional stress wave propagation problem through nonlinear earth materials including the effects of water flow through the earth materials.

Prior to the beginning of this study, a numerical technique was developed to treat the dynamic wave problem through arbitrary nonlinear media (Ref. 5, 6 and 7) without including the effects of water on the propagation process. This numerical approach is based upon the finite element method of analysis and led to the development of a large computer program (termed the SLAM Code for identification, the acronym standing for Stress Waves in Layered Arbitrary Media) to treat either the general axisymmetric or plane (stress or strain) geometric configuration. The finite element approach has been taken in this development to allow the user a general flexibility in treating two dimensional problems of rather complex geometry (inclusions, material layering, complex boundaries, etc.).

The majority of computer codes that have been developed to treat these problems are based upon finite difference formulations and thus would have difficulty in treating complex geometries of interest. In the finite difference formulations, relatively uniform meshes are distributed over the half-space of interest and equations of motions applicable at each node are developed by suitably differencing the system partial differential equations of motion. By contrast, in the finite element formulation, the two dimensional half-space is divided into small, arbitrarily located, small elements, these elements being connected to each other at their vertices or node points. From the element type and geometry, equations of motion are developed for each node. The primary advantage of this method over its counterpart difference formulation thus lies in its flexibility in specifying node distributions for a particular problem. It can then be used to treat problems of as complex a geometry as desired with no change in computer code formulation.

However, this added flexibility is obtained at a cost, this cost being the increased amount of information that must be maintained in the computer (or its auxiliary storage units). Thus to perform a calculation for a simple problem, with, say, a uniform mesh, the finite element formulation will be inefficient as compared to finite differences. For problems where simple mesh formations can be used, the finite element solution will in general take more machine time to achieve the same results as the difference solution. Thus the very flexibility which is its

advantage can be considered a disadvantage for these cases.

After the development of SLAM Code, various problems of interest were investigated to determine the effects of material nonlinearities on the wave propagation process (Ref. 5). In general, three types of problems are of interest wnen studying dynamic processes through earth media. In the first type, the half space is subjected to high intensity pressure loadings caused by high energy explosions. The resulting ground shock effects are highly transient and are characterized by relatively short duration shock waves of high strength. Of particular interest for this problem is the rate of decay of the shock front as it moves through the ground. Clearly, nonlinear properties of the material significantly influence the decay of the shock strength since large non-recoverable volume changes can decrease the peak pressures of the shock front. In the second problem type, the half-space is subjected to long duration low intensity vibratory type loadings associated with earthquake motions. Again nonlinear properties and volume changes of the earth material significantly alter the characteristics of the motion histories sustained at the surface of the ground.

A third type, not often considered with the first two problems, is concerned with the response of near shore structures and soils subjected to ocean storm waves. In these problems nonlinear soil properties as well as induced seepage and pore pressure effects tend to reduce the strengtn of the soil leading to potential massive failures of the soil systems. It is well known (Ref. 11) that storm waves can induce slide failures on even flat

slopes due to the excess seepage conditions developed within the ocean sediments. In these problems, the stress and motion histories sustained at any point in the ground are significantly influenced by the nonlinear characteristics of the materials, associated volume changes and any induced seepage conditions that may occur. Thus, to seriously treat the time dependent response of earth media, the effects of pore water must be suitably taken into account.

In the following section of this report, a brief review of the analytic approach and numerical techniques used to obtain solutions is presented. After this review, the results obtained for four different problem types are presented, these problems being chosen primarily to indicate the areas for which this analysis is applicable. In the first results presented (Section 3.0), quasi-static problems are considered; that is, inertial effects are neglected. The problems are limited to the (time-dependent) two dimensional consolidation situations. This is followed (Section 4.0) by the analysis of stress wave propagation through saturated soil columns to determine the influence of pore fluid on stress wave speed. Sections 5.0 and 6.0 present results obtained for the effects of soil liquefaction generated by ocean storm waves, the first concerning liquefaction of foundation soils and the second concerning embankment stability to the storm waves.

2.0 GOVERNING SYSTEM EQUATIONS

In Ref. 1, the derivation of the system of equations governing both the equilibrium of the nodes as well as pore water migration (seepage) was presented in detail. The basic assumptions made are:

(a) the soil can behave as a nonhomogeneous, aniso-
tropic and inelastic solid;

(b) the pore water is considered as incompressible
with respect to the soil component;

(c) the deformation of the soil depends upon inter-
granular stresses only;

(d) the water flows through the soil according to
D'arcy's law.

For completeness of this report, the derivation of the system equations has been summarized and presented in Appendix A. The system equations can be written symbolically as

$$\{F_u\} \cdot [k_{uu}]\{u\} + [k_{uw}]\{w\} - [\bar{k}_u]\{\pi\}$$

$$\{F_w\} \cdot [k_{wu}]\{u\} + [k_{ww}]\{w\} - [\bar{k}_w]\{\pi\}$$

$$\{P\} \cdot [\bar{k}_u]^T\{\dot{u}\} + [\bar{k}_w]^T\{\dot{w}\} + [H]\{\pi\}$$

(1)

In equations 1, the vectors $\{F_u\}$ and $\{F_w\}$ are the horizontal (u-direction) and vertical (w-direction) forces generated at the nodes of the finite element mesh. The matrices k_{uu}, k_{uw}, k_{wu}, k_{ww}, are the usual elastic stiffness matrices and are used to compute the elastic components of the forces developed at the node points due to the relative displacements of the element nodes. The vectors $\{u\}$ and $\{w\}$ are the horizontal and vertical

2.1

displacements of the nodes of the mesh, while the vector $\{\pi\}$ represents the excess pore pressures developed at the node points. The matrices $\bar{k}_u$ and $\bar{k}_w$ then convert these excess pore pressure into equivalent node point loadings.

The forces at the node points, $\{Fu\}$ and $\{Fw\}$, can have three components, namely,

(a) applied node point loads due to applied pressure loads;

(b) fictitious correction forces to account for nonlinear stress-strain behavior of the soil skeleton;

(c) inertia loadings for dynamic problems.

The forces can then be written as

$$\{F_u\} = \{F_u^A\} + \{F_u^N\} - [M]\{\ddot{u}\}$$
$$\{F_w\} = \{F_w^A\} + \{F_w^N\} - [M]\{\ddot{w}\}$$

(2)

The terms with the superscript A in equation 2 are the horizontal and vertical components of any forces applied to the nodes (from concentrated loads or pressures applied to specific surfaces in the problem). The terms with the superscript N refer to the fictitious correction forces that are applied to the nodes to account for any nonlinearity in material stress-strain behavior (or deviations from the elastic case). The final terms of equation 2 refer to inertia forces if dynamic effects are included.

The first two of equation 1 then represent the equilibrium of total stresses at a point in the half-space. The third equation of equation 1 represents the seepage flow relationship generated from D'arcy's law. The matrix [H] is dependent upon the coefficients of permeability of the material (as well as

properties of the finite element configuration) and the vectors $\{\dot{u}\}$ and $\{\dot{w}\}$ represent the nodal velocities.

The vector $\{P\}$ represents the rate of volume change of the fluid component associated with each node point. For incompressible fluid, these components are zero for interior node points (all fluid that flows into an element must flow out), while for some boundary node points (for which the excess pore pressure is specified), these components indicate the volume of water flowing out of the nodes.

2.1 Solution Procedures

At each node point (except at boundary nodes where either displacements and/or excess pore pressures are specified), three unknowns must be determined at any instant of time, namely the two node displacements (u and w) and the excess pore pressure (π). The solution procedure then depends upon the particular conditions of the problem.

For example, for steady state flow conditions where the coefficients of permeability are assumed to be independent of the intergranular stress (or strain) state, the time variation of the parameters is zero. Referring to equation 1, this allows for a direct solution of the third equation (by elimination procedures, say) for the excess pore pressure distribution. With these as knowns, the first two of equation 1 can then be solved for the node displacement components. If the material is elastic, the nonlinear correction forces of equation 2 are zero so that a single solution is all that is needed. If the material stress-strain relation is nonlinear, the displacement solution must be

iterated upon since the nonlinear correction forces are functions of the node displacements.

For problems in which transient effects are included but for which inertia effects can be neglected (slow transients as in consolidation problems), the following procedure can be used. The velocity intergration procedure is based upon a simple linear velocity approximation during a small time step, or

$$\chi_i = \chi_{i-1} + \frac{\Delta t}{2} (\dot{\chi}_{i-1} + \dot{\chi}_i)$$ (3)

where χ_i represents a displacement at time i, χ_{i-1} the displacement at the preceding time step, $\dot{\chi}_{i-1}$ and $\dot{\chi}_i$ represent the corresponding velocities and Δt is the time increment between i-1 and i. Substituting equation 3 into equation 1 leads to the equations

$$\begin{Bmatrix} F_u \\ F_w \\ G \end{Bmatrix}_i = \begin{bmatrix} k_{uu} & k_{uw} & -\bar{k}_u \\ k_{uw} & k_{ww} & -\bar{k}_w \\ -\bar{k}_u^T & -\bar{k}_w^T & -\frac{\Delta t}{2} H \end{bmatrix} \begin{Bmatrix} u \\ w \\ \pi \end{Bmatrix}_i$$ (4)

where the subscripts i refer to the current times. The "forcing" vector $\{G\}$ can be written as

$$\{G\}_i = -\frac{\Delta t}{2} \left[\{P\}_i + [\bar{k}_u]^T \{\dot{u}_{i-1} + \frac{2}{\Delta t} u_{i-1}\} + [\bar{k}_w]^T \{\dot{w}_{i-1} + \frac{2}{\Delta t} w_{i-1}\} \right]$$ (5)

and is defined in terms of the previous displacement and velocity history. The "stiffness" matrix of equation 4 is symmetric and usual solution procedures can be used.

Considering an elastic porous material, at a particular instant of time, the effective force vector of equation 4 is

2.4

known, since the applied loads are specified and the G-vector can be computed from the previous time step. Obviously, the solution must start from some time when the initial conditions are specified. The unknowns (u, w, π) at the current time can then be obtained by, say, a simple elimination technique. The solution at the following time step can then be obtained using the current solution as input, etc. In this fashion, the solution is marched out in time.

For nonlinear material behavior, this procedure has to be modified since the nonlinear correction forces of equation 2 are also functions of the current displacements. To overcome this situation, an iteration procedure is used at each time step to ensure that the nonlinear correction forces are properly included in the analysis. At each time step, an initial trial solution is obtained by using approximate values for these correction forces (usually the forces from the previous time step), and these are modified by the iteration process.

For problems in which inertia effects are no longer negligible (say, stress wave problems), a similar procedure can be used, except employing a linear acceleration extrapolation procedure, or

$$\dot{x}_i = \dot{x}_{i-1} + \frac{\Delta t}{2}(\ddot{x}_{i-1} + \ddot{x}_i).$$

$$x_i = x_{i-1} + \dot{x}_{i-1}\Delta t + \frac{\Delta t^2}{6}(\ddot{x}_i + 2\ddot{x}_{i-1})$$

(6)

Substituting equation 6 into equations 1 and 2 leads to another implicit integration scheme which can be written as

2.5

$$\left\{\begin{array}{c} F_u^* \\ F_w^* \\ G^* \end{array}\right\}_i = \left[\begin{array}{ccc} (k_{uu} + \frac{6}{\Delta t^2} M) & k_{uw} & -\overline{k}_u \\ k_{wu} & (k_{ww} + \frac{6}{\Delta t^2} M) & -\overline{k}_w \\ -\overline{k}_u^T & -\overline{k}_w^T & -\frac{\Delta t}{3} H \end{array}\right]\left\{\begin{array}{c} u \\ w \\ \pi \end{array}\right\}_i \qquad (7)$$

The "stiffness" matrix of equation 7 is again symmetric and may be solved by simple elimination methods. The forcing functions of equations 7 are defined by

$$\{F_u^*\} = \{F_u^\wedge\} - \{F_u^w\} + [M]\left[\frac{6}{\Delta t^2}\{u\}_{i-1} + \frac{6}{\Delta t}\{\dot{u}_{i-1}\} + 2\{\ddot{u}\}_{i-1}\right]$$

$$\{F_w^*\} = \{F_w^\wedge\} + \{F_w^w\} + [M]\left[\frac{6}{\Delta t^2}\{w\}_{i-1} + \frac{6}{\Delta t}\{\dot{w}\}_{i-1} + 2\{\ddot{w}\}_{i-1}\right]$$

$$\{G^*\} = -\frac{\Delta t}{3}\{P\}_i - [\overline{k}_u]^T\left[\{u\}_{i-1} + \frac{2\Delta t}{3}\{\dot{u}\}_{i-1} + \frac{\Delta t^2}{6}\{\ddot{u}\}_{i-1}\right] \qquad (8)$$
$$\qquad - [\overline{k}_w]^T\left[\{w\}_{i-1} + \frac{2\Delta t}{3}\{\dot{w}\}_{i-1} + \frac{\Delta t^2}{6}\{\ddot{w}\}_{i-1}\right]$$

Again the solution can be marched out in time as before.

A draw back of equation 8 occurs for cases where the time increment required is very small or the mass vector very large. For these situations, the inertia terms of the "stiffness" matrix may become extremely large, masking out the stiffness terms. This in turn may lead to instability in the implicit integration procedures used. For these cases, a modified approach can be used. The third of equation 1 can be solved for the pore pressure vector (requiring an inversion of the H matrix) and this substituted into the remaining two force equations. For this case, the force equations become

$$\{F_u^\wedge\} - \{F_u^w\} = \left([k_{uu}]\{u\} + [k_{uw}]\{w\}\right) + \left([\overline{k}_{uu}]\{\dot{u}\} + [\overline{k}_{uw}]\{\dot{w}\}\right) + [M]\{\ddot{u}\}$$

$$\qquad (9)$$

$$\{F_w^\wedge\} + \{F_w^w\} = \left([k_{wu}]\{u\} + [k_{ww}]\{w\}\right) + \left([\overline{k}_{wu}]\{\dot{u}\} + [\overline{k}_{ww}]\{\dot{w}\}\right) + [M]\{\ddot{w}\}$$

2.6

With this approach, either implicit or explicit integration schemes can be used.

3.0 SOIL TEST CONFIGURATIONS

With the developed computer program, numerical results were generated for several soil configurations similar to the usual soil tests, consolidation and triaxial compression. The first set of data assumed elastic soil behavior, since for these problems analytic solutions are available or can be easily developed for comparison purposes. The first nonlinear soil model investigated made use of a Coulomb-Mohr elastic plastic model based on the concepts of the theory of plasticity.

Although this model is often used, it is not adequate for modeling stress-strain behavior (except in a crude sense) and would be of questionable value when studying pore pressure dependent problems. A more detailed soil model was then investigated which adequately predicts stress strain behavior of a particular sand sample and was developed by fitting the parameters of this model to available experimental data.

3.1 One-Dimensional Elastic Consolidation

The first problem investigated was, naturally, that of the classical one-dimensional consolidation of elastic material. The analytic solution available for comparison is the standard Terzaghi solution (Ref. 2). The problem parameters chosen for the investigation are shown in Figure 1. The computed settlement-time history at the top of the soil surface is shown in Fig. 2 and comparisons made with the exact analytic solution. The excess pore pressures developed at the bottom of the layer are shown in Figure 3

3.1

while those at a point nearer the surface are shown in Figure 4.
Again comparisons are made with the exact solution and in all cases
they show excellent agreement. The pore pressure distribution at
various times through the layer is shown in Figure 5. Since the
pore pressure is assumed to vary linearly within a given element
the distribution curves are piecewise linear. If in the actual
problem the pore pressure variation is sharp, smaller element sizes
must be used to suitably approximate the solution.

3.2 Triaxial Elastic Soil Configuration

The second model considered was the triaxial soil con-
figuration shown in Fig. 6a. The soil model was considered to be
elastic and a 50 psi vertical pressure applied at the initial or
zero time. The finite element model used is shown in Fig. 6b and
consists of 28 rectangular elements to represent the upper quarter
of the triaxial sample. The elements are thus axisymmetric or ring
elements.

To obtain the analytic solution, it was assumed that
strain conditions in the sample are uniform. The initial pore pres-
sure developed in the sample (prior to drainage occurring) is found
from the following analysis. The volume change per unit soil volume
for the elastic soil is

$$\Delta V = \frac{1-2\nu}{E}\left[\bar{\sigma}_r + \bar{\sigma}_\theta + \bar{\sigma}_z\right] \tag{10}$$

where the barred stresses represent the intergranular stresses, and

3.2

E and ν are the elastic modulus and Poisson's ratio, respectively. Since no seepage occurs during the initial conditions, the volume change is zero or

$$\bar{\sigma}_3 = -(\bar{\sigma}_r + \bar{\sigma}_\theta) \tag{11}$$

In addition,

$$\bar{\sigma}_r = \bar{\sigma}_\theta = -p$$

$$\bar{\sigma}_3 + p = \sigma_v \tag{12}$$

where p is the excess pore pressure and σ_v is the vertical applied stress. Combining equations 11 and 12 leads to the solution

$$\bar{\sigma}_3 = 2\sigma_v/3 \tag{13}$$

$$p = \sigma_v/3$$

The initial compression of the soil sample is simply

$$\Delta_i = \frac{2}{3} \frac{\sigma_v l}{E} (1 + \nu) \tag{14}$$

The final stresses in the soil system are obtained when p is zero (no pore pressure) and

$$\bar{\sigma}_r = \bar{\sigma}_\theta = 0$$

$$\bar{\sigma}_3 = \sigma_v \tag{15}$$

while the final compression of the soil sample is

$$\Delta_f = \frac{\sigma_N L}{E} \tag{16}$$

where L is half the original sample height (height of the finite element model). The settlement from the initial condition to the final condition is governed by the one-dimensional consolidation model (since one-dimensional seepage occurs through the top surface only) with the modification that the definition of the coefficient of consolidation is

$$C_N = \frac{k}{\gamma_w} \frac{E}{3(1-2\nu)} \tag{17}$$

The solution to the particular problem of Fig. 6 was obtained numerically using a time increment of 0.1 seconds. The pore pressure distribution along the centerline elements is shown in Fig. 7 together with comparisons with the analytic solution. As can be seen, the comparisons are excellent, except during the early part of the solution. In an attempt to uncover the cause of the discrepancies, the same problem was investigated with differing time increments, and the results are shown in Fig. 8. As may be noted by comparing Figs. 7 and 8, the early time oscillations found for the top element (Element 1) are related to the time step. As the time step is decreased, the oscillations disappear. A comparison with the exact solution shows that the computed solution is slightly lower and this can be attributed to the fact that the pore

3.4

pressure profile is assumed to be linear across the element while the actual pressure profile is curved, particularly at the early times.

The comparison with the middle element (Element 4) is not as clear cut, however. As may be noted from Fig. 8, this pore pressure shows an initial increase in pore pressure before the anticipated decay occurs, and this increase is independent of time increment of the integration. Since this phenomenon did not occur in the elastic plane problem discussed previously, it must be concluded that this variation is concerned with the coarseness of the finite element mesh in the radial direction for this axisymmetric problem. No further numerical studies have been conducted on this problem as yet, however.

3.3 Triaxial Coulomb-Mohr Model

The first triaxial problem including nonlinear material properties that was investigated was the same model shown in Fig. 6 but with nonlinear properties described by the Coulomb-Mohr yield condition (Ref. 3). For stresses within the yield surface, the soil is assumed to behave elastically, where the yield surface is defined by

$$\alpha J_1 + \sqrt{J_2'} = k \tag{18}$$

For the axisymmetric stress condition of interest for this problem,

3.5

$$J_1 = \bar{\sigma}_r + \bar{\sigma}_\theta + \bar{\sigma}_3$$

$$J_2' = \frac{1}{6}\left\{(\bar{\sigma}_r - \bar{\sigma}_\theta)^2 + (\bar{\sigma}_\theta - \bar{\sigma}_3)^2 + (\bar{\sigma}_3 - \bar{\sigma}_r)^2\right\} + \bar{\tau}_{r_3}^2 \qquad (19)$$

where the bar again indicates intergranular stresses. The coefficients (α, k) are related to the usual strength parameters obtained from a triaxial test series, ϕ, the angle of internal friction, and c, the cohesion, by

$$\alpha = \frac{2}{\sqrt{3}} \frac{\sin\phi}{(3 - \sin\phi)}$$

$$\qquad (20)$$

$$k = \frac{6c}{\sqrt{3}} \frac{\cos\phi}{(3 - \sin\phi)}$$

For stresses on the yield surface, plastic strain components are determined from the usual normality principal.

Prior to investigating this problem numerically, the analytic solution for the initial stress condition was obtained (no drainage allowed). As the vertical stress is slowly increased, the soil behaves elastically and the previous solution applies. Substituting equations 12 and 13 into equations 19 yields

$$J_1 = 0$$

$$J_2' = \frac{1}{\sqrt{3}} \sigma_N$$

For plastic yielding to begin, the critical vertical stress must reach the value

$$\sigma_N^y = \sqrt{3}\, k \qquad\qquad (21)$$

For applied stresses larger than this critical value, plastic fl w must be accounted for, making use of the normality relation (Ref. 3), which for this problem becomes

$$\dot{\epsilon}_r^P = \dot{\epsilon}_\theta^P = -\alpha - \frac{1}{6\sqrt{J_2'}}\, (\bar{\sigma}_\partial - \bar{\sigma}_r)$$

$$\dot{\epsilon}_\partial^P = -\alpha + \frac{1}{6\sqrt{J_2'}}\, (\bar{\sigma}_\partial - \bar{\sigma}_r) \qquad\qquad (22)$$

where ($\dot{\epsilon}_r^P$, $\dot{\epsilon}_\partial^P$) are the radial and vertical components of the plastic strain rate vector. The plastic volume change is

$$\Delta V^P = -\frac{3\alpha}{\left(\frac{1}{\sqrt{3}} - \alpha\right)}\, \epsilon_\partial^P \qquad\qquad (23)$$

where ϵ_∂^P is the total plastic vertical strain, while the elastic volume change is

$$\Delta V^e = \left(\frac{1-2\nu}{E}\right)\left(\bar{\sigma}_\partial + 2\bar{\sigma}_r\right) \qquad\qquad (24)$$

Knowing that the total volume change is zero (no drainage out of the sample is allowed), the solution can be readily obtained for any applied stresses greater than the critical, or

3.7

$$\bar{\sigma}_r = -p = \left(\frac{1-\sqrt{3}\alpha}{3\sqrt{3}\alpha}\right)\sigma_N - \frac{k}{3\alpha}$$

$$\bar{\sigma}_z = \left(\frac{1+2\sqrt{3}\alpha}{3\sqrt{3}\alpha}\right)\sigma_N - \frac{k}{3\alpha}$$

$$\epsilon_z^P = \left(\frac{1-\sqrt{3}\alpha}{3\sqrt{3}\alpha}\right)\left(\frac{1-2\nu}{E}\right)(\bar{\sigma}_z + 2\bar{\sigma}_r)$$

$$\epsilon_z^E = \frac{1}{E}\left(\bar{\sigma}_z - 2\nu\bar{\sigma}_r\right) \tag{25}$$

$$\epsilon_z^T = \epsilon_z^E + \epsilon_z^P$$

The results for a particular undrained case are shown in Fig. 9. The vertical pressure is applied "slowly" with a rise time of 50 seconds until it reaches a peak pressure of 50 psi. The particular properties of the soil chosen were

$$E = 1000 \text{ psi}$$
$$\nu = 0.25$$
$$c = 20.8 \text{ psi}$$
$$\phi = 30°$$

For this condition the critical vertical stress is reached when σ_N is 43.4 psi and the corresponding pore pressure is 14.45 psi. As the vertical stress is increased to 50 psi, plastic flow takes place (along with plastic volume expansion) and the pore pressure reduces to 11.1 psi. Five computer runs were made for this problem using different time steps as seen in Fig. 9. In each case, the nonlinear

3.8

correction forces in the equilibrium equations were taken as the value computed during the previous time step. As can be noted, the smaller the time step, the better the approximation, as expected. As an alternate to this procedure, the nonlinear correction forces in a given time step can be recomputed by iteration (obtain a trial solution, computed correction force, obtain new solution, etc.). For this problem of proportional loading, this procedure is equivalent to using smaller time steps without iteration during each time step.

After the final equilibrium condition is reached under no drainage conditions, the drained situation can be achieved by letting the pore pressure decrease to zero by allowing drainage through the top and bottom surfaces of the soil sample. It can be shown that for this soil model, the decay of the pore pressure will occur elastically; that is, the intergranular stress state will move off the yield surface as the pore pressure decreases, so that the decay rate will be as described in the previous elastic triaxial solution.

The solutions for these cases are shown in Fig. 10 where the vertical intergranular stress is plotted as a function of the total vertical strain for various values of the cohesion and for a fixed value of the friction angle of 30°. If the cohesion is 24.0 psi or greater, the soil sample always remains elastic. The initial stress state when a vertical stress of 50 psi is applied and no drainage is allowed is $\bar{\sigma}_3 = 33.3$ psi and p = 16.7 psi. When drainage is then allowed, the pore pressure decreases to zero, and the vertical intergranular stress increases to the applied stress

of 50 psi. The final state is the same as would occur if the sample had been tested dry (no pore pressure). If, however, the cohesion is lower, the initial undrained state causes plastic flow to occur with the drained condition occurring elastically, as shown. For a value of cohesion equal to 14.4 psi, the initial undrained state occurs with no excess pore pressure, and the drained state is the same as the undrained state. For values of cohesion less than 14.4 psi, equilibrium under the applied loads cannot be maintained. It should be pointed out that for values of cohesion between 14.4 and 24.0 psi, the dry test will show no plastic flow, while the undrained-drained sequence will yield plastic strains.

It is clear then that even for this relatively simple soil model, the stress-strain behavior between saturated and unsaturated soil samples will be different and will be influenced by the rate of loading (as compared with the rate of pore pressure decay). To investigate this analytic solution further, the previous solution was nondimensionalized in the following fashion. Non dimensional parameters are defined as

$$\beta_1 = \frac{6}{\sqrt{3}} \left(\frac{\cos\phi}{3 - \sin\phi} \right)$$

$$\beta_2 = \left(\frac{1 + 2\sqrt{3}\alpha}{3\sqrt{3}\alpha} \right)$$

$$\beta_3 = \left(\frac{1 - \sqrt{3}\alpha}{3\sqrt{3}\alpha} \right)$$

(26)

The upper and lower limits of cohesion for which a nonlinear solution (stable plastic strains will occur) can be obtained for the undrained case are

3.10

$$\left(\frac{c}{\sigma_N}\right)_u = \frac{1}{\sqrt{3}\,\beta_1}$$

$$\left(\frac{c}{\sigma_N}\right)_L = \frac{1}{\beta_1}\left(\frac{1}{\sqrt{3}} - \alpha\right)$$

For any value of cohesion between these limits, the solution yields

$$\left(\frac{\bar{q}_r}{\sigma_N}\right) = -\left(\frac{P}{\sigma_N}\right) = \beta_3 - \frac{\beta_1}{3\alpha}\left(\frac{c}{\sigma_N}\right)$$

$$\left(\frac{\bar{q}_3}{\sigma_N}\right) = \beta_2 - \frac{\beta_1}{3\alpha}\left(\frac{c}{\sigma_N}\right)$$

$$\epsilon_3^e = \frac{\sigma_N}{E}\left\{\left(\frac{\bar{q}_3}{\sigma_N}\right) - 2\upsilon\left(\frac{\bar{q}_r}{\sigma_N}\right)\right\}$$

$$\epsilon_3^P = \frac{\sigma_N}{E}\left\{\beta_3(1-2\upsilon)\left(\frac{\bar{q}_3}{\sigma_n} + 2\frac{\bar{q}_r}{\sigma_N}\right)\right\}$$

$$\epsilon_3^T = \epsilon_3^e + \epsilon_3^P$$

After this initial solution occurs, the addition vertical strain that will develop as the excess pore pressure is allowed to decay to zero is

$$\epsilon_3 = \frac{\sigma_N}{E}\left\{(1-2\upsilon)\left(\frac{P}{\sigma_N}\right)\right\}$$

so that the final strain is the sum of the strains from equations

28 and 29. The solutions for several parameter variations are shown in Figs. 11 through 14. In Fig. 11, the nondimensional vertical intergranular stress is plotted as a function of the ratio $\epsilon_3 / \epsilon_{3_d}^D$, where $\epsilon_{3_d}^D$ is the vertical strain that would occur in the dry state and is simply

$$\epsilon_3^D = \frac{\sigma_N}{E} \qquad (30)$$

As may be noted, the difference in limiting values of cohesion for this problem is relatively small, but the influence on the final strain is large (ratio of 6.25). Curves are shown for four equally spaced values of cohesion between the limiting values.

The same solution is shown in Fig. 12, except that the friction angle was increased from 5° to 30°. As may be noted, the final strains are much lower than those of Fig. 11, and the associated plastic strains occurring during the initial undrained state are much smaller. This is due to the fact that for the higher friction angle the plastic volume expansion is larger than for the smaller friction angle causing the excess pore pressure to decay more rapidly as plastic strains develop. Fig. 13 shows the same results for a still larger friction angle of 45°, again showing a smaller difference in final strains.

The results for a different value of Poisson's ratio ($\nu = 0.25$) are shown in Fig. 14 for a friction angle of 30°. As can be noted, the behavior is essentially different than that of Fig. 12. This is due to the fact that the elastic volume change

3.12

during the initial loading decreases as Poisson's ratio increases.

3.4 McCormick Ranch Sand Model

It is, of course, well known that the relatively simpli-
fied constitutive models, such as the Coulomb-Mohr model, can only
crudely approximate the stress-strain behavior of real soils. In
order to properly take into account the influence of pore fluid on
soil response, more realistic models must be developed. An example
of such a model was presented in Ref. 4 wherein the parameters of
the model were chosen to match (as closely as possible) available
experimental data on a particular sand sample, known as McCormick
Ranch Sand. A rather extensive series of triaxial, uniaxial, and
hydrostatic compression tests were conducted and an attempt was
made to fit the analytic model so as to reproduce the available data.

It was found that for the particular parameters chosen
the stress-strain curve during the initial load-unload cycle could
be adequately reproduced for the triaxial compression test (over a
wide range of confining pressures) and for the uniaxial compression
test. The soil model, however, was significantly stiffer under
hydrostatic compression (although the shape of the load-unload curve
was the same) than the experimental data.

The model is based on the following analysis. The hydro-
static and deviatoric stress-strain components are related by

$$\dot{s}_{ij} = 2G\,\dot{e}_{ij}$$

$$\dot{p} = 3K\,\dot{e} \qquad\qquad (31)$$

3.13

where S_{ij} = deviatoric stress tensor

e_{ij} = deviatoric strain tensor

P = hydrostatic pressure

e = volumetric strain = $\frac{1}{3}(\dot{\epsilon}_1 + \dot{\epsilon}_2 + \dot{\epsilon}_3)$

and are related to the total stress-strain components by

$$\dot{e}_{ij} = \dot{\epsilon}_{ij} - \dot{e}\,\delta_{ij}$$

$$\dot{s}_{ij} = \dot{\sigma}_{ij} - \dot{p}\,\delta_{ij} \tag{32}$$

where $(\sigma_{ij}, \epsilon_{ij})$ are the total stress-strain tensors and δ_{ij} is the Kronecker delta. The dots in equations 31 and 32 indicate the corresponding rates. The parameters K and G represent the bulk and shear moduli, respectively, and are taken as functions of stress history.

The form used for the bulk modulus is:

loading: $K_L = K_0 + K_1 e + K_2 e^2$, for $\dot{e} > 0$ $\tag{33}$

unloading: $K_u = K_{0u} + K_{1u} P$

where the parameters K_0, K_1, K_2, K_{0u}, K_{1u} are parameters found by fitting the experimental data. In equation 33, volume compression is assumed to be positive. The corresponding form used for the shear modulus is

loading:

$$G_L = G_0 + \bar{\gamma}_1 \sqrt{J_2'} + \gamma_1 \, p + \gamma_2 \, p^2 \qquad \text{for} \quad p \le p_c$$

$$= G_1 + \bar{\gamma}_1 \sqrt{J_2'} \qquad\qquad \text{for} \quad p > p_c \tag{34}$$

unloading:

$$G_u = G_{0u} + \bar{\gamma}_{1u} \sqrt{J_2'} + \gamma_{1u} \, p + \gamma_{2u} \, p^2 \qquad \text{for} \quad p \le p_c$$

$$= G_{1u} + \bar{\gamma}_{1u} \sqrt{J_2'} \qquad\qquad \text{for} \quad p > p_c$$

and

$$G_1 = G_0 - \frac{1}{4} \frac{\gamma_1^2}{\gamma_2}$$

$$G_{1u} = G_{0u} - \frac{1}{4} \frac{\gamma_u^2}{\gamma_2} \tag{35}$$

where p_c is a critical hydrostatic pressure (positive in compression and J_2' is the second invariant of the deviatoric stresses (equation 19).

To match the specific test results for the sand sample, the following parameters were found to best reproduce all the data:

$G_0 = 8.0 \text{ ksi}$ $G_{0u} = 8.0 \text{ ksi}$

$K_0 = 5.83 \text{ ksi}$ $K_{0u} = 32.0 \text{ ksi}$

$K_1 = 80 \text{ ksi}$ $K_{1u} = 143$

$\gamma_1 = 32.4$ $\bar{\gamma}_1 = -110$

$\gamma_2 = -15.0 \text{ }1/\text{ksi}$ $K_L = 30,000 \text{ ksi}$

$\gamma_{1u} = 40.0$ $\gamma_{2u} = -18.5 \text{ }1/\text{ksi}$

$\bar{\gamma}_{1u} = 500.0$

The stress-strain behavior under uniaxial compression is

shown in Fig. 15 under both initial loading conditions as well as strain load/unload cycling. As may be noted, the stress-strain response exhibits the characteristic stiffening effect as well as the nonrecoverable behavior under load cycling. The pressure ranges shown are higher than normally used but suitable modification of the data input would convert this typical response to lower stress ranges of interest.

The behavior under triaxial compression is presented in Figs. 16 to 19 and again exhibits much of the characteristics anticipated for a sand sample. During the load/unload cycling, the model can be further improved to reproduce test data by modifying the shear modulus formulation under reload conditions to better match strain behavior with constant load cycling.

The previous data were obtained for the Ranch Sand model in the dry condition. To determine the behavior with pore fluid, similar problems were investigated including load cycling effects. In Fig. 20, the triaxial response is presented for a consolidated/ undrained experiment with load cycling in the vertical direction corresponding to the load cycles shown in Fig. 18 for the dry sample. In both cases, lateral or confining stresses were maintained constant. As can be seen in Fig. 20, the effect of pore pressure is to decrease the axial strain increment between load cycles. That is, in the undrained state, the soil model "shakes down" to effectively a linear model, although strong nonlinear behavior again takes effect as the applied load is finally increased beyond the load cycling regime.

Similar behavior is shown in Fig. 21 where the applied vertical load is cycled through the complete load range from 0 to 300 psi. This test corresponds to the dry triaxial test shown in Fig. 19. Again, it may be noted that within a load cycle, pore pressure effects cause the stress-strain behavior to "shake down" to an effective elastic state. Of course this type of response can be modified by changing the definition of the reload shear modulus as defined by equation 34. A plot of the invariants of effective stresses during the loading cycle for the triaxial tests is shown in Fig. 22, for both the consolidated undrained and drained tests. As may be noted, J_1 is constant during the undrained test indicating that the bulk modulus (equation 33) is constant with this model. Therefore the cycling response will be completely dependent upon the variation in the deviatoric response, or the shear modulus behavior. The cycling response will be essentially elastic as long as the shear modulus is maintained as the unloading modulus within the cycling load range.

Two other triaxial experiments were conducted where the samples were consolidated under a confining stress of 400 psi, loaded vertically in the drained state to 630 psi and then further loaded cycled between 575 psi and 690 psi in both the drained and undrained states. A comparison of the results is shown in Fig. 23, in which anticipated responses were determined.

(a) Configuration Analyzed

Applied Pressure = 10 psi

Clay Layer   7'

$E = 1000$ psi
$\nu = 0.25$
$K/\gamma_w = 0.048 \ in^4/lb \cdot sec.$
$C_v = 57.6 \ in^2/sec.$

Impervious Boundary

p = 10 psi

Free Draining

Roller Supports

No Drainage

Fixed Supports
No Drainage

(b) Finite Element Configuration
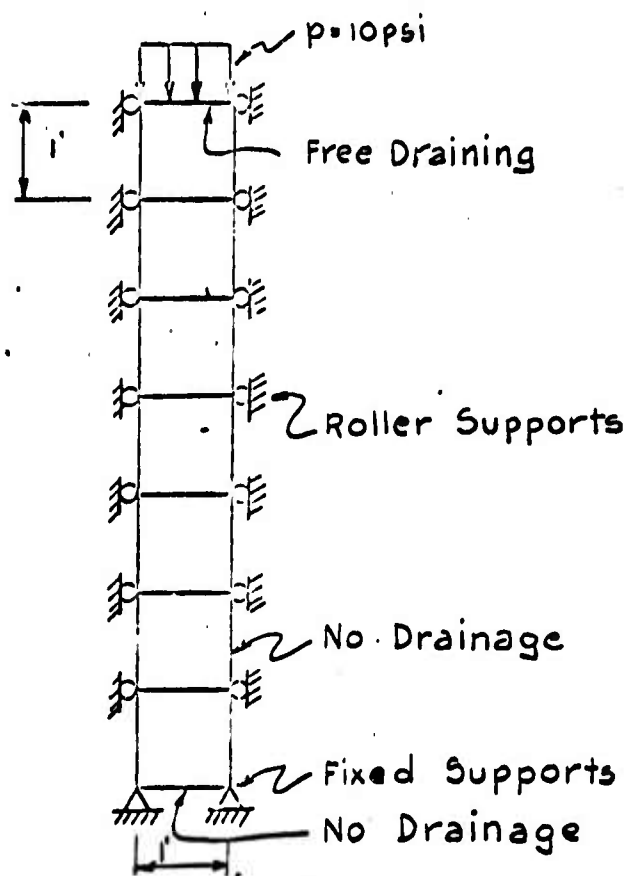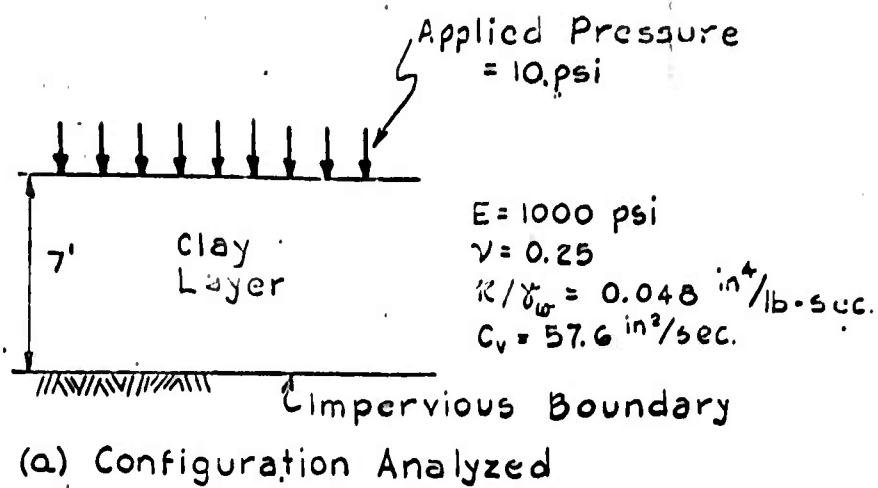
Fig. 1   One-Dimensional Elastic Consolidation Problem

3.18
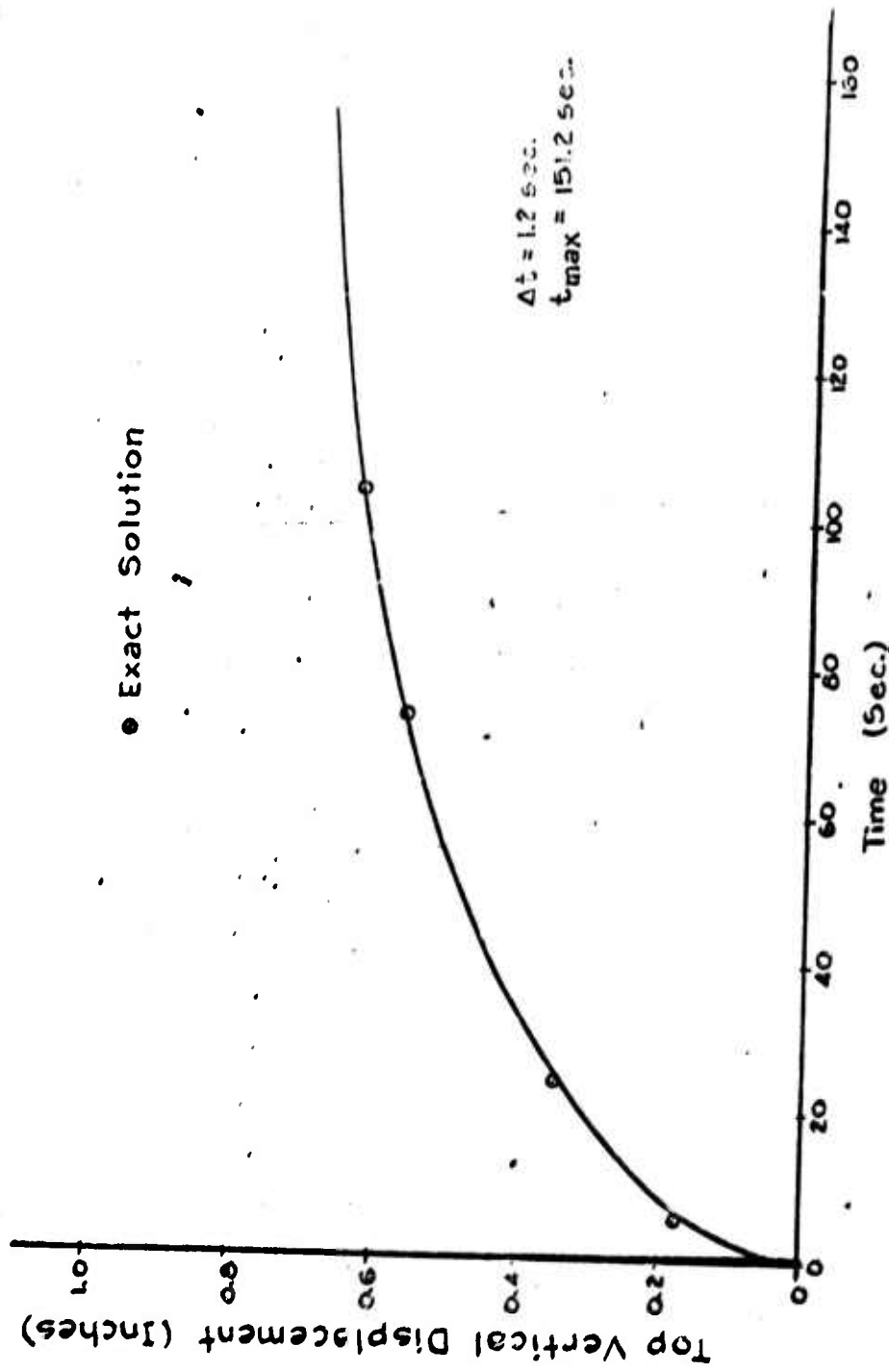
Fig. 2 One Dimensional Elastic Consolidation,
Settlement of Top of Layer

3.19
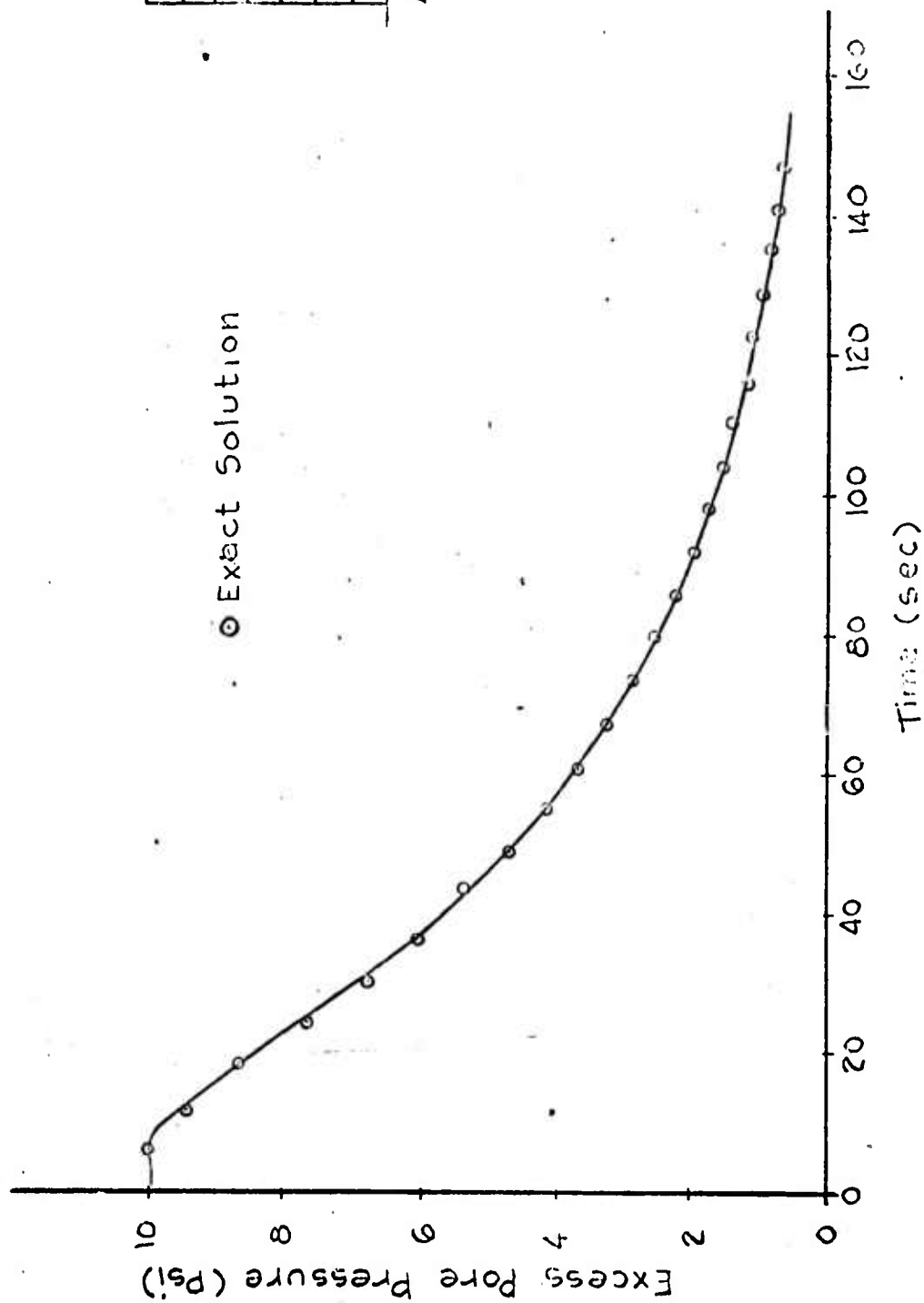
Fig. 3 One Dimensional Elastic Consolidation, Excess Pore Pressure at Bottom Element

3.20
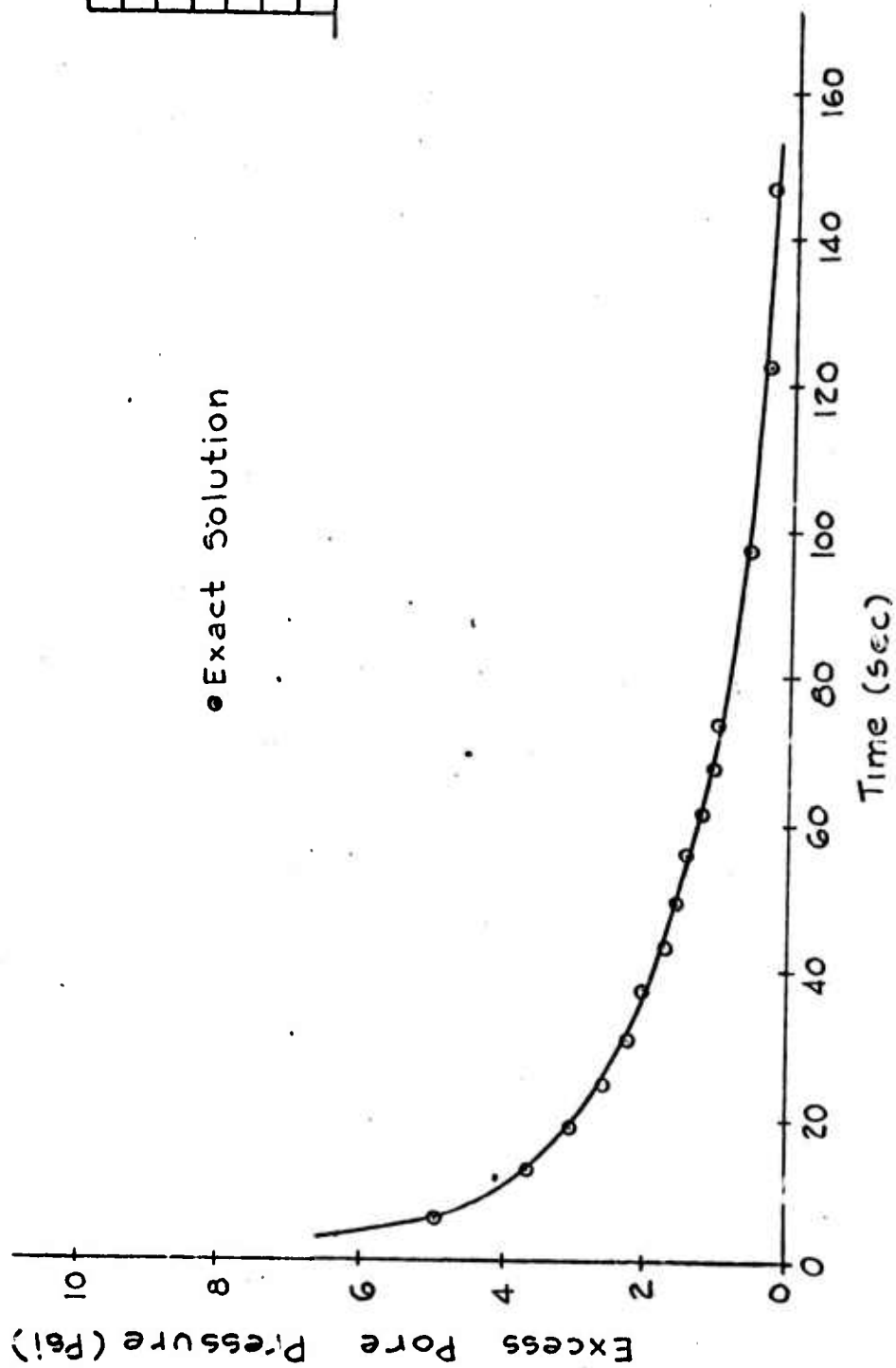
Fig. 4 One Dimensional Elastic Consolidation,

Excess Pore Pressure at 2nd Element
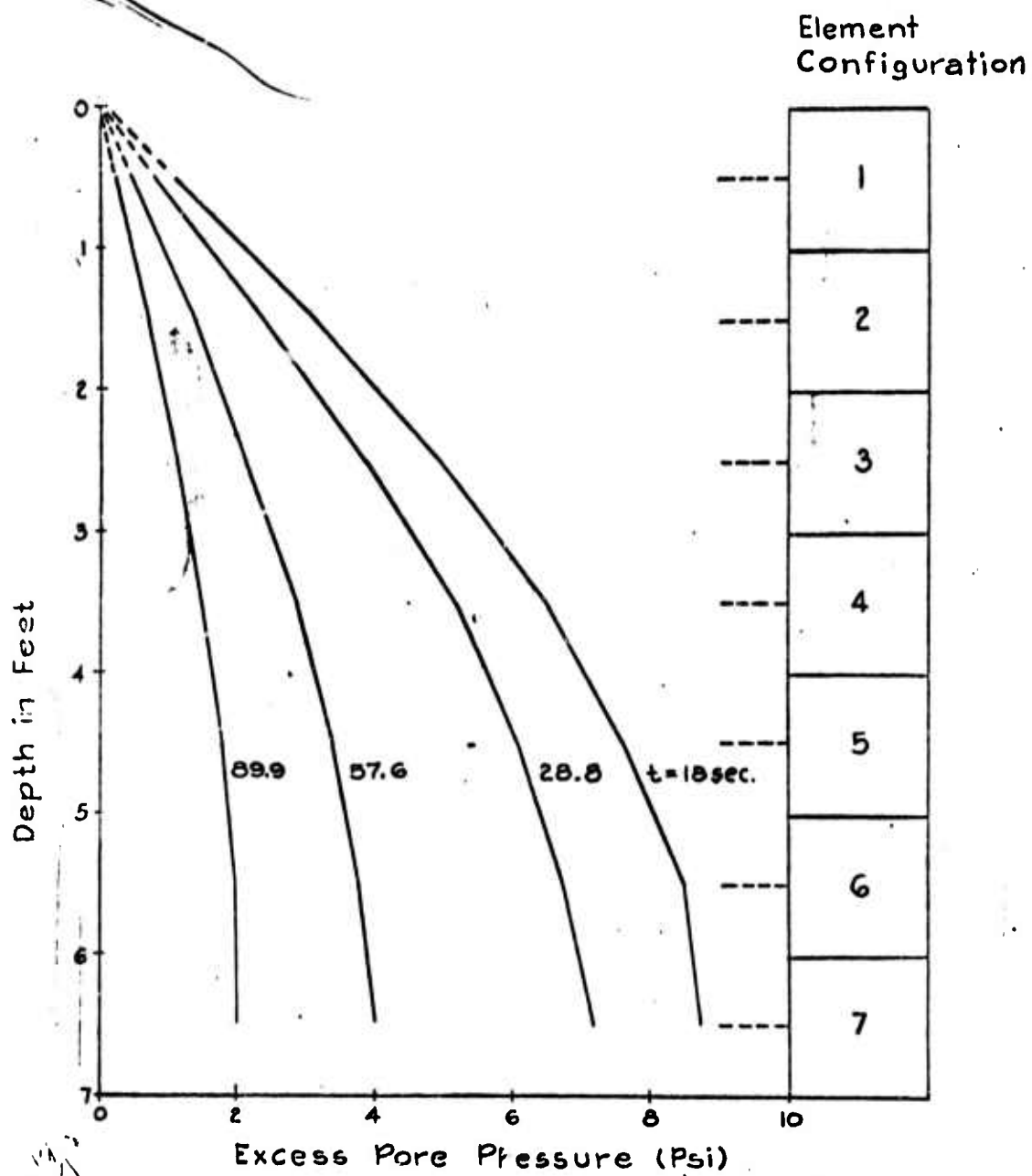
Fig. 5 One-Dimensional Elastic Consolidation,
Excess Pore Pressure Distribution
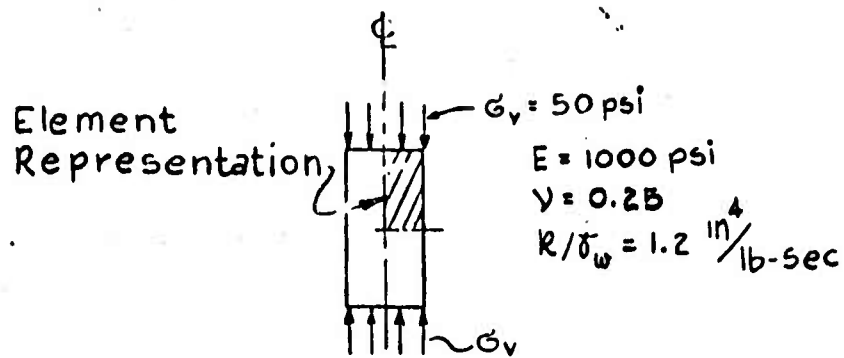
(a) Configuration of Triaxial Model
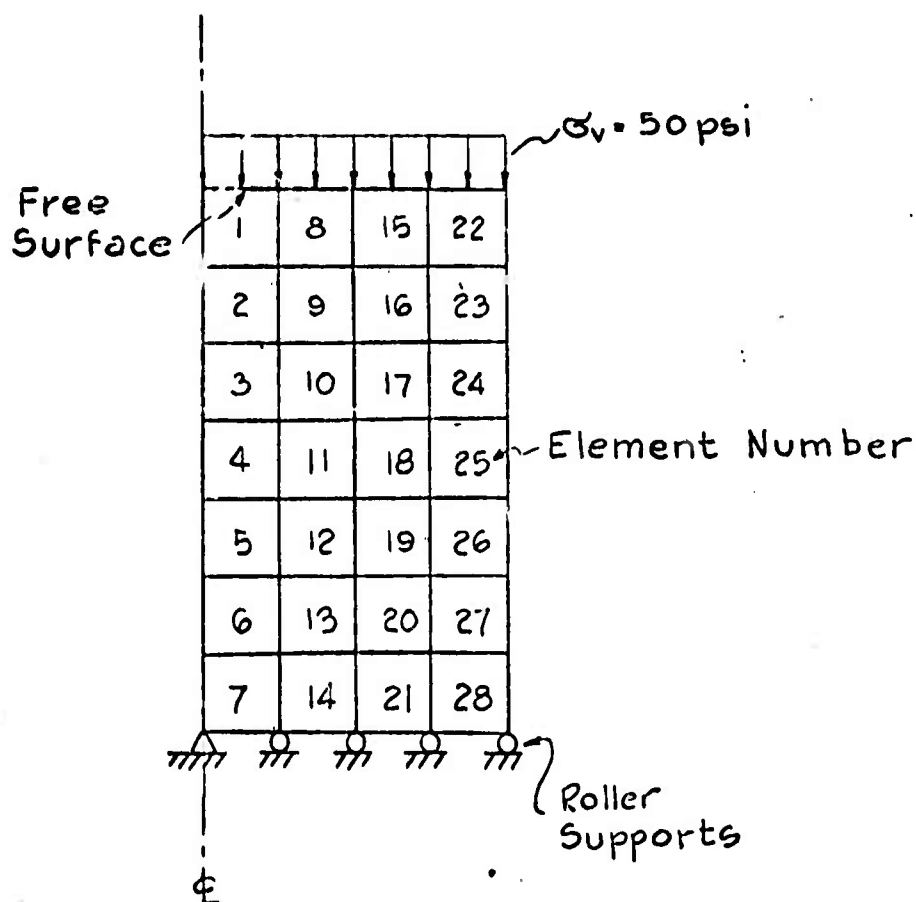
(b) Axisymmetric Finite Element Model

Fig. 6   Elastic Triaxial Test Configuration
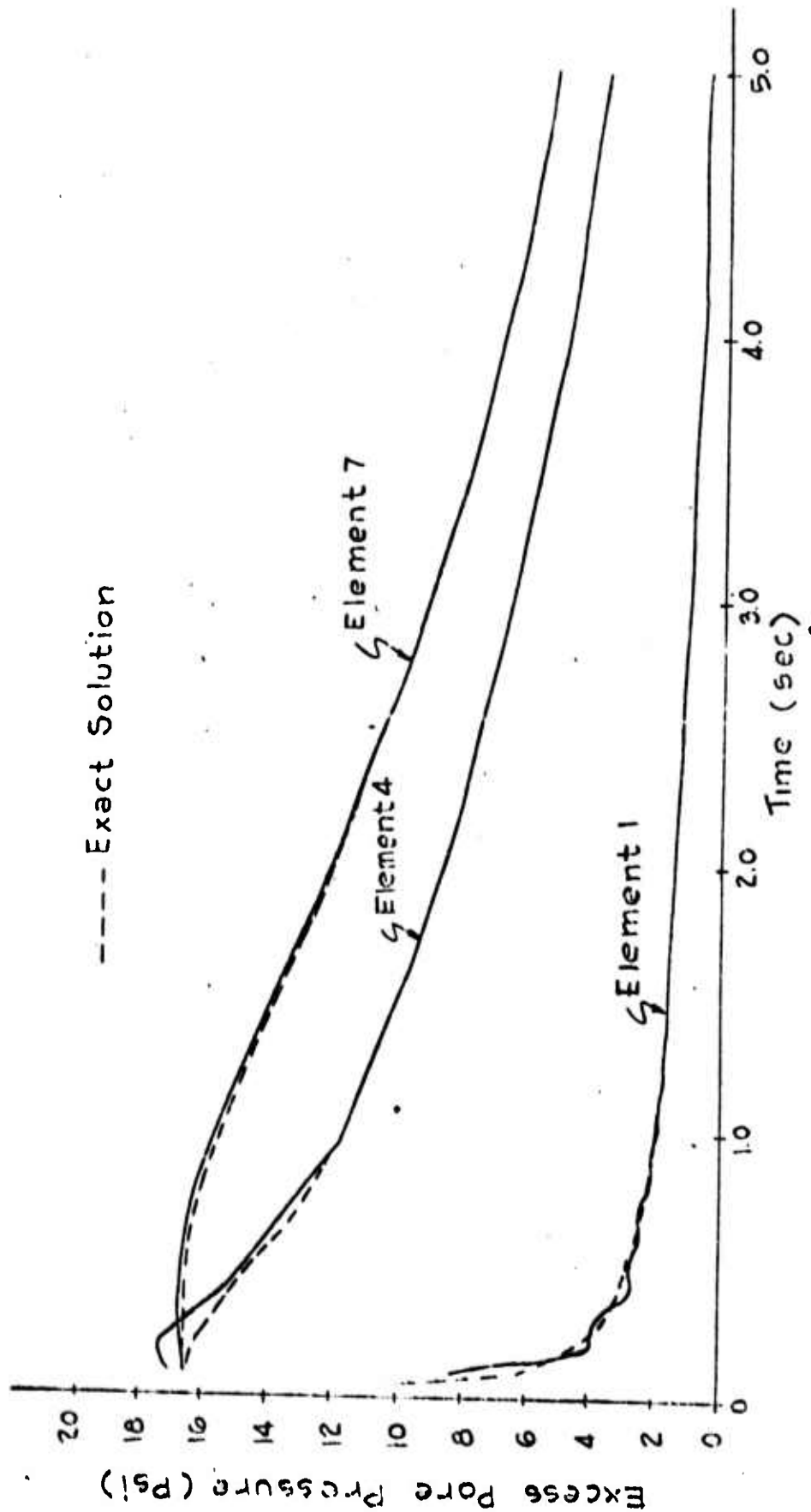
Fig. 7 Elastic Triaxial Test, Excess Pore Pressure Near Centerline

3.24
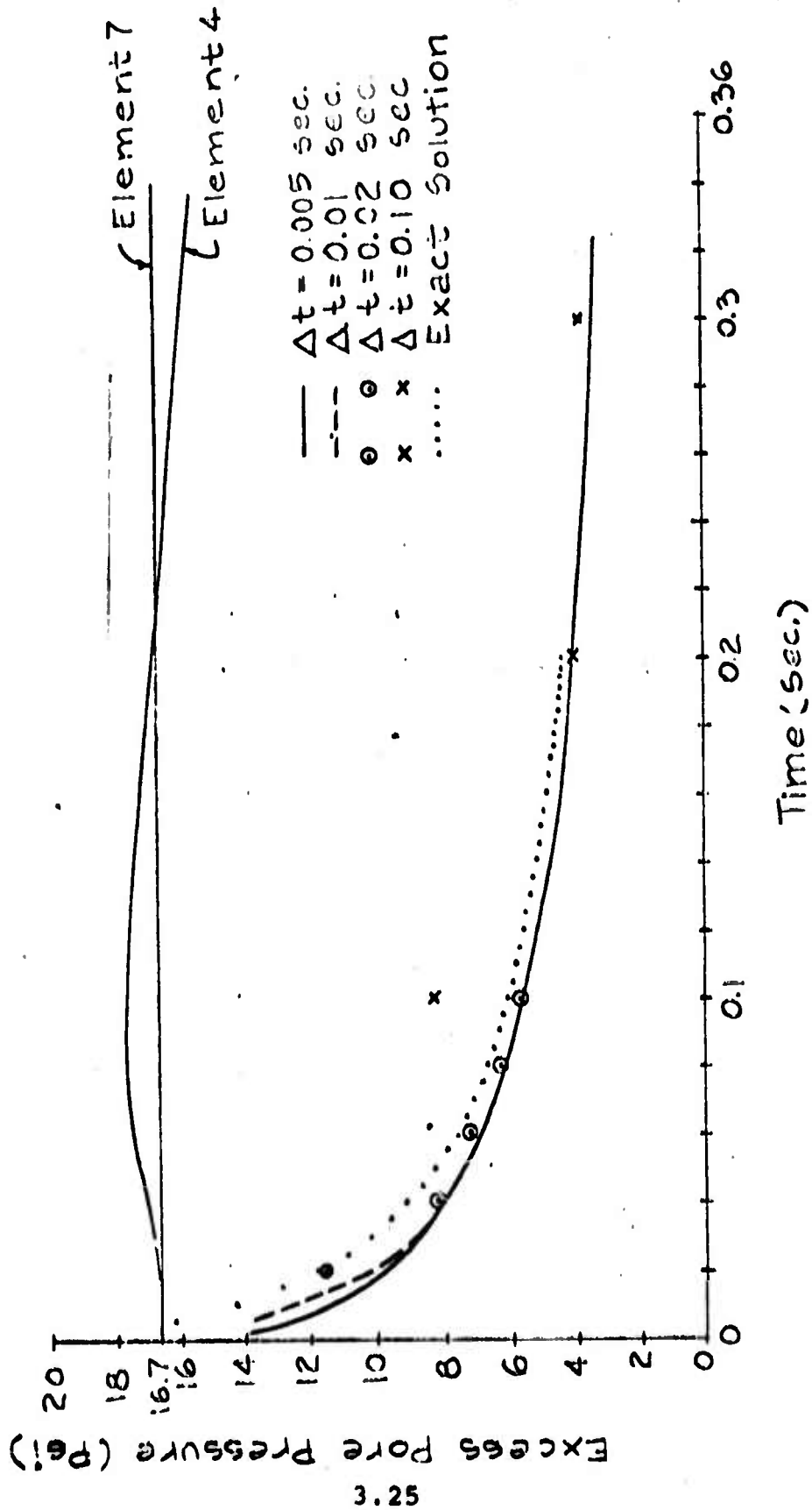
Fig. 8 Elastic Triaxial Solution, Excess Pore Pressure Near Centerline,

Influence of Time Increment on Solution

3.25

KOUNT = 1
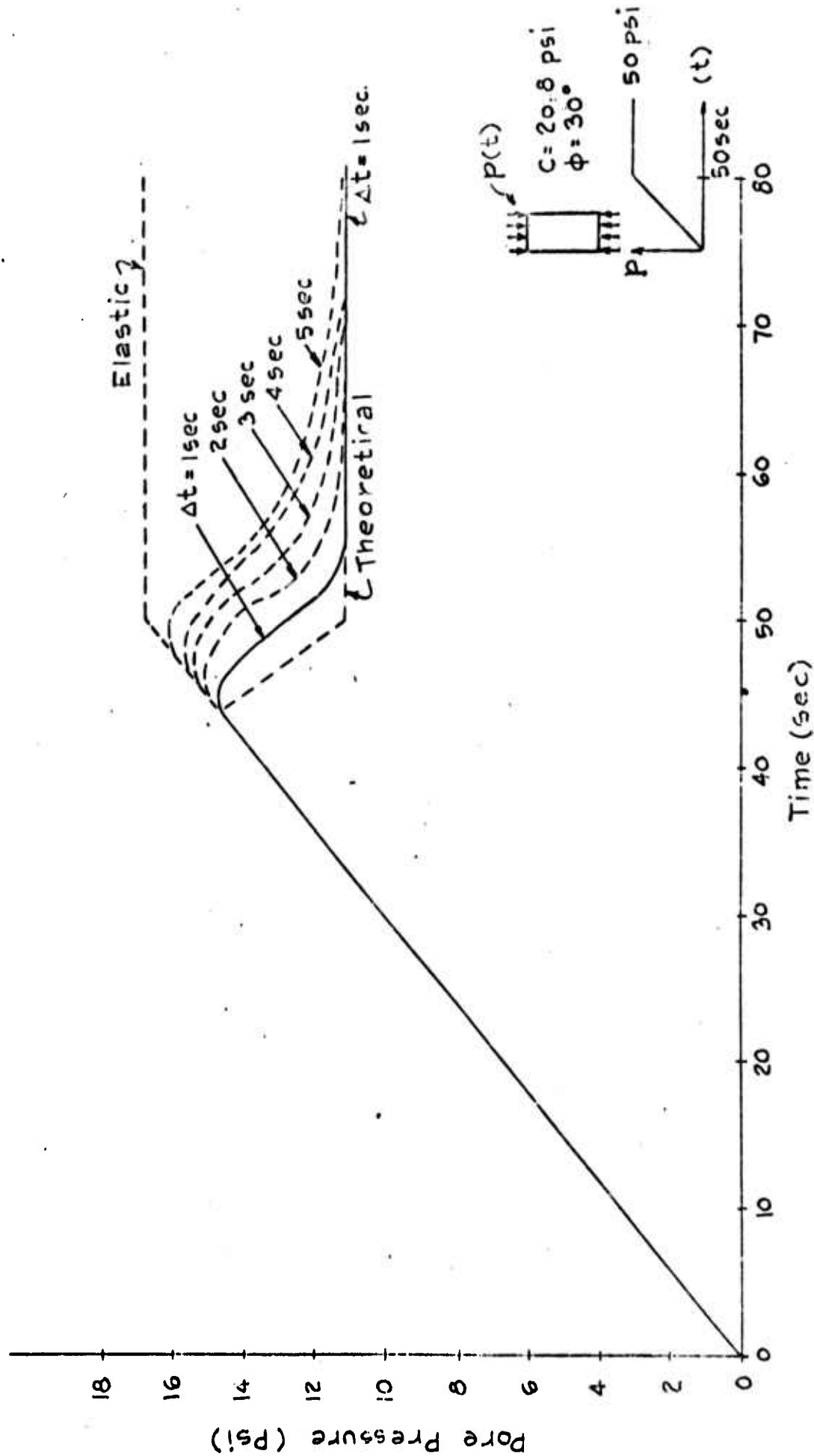
Fig. 9 Triaxial Compression, Cculomb-Mohr Material, Undrained Test

3.26
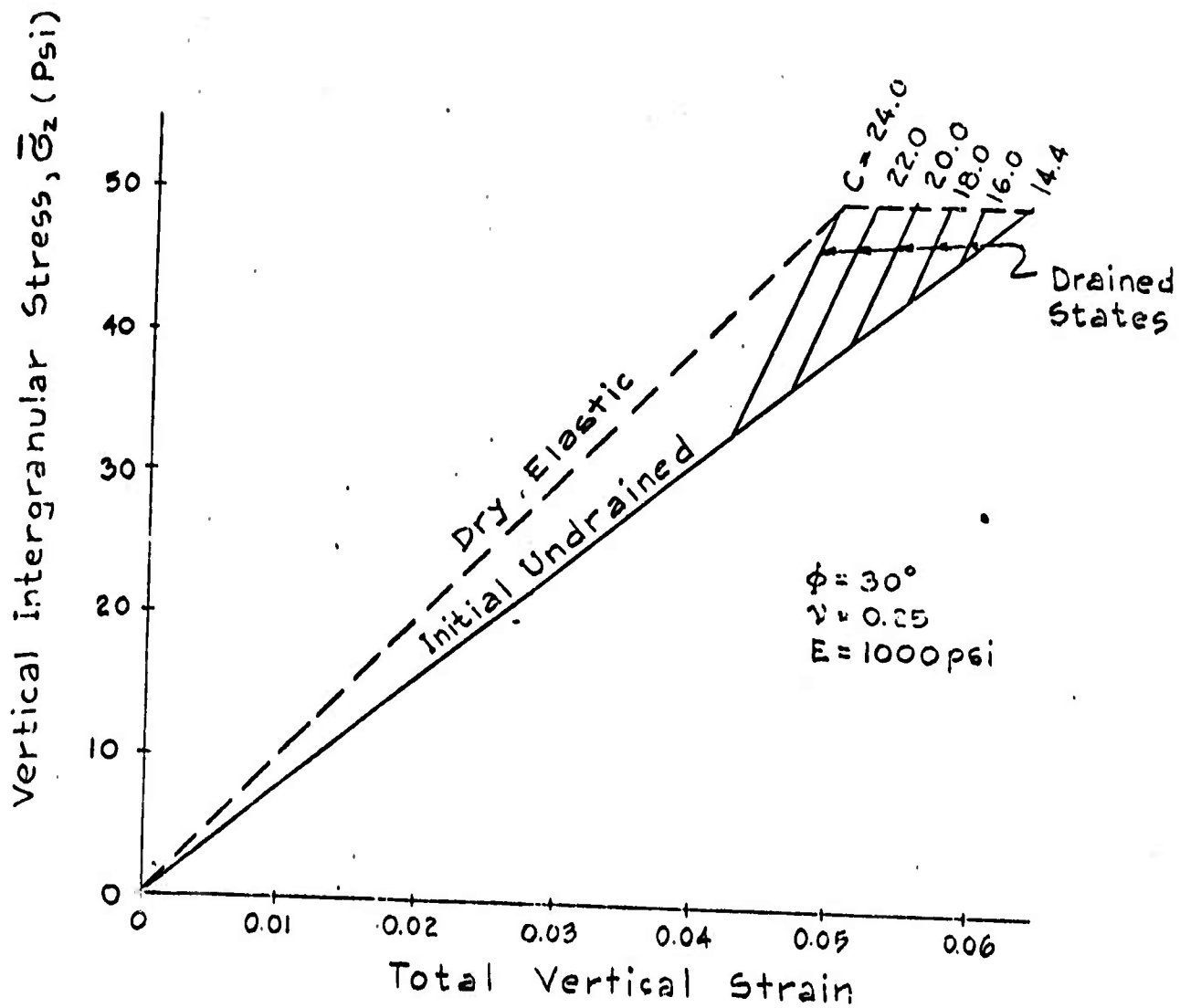
Fig. 10   Triaxial Compression Test, Coulomb-Mohr Material
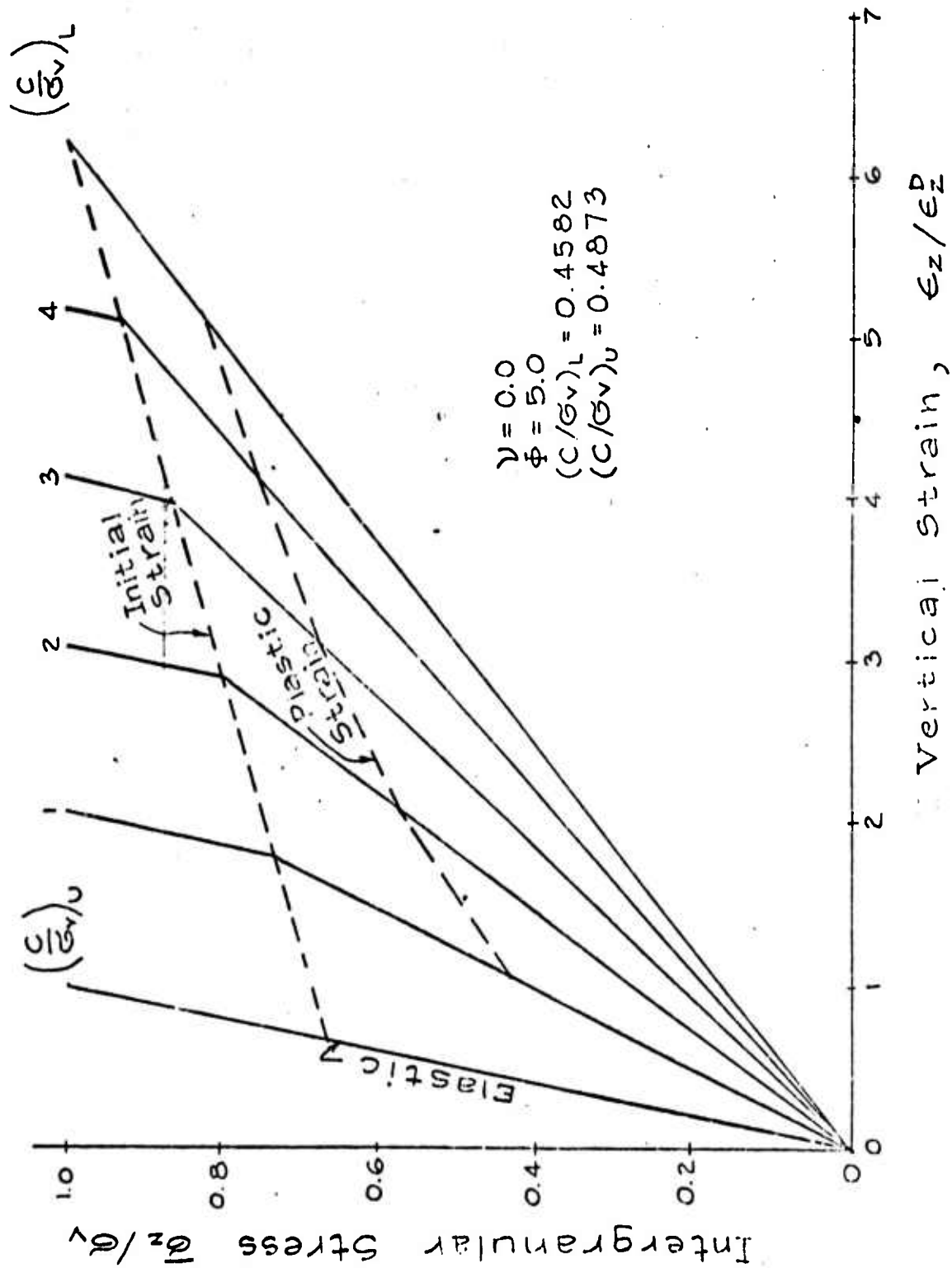
Fig. 11 Triaxial Compression Test, Coulomb-Mohr Material, Nondimensional Solution
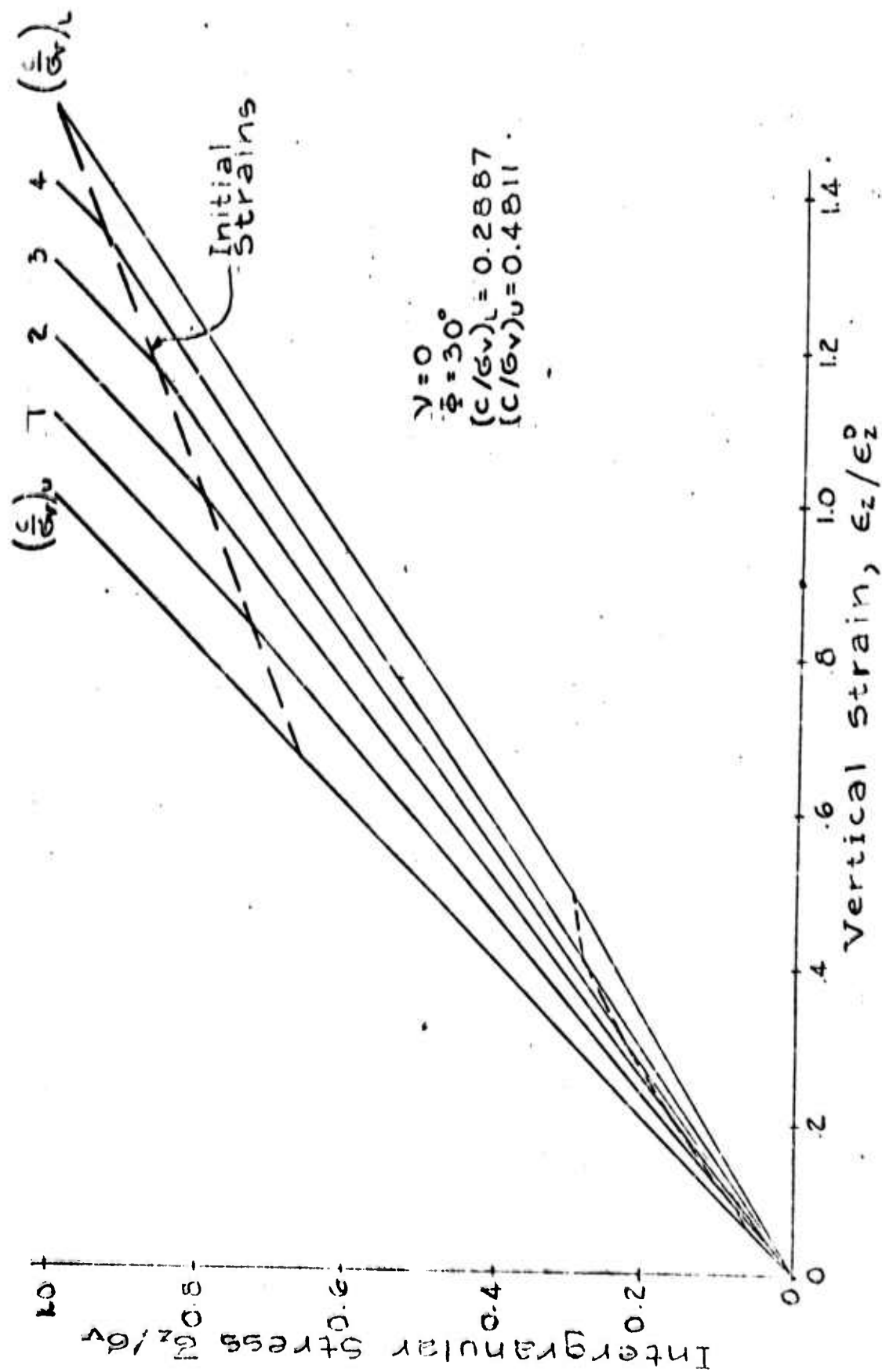
3.28

Fig. 17 Triaxial Compression Test, Coulomb-Mohr Material, Non-Dimensional Solution

$\gamma = 0$

$\bar{\phi} = 30°$

$(c/\sigma_v)_L = 0.2887$

$[c/\sigma_v]_u = 0.4811$

Initial Strains

$\left(\frac{c}{\sigma_v}\right)_L$

$\left(\frac{c}{\sigma_v}\right)_u$

1 2 3 4

Vertical Strain, ϵ_z/ϵ_z^p

Intergranular Stress $\bar{\sigma}_z/\sigma_v$

3.29
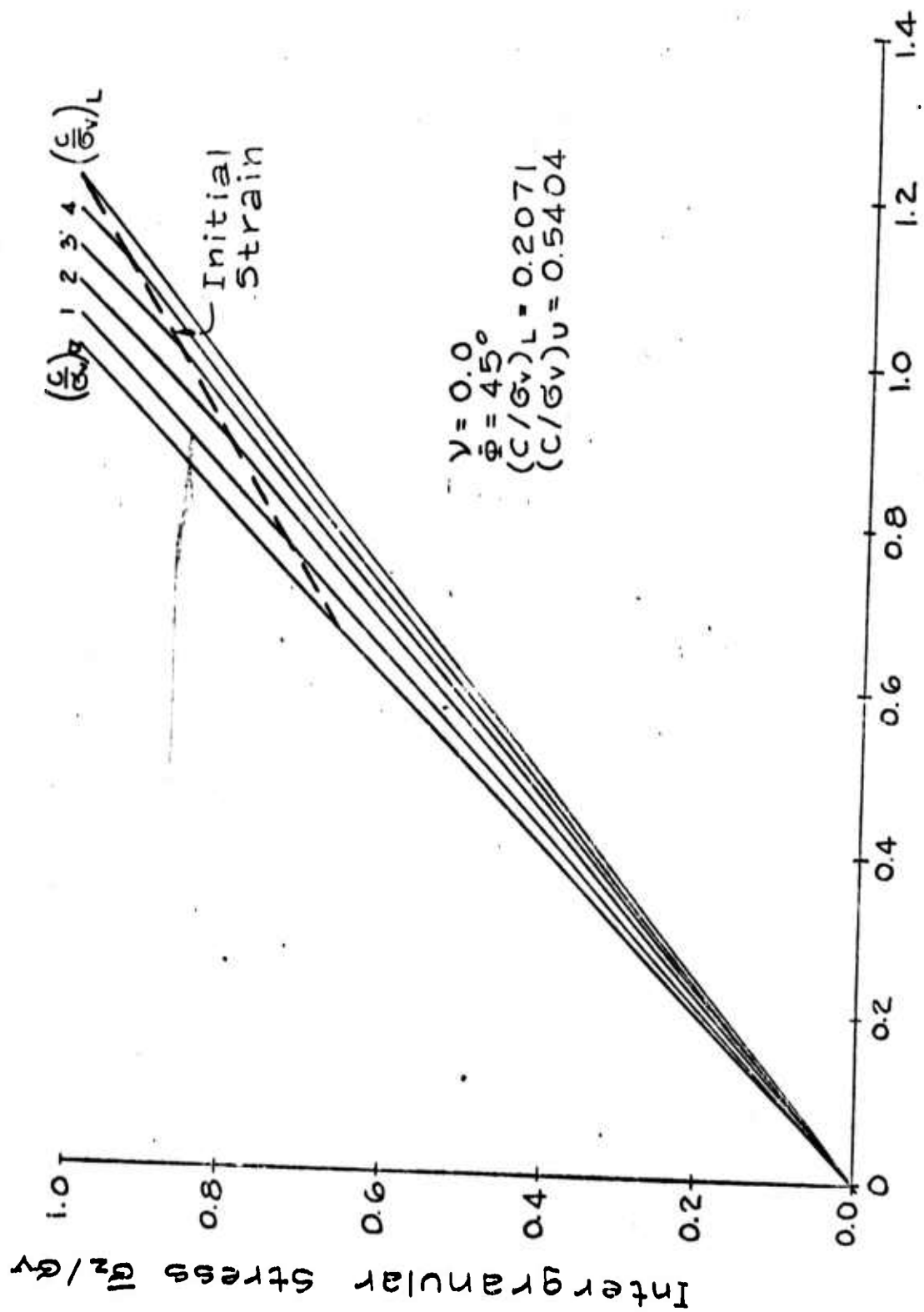
Fig. 13 Triaxial Compression Test, Coulomb-Mohr Material, Nondimensional Solution
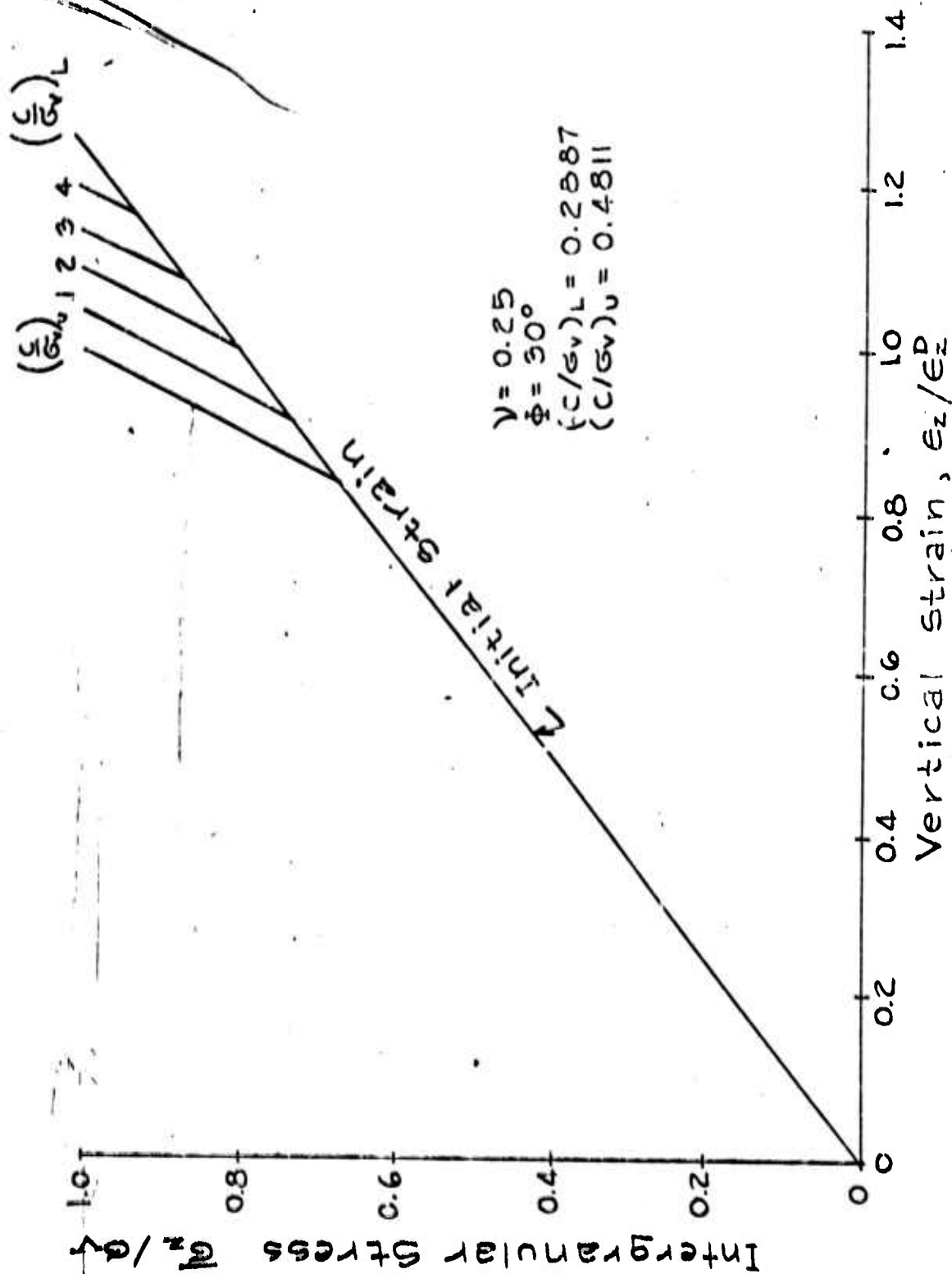
Fig. 14 Triaxial Compression Test, Coulomb-Mohr Material, Non-Dimensional Solution
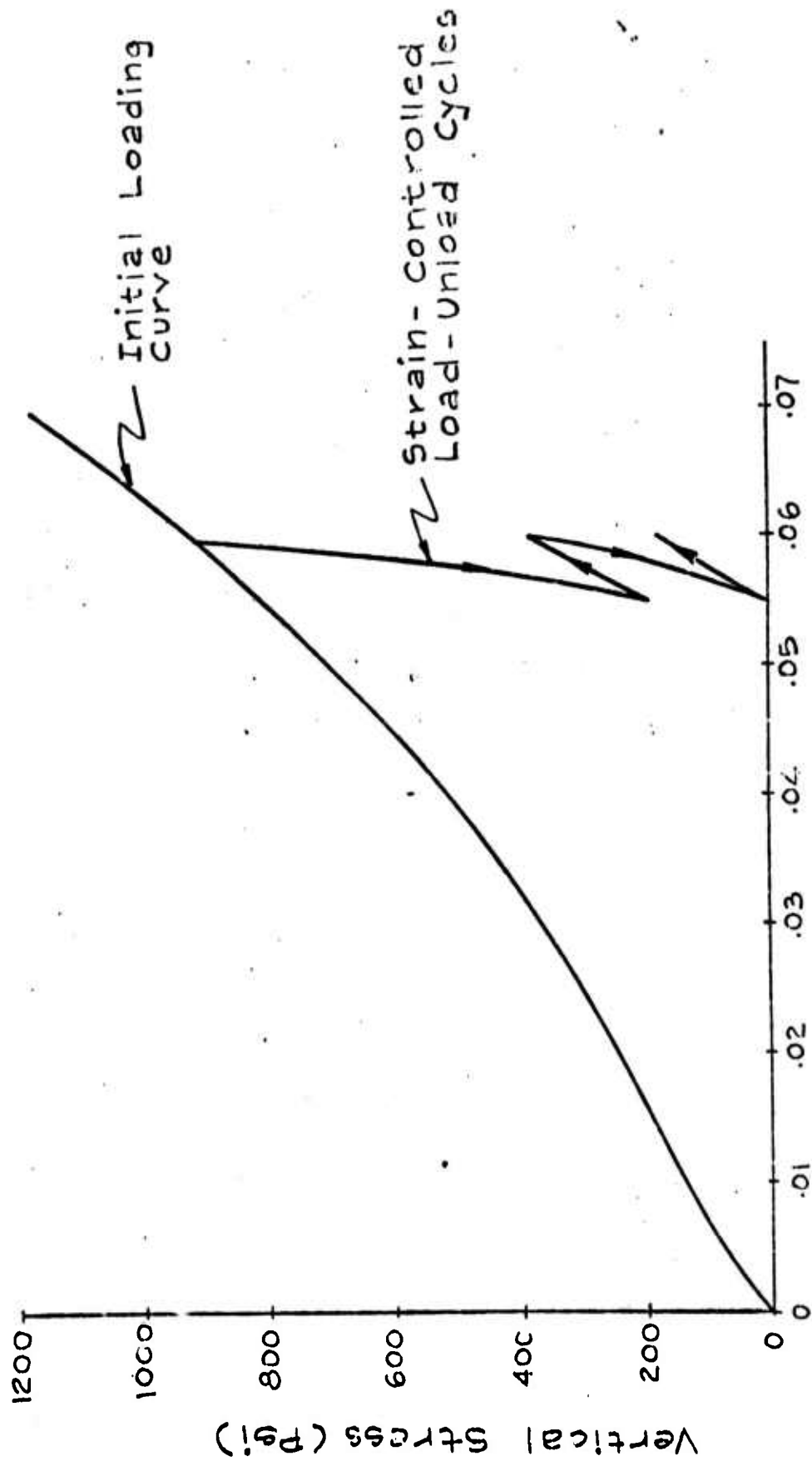
Fig. 15 Uniaxial Compression Test, Ranch Sand Model,

No Pore Fluid

3.32
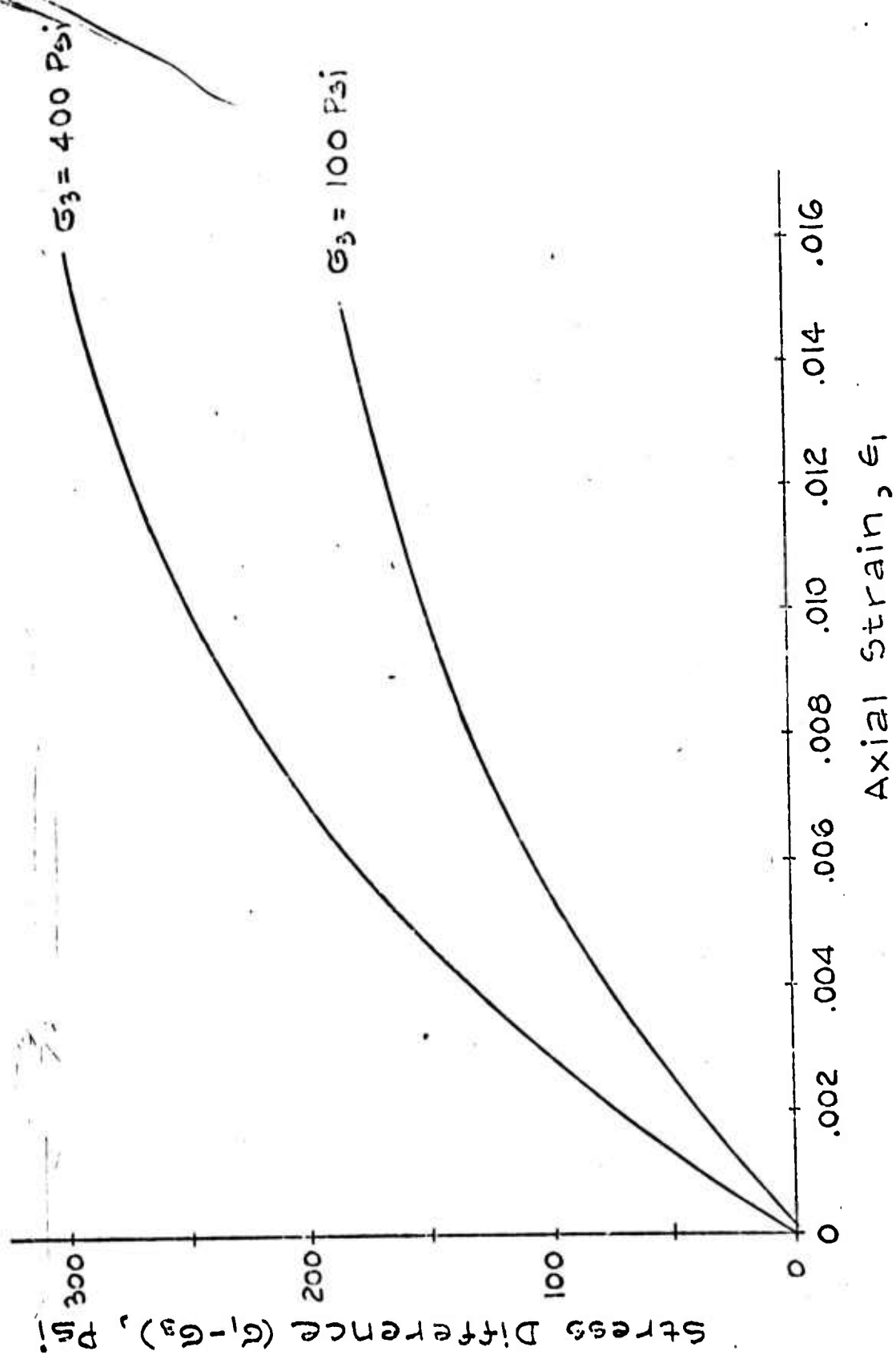
Fig. 16 Triaxial Response, Ranch Sand Model, No Pore Fluid

3.33
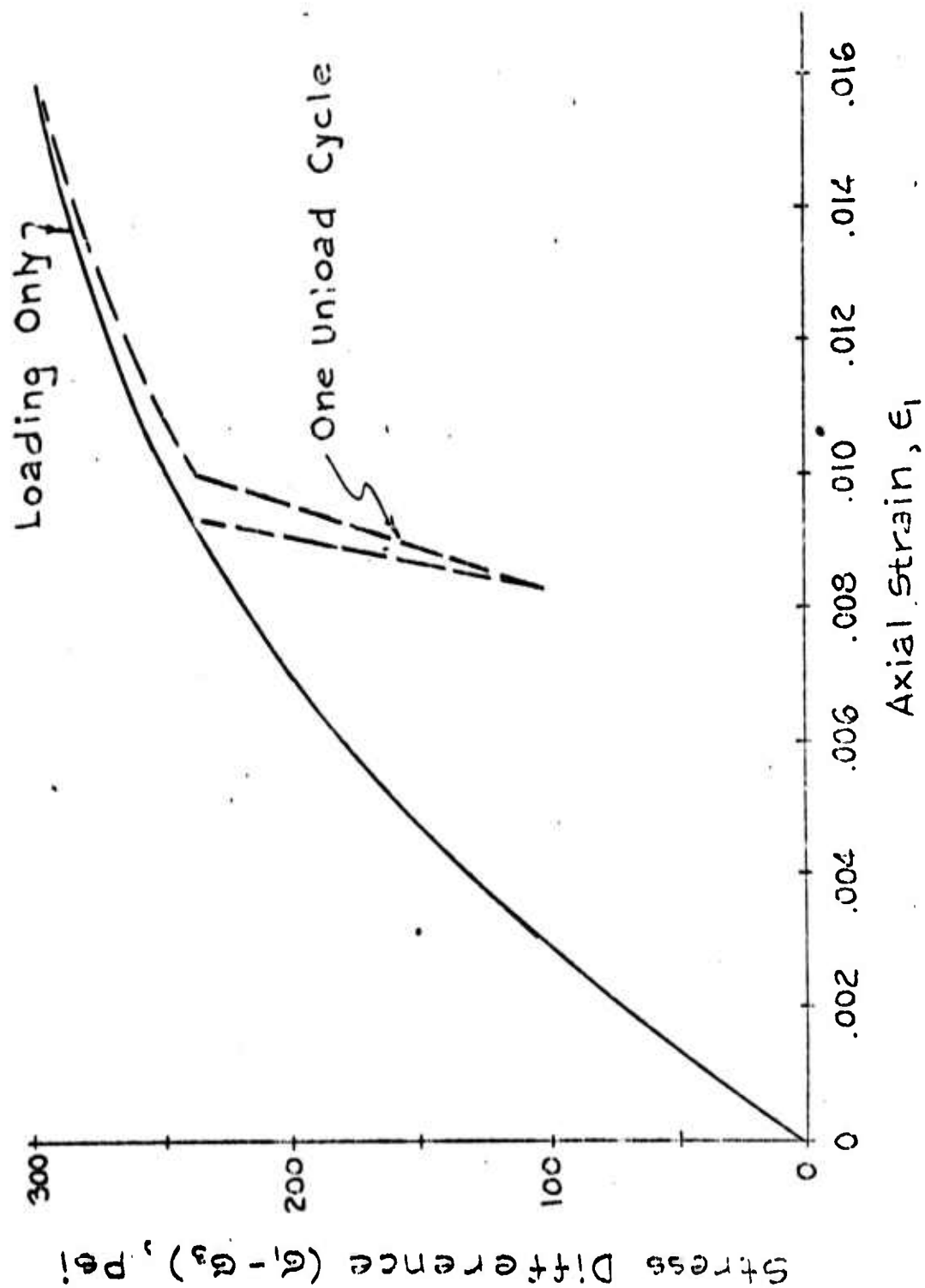
Fig. 17 Triaxial Response, Ranch Sand Model, No Pore Fluid

3.34
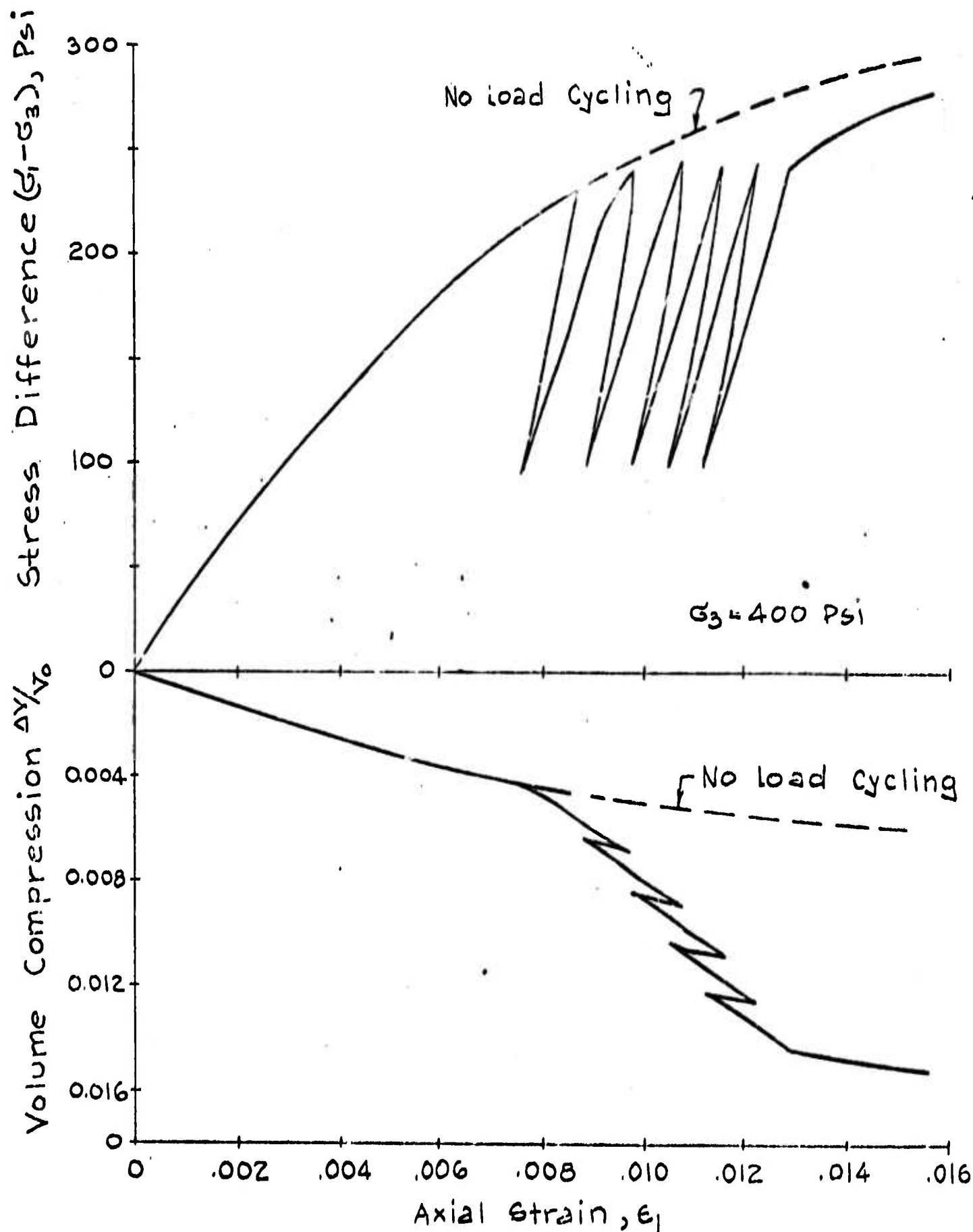
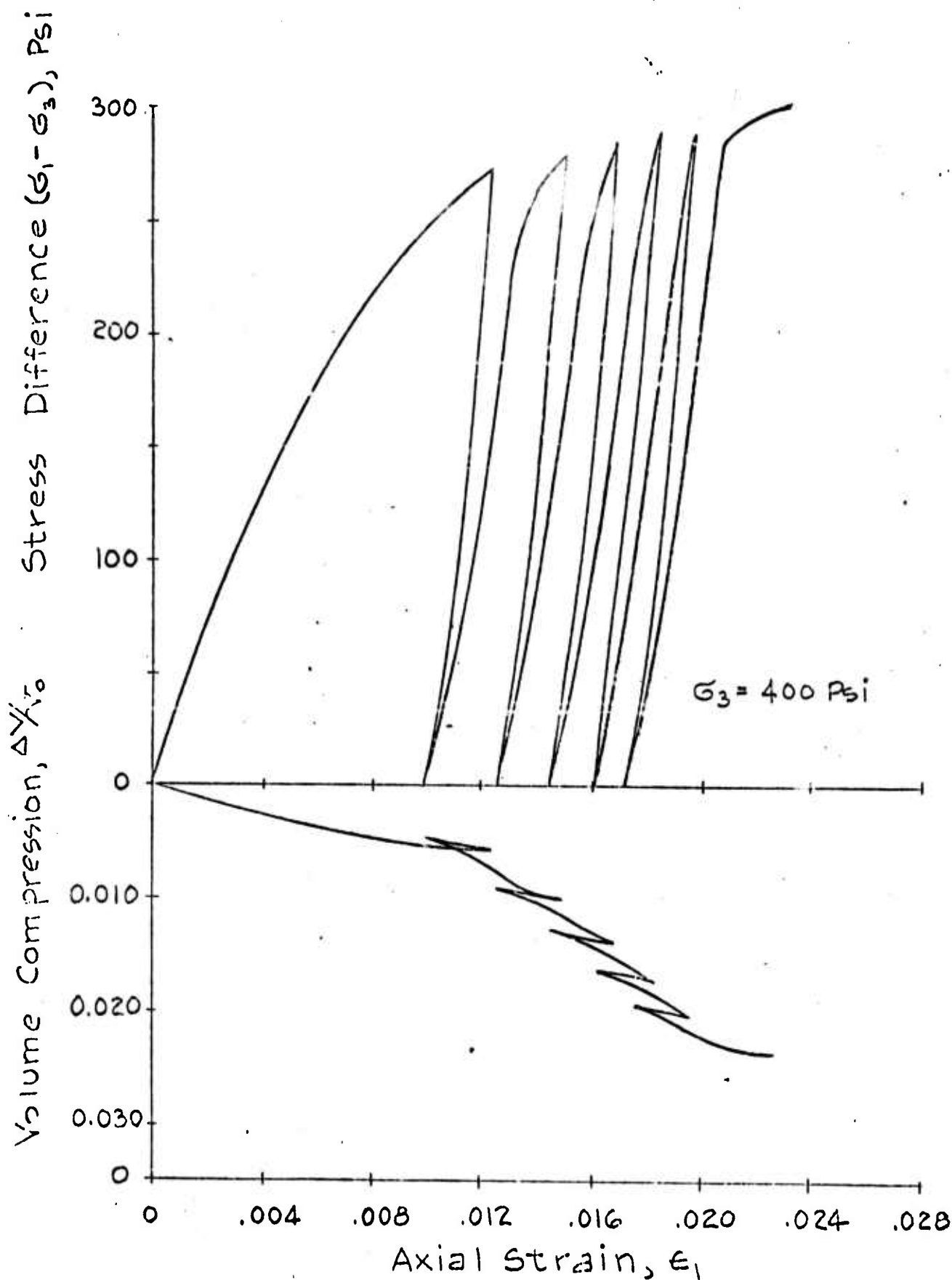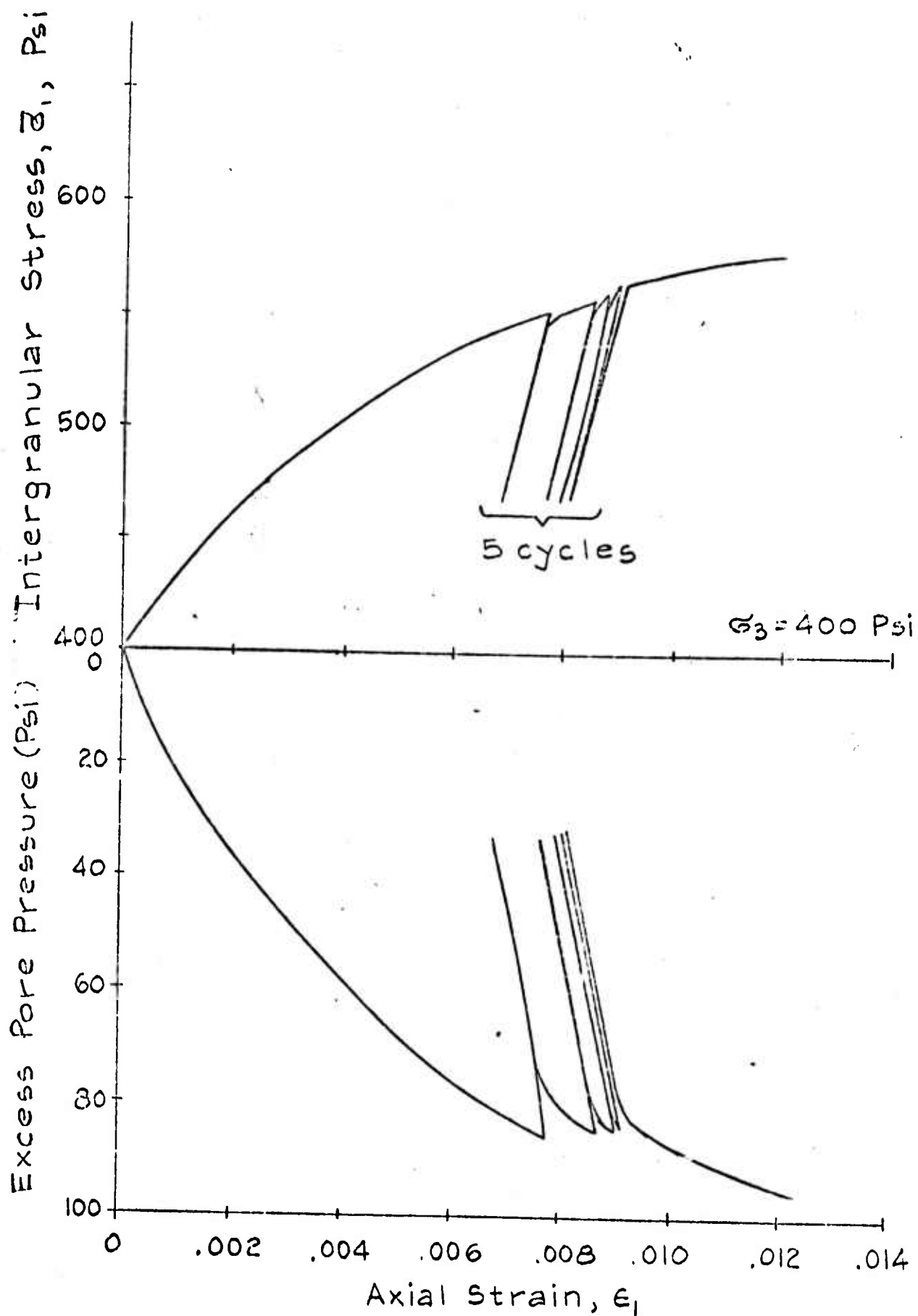Fig. 18   Triaxial Response, Ranch Sand Model,

No Pore Fluid

3.35

Fig. 19   Triaxial Response, Ranch Sand Model,
No Pore Fluid

3.36

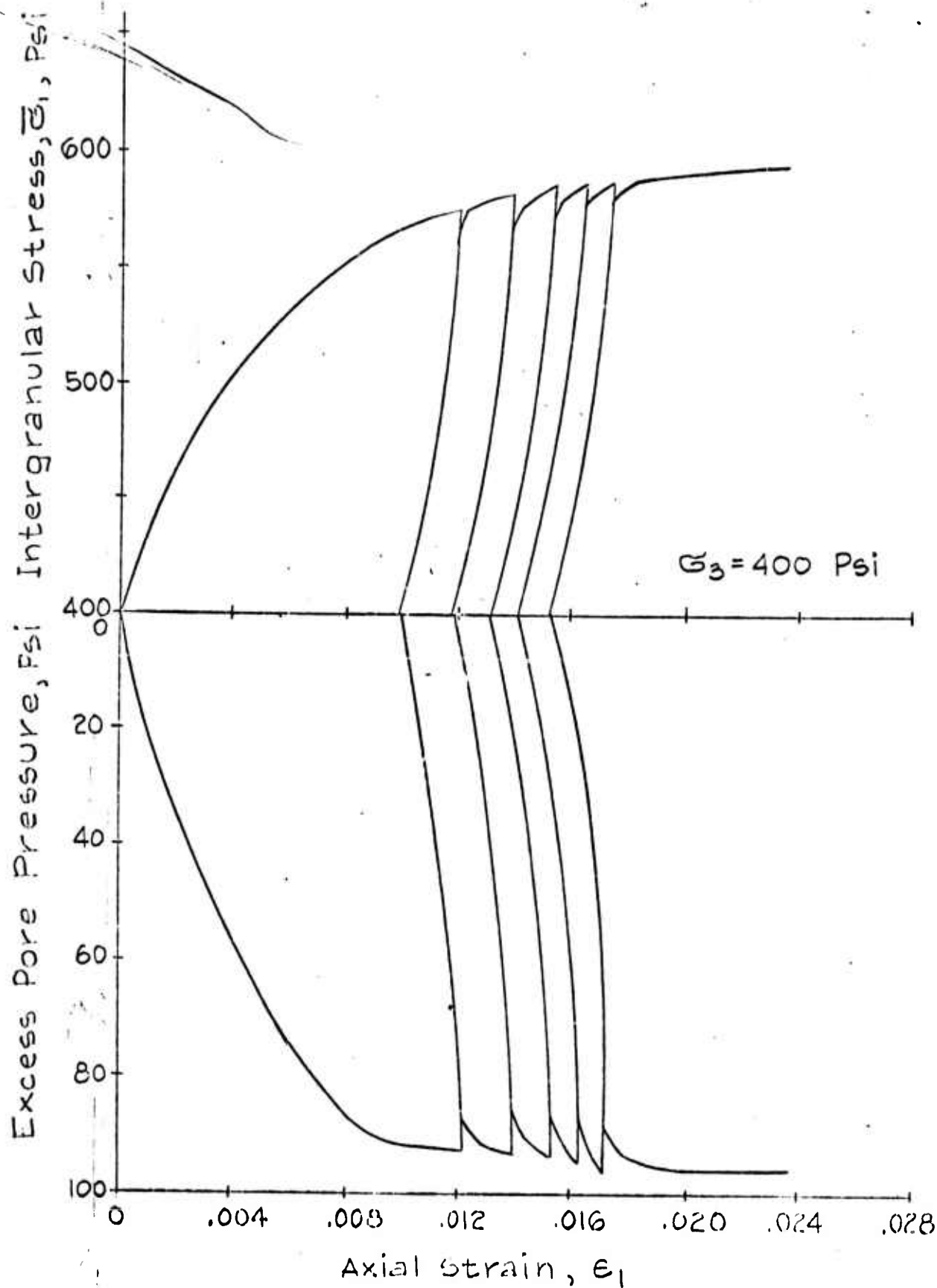Fig. 20   Triaxial Response, Ranch Sand Model,

Consolidated, Undrained Test

3.37

Fig. 21 Triaxial Response, Ranch Sand Model,
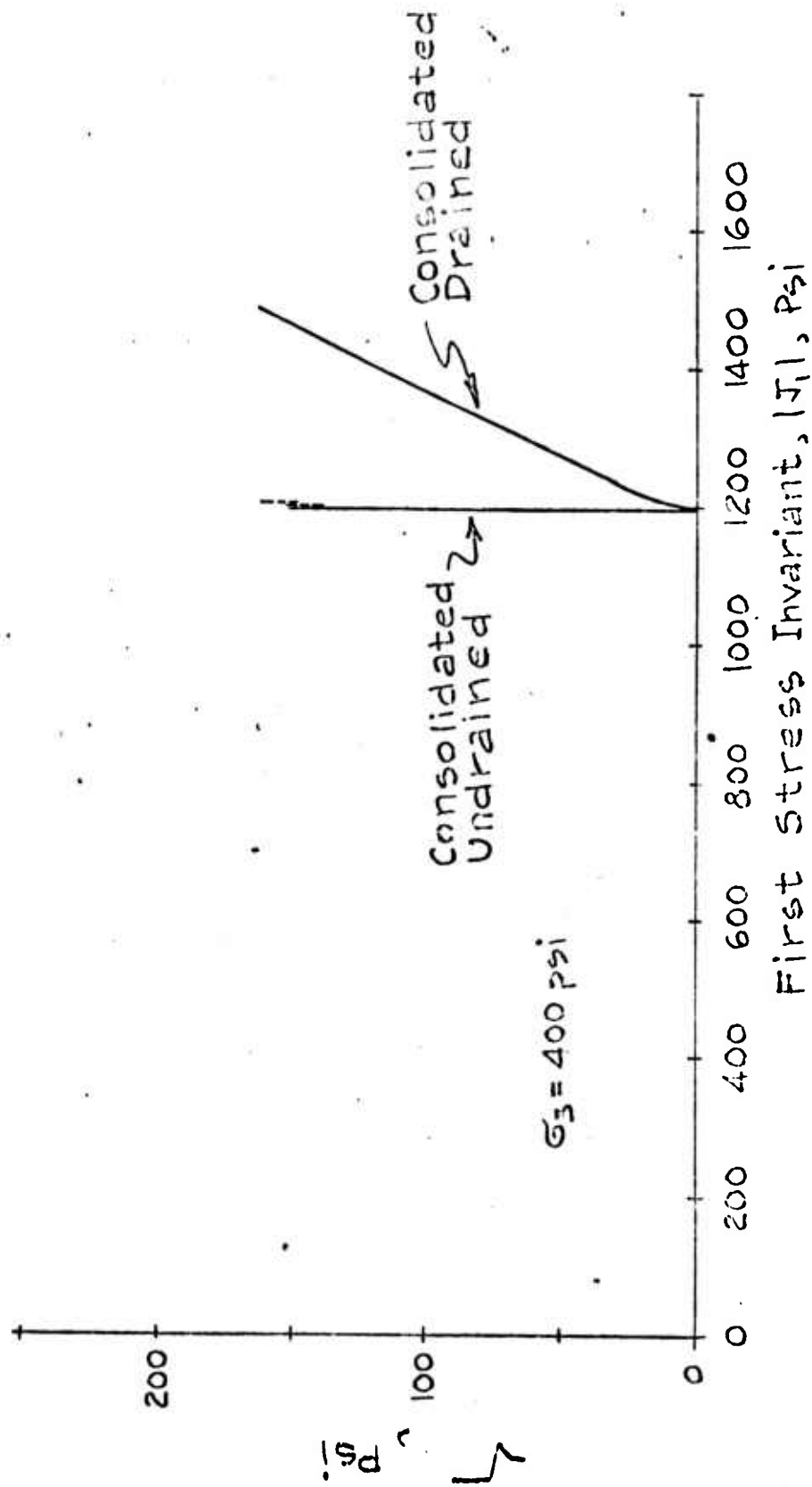
Consolidated Undrained Test

3.38

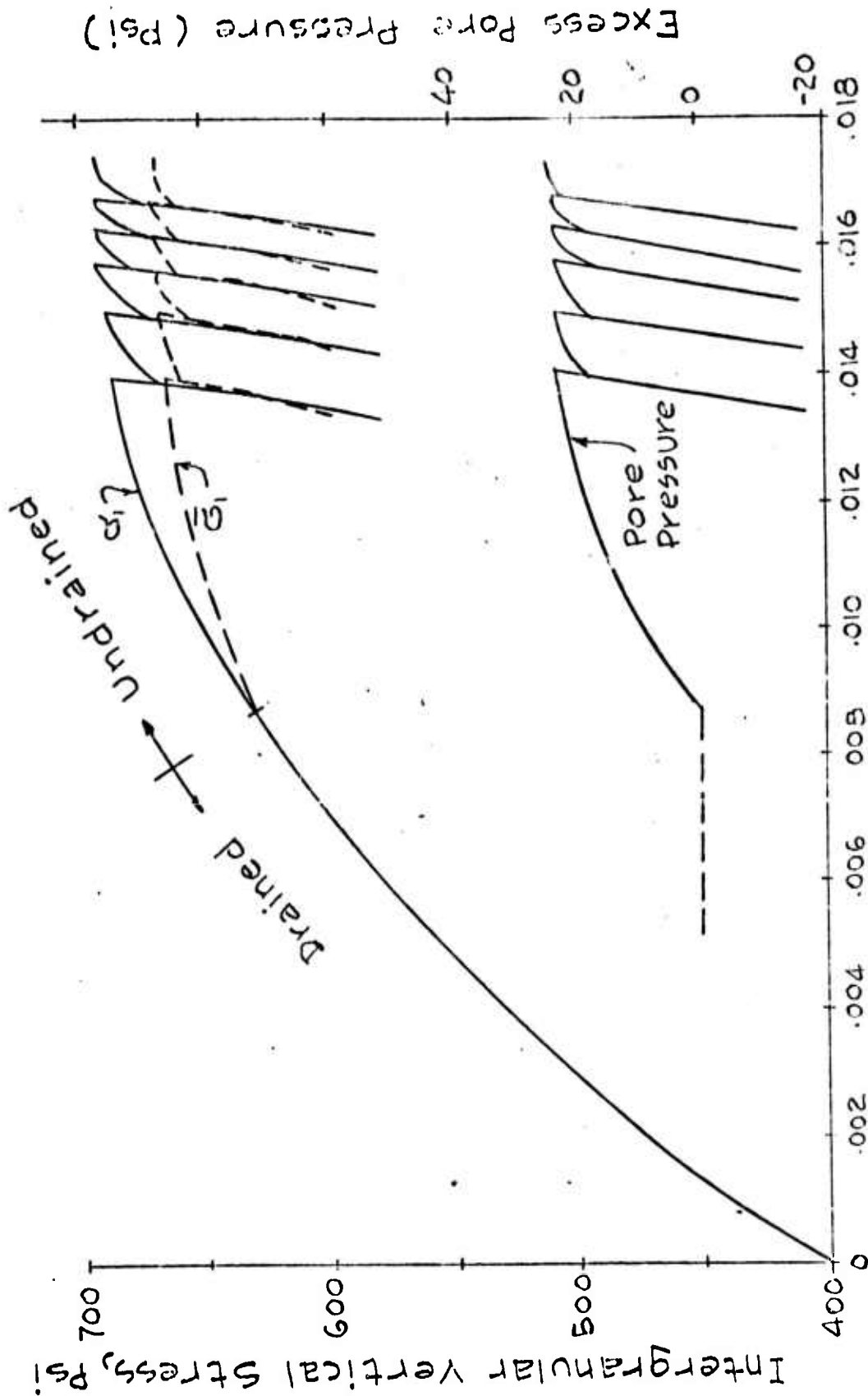Fig. 22 Triaxial Response, Ranch Sand Model, Effective Stress Invariants

Fig. 23 Triaxial Response, Ranch Sand Model, Consolidated Drained/Undrained Test

4.0 Stress Wave Propagation in Uniaxial Compression

The first dynamic problem considered was the one-dimensional soil column subjected to a step pulse pressure at its end, a configuration often used in determining wave propagation properties through actual soil columns. The configuration studied assumed the soil column to be contained within an imprevious membrane so that no pore fluid (for the case of saturated soils) could escape. However, it was assumed that the membrane provided no lateral restraint to the soil column, so that even for an incompressible fluid, a finite compressed wave speed exists. If lateral inertia effects are neglected, the effective modulus of the soil (plane strain/stress condition) is

$$E^* \cdot E / (1 - \nu^2)$$

(36)

and the effective dry wave speed is

$$c^* \cdot \left[E^* / \rho \right]^{1/2}$$

(37)

The finite element configuration used for this problem is shown in Fig. 24, and consisted of a set of square

plane strain elements with no lateral restraint provided to
the nodes. In the numerical calculation, lateral inertia
effects are in fact included since each node is considered
to have two degrees of freedom. The first problem run con-
tained no pore fluid, and the computed stress profile along
the rod is shown in Figure 25. As can be noted, the computed
stresses show the usual oscillations about the true solution
caused by the sharp stress front applied to the rod. The
propagation of the pulse through the soil is shown in Fig. 26
and the computed wave speed is seen to compare favorably with
the actual effective wave speed. A similar result is shown in
Fig. 27 for the case of a different Poisson's ratio.

For the case of saturated soils, the stress profile
along the rod at a late time in the pulse is shown in Fig. 28.
As may be noted, the wave speed is higher than the dry wave
speed, since the pulse is already reflecting off the bottom
boundary. At the loaded end of the soil column, the solution
approaches the static solution, which for an incompressible
pore fluid, indicates that the pore pressure is

$$u = \sigma_0 / 2 \qquad\qquad (38)$$

where σ_o is the applied static loading. Figure 29 shows similar results for undrained soil with a different Poisson's ratio. As may be noted by comparing Figs. 28 and 29, the effective wave speed decreases as Poisson's ratio increases, which is opposite to the results computed for dry soils. Obviously the reason for this discrepancy lies in the amount of lateral inertia effects that are allowed to occur for the different Poisson's ratios.

A plot of peak stress traverse through the soil rod is shown in Figure 30, for cases of both dry and saturated soils. As may be seen, the effective dry wave velocity increases as Poisson's ratio increases (as predicted by equation 37). However, the opposite effect occurs for saturated soils since the partition of energy into the lateral direction essentially lowers the effective wave speed.

A series of problems were investigated for different coefficients of permeability. Stress profiles along the rod are shown in Fig. 31 for various values of $\bar{k}$ where

$$\bar{k} = k/\gamma_w$$

(39)

and $\bar{k}$ is the coefficient of permeability. From these results, it may be determined that the effective wave speed (as determined by peak stress traverse through the rod) is unaffected by the coefficient of permeability. However, the stress profile, both in the vicinity of the front and behind the front, is affected. This would indicate that local fluid migration, controlled by the coefficient of permeability, directly influences the local intergranular stress conditions.
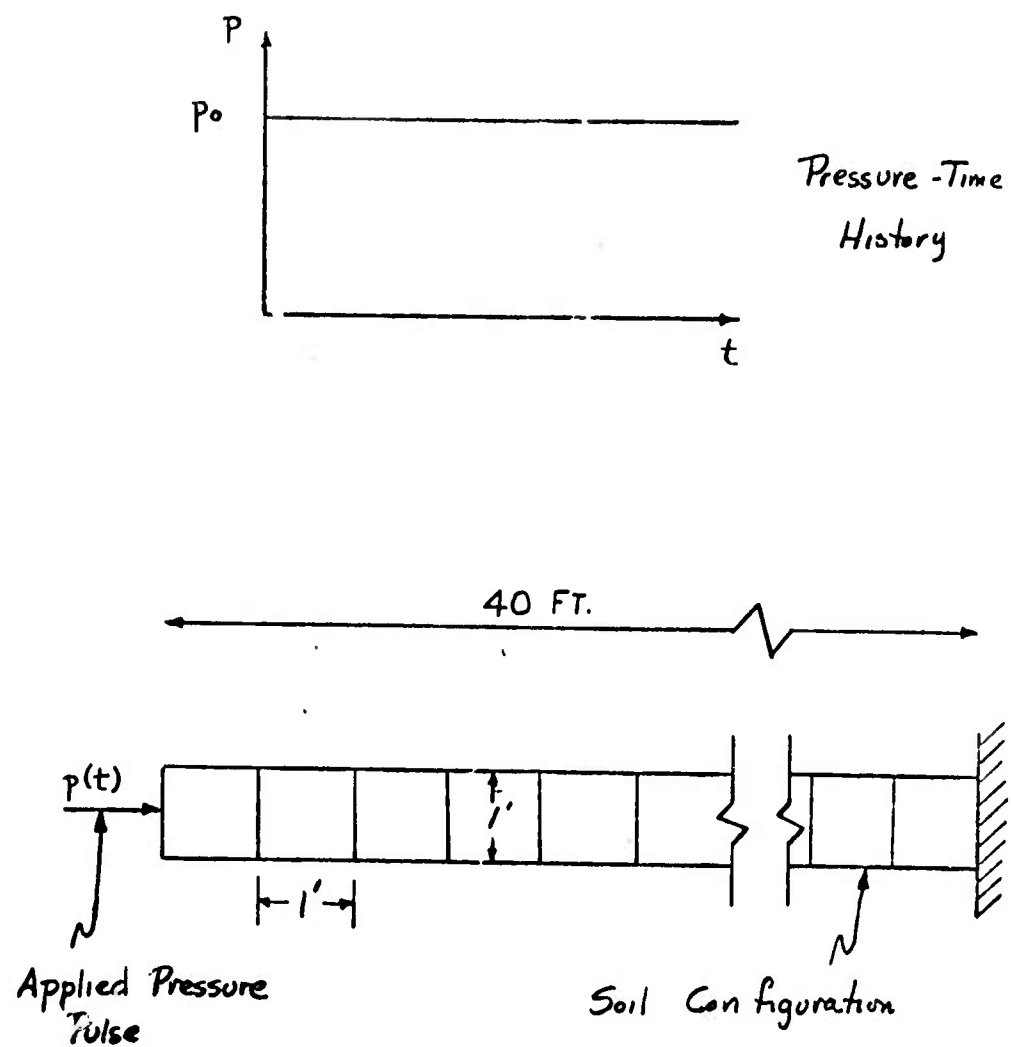
4.3

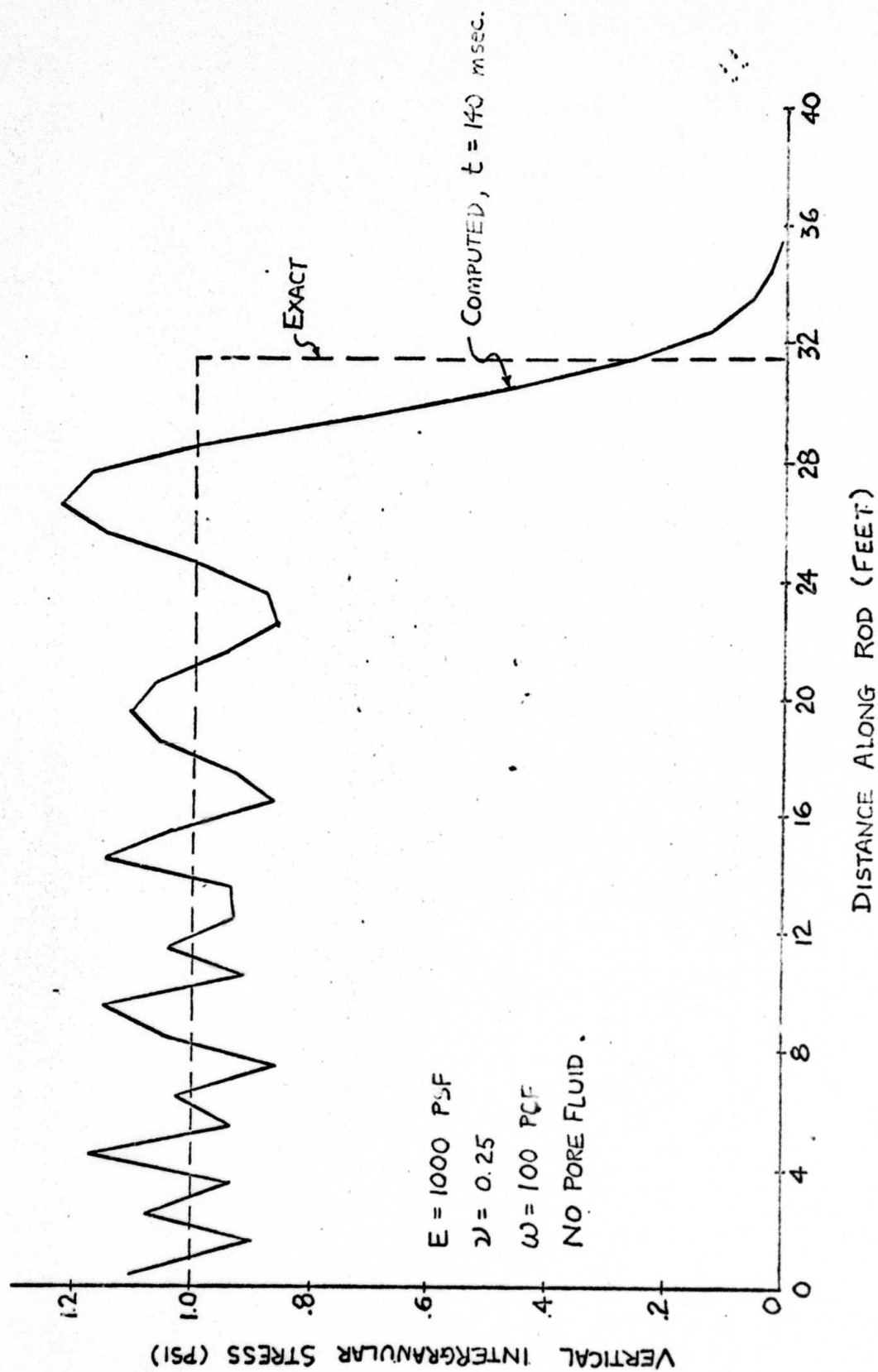Fig. 24. Configuration of Uniaxial Soil Model

4.4

Fig. 25. Stress Profile along Soil Column, No Pore Fluid

The figure plots VERTICAL INTERGRANULAR STRESS (PSI) against DISTANCE ALONG ROD (FEET), with curves labeled EXACT and COMPUTED, t = 140 msec.

Parameters:
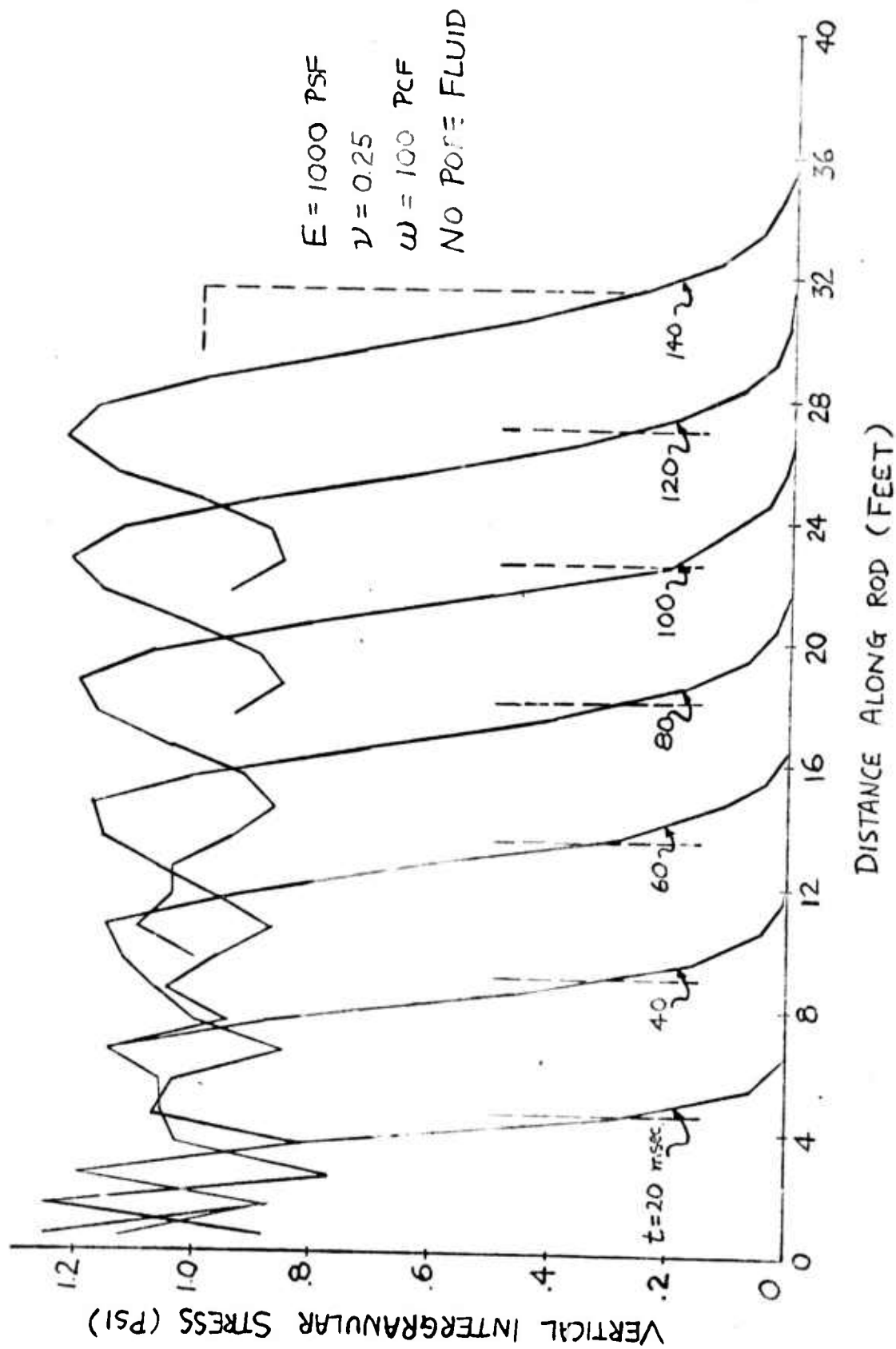E = 1000 PSF
ν = 0.25
ω = 100 PCF
NO PORE FLUID.

4.5

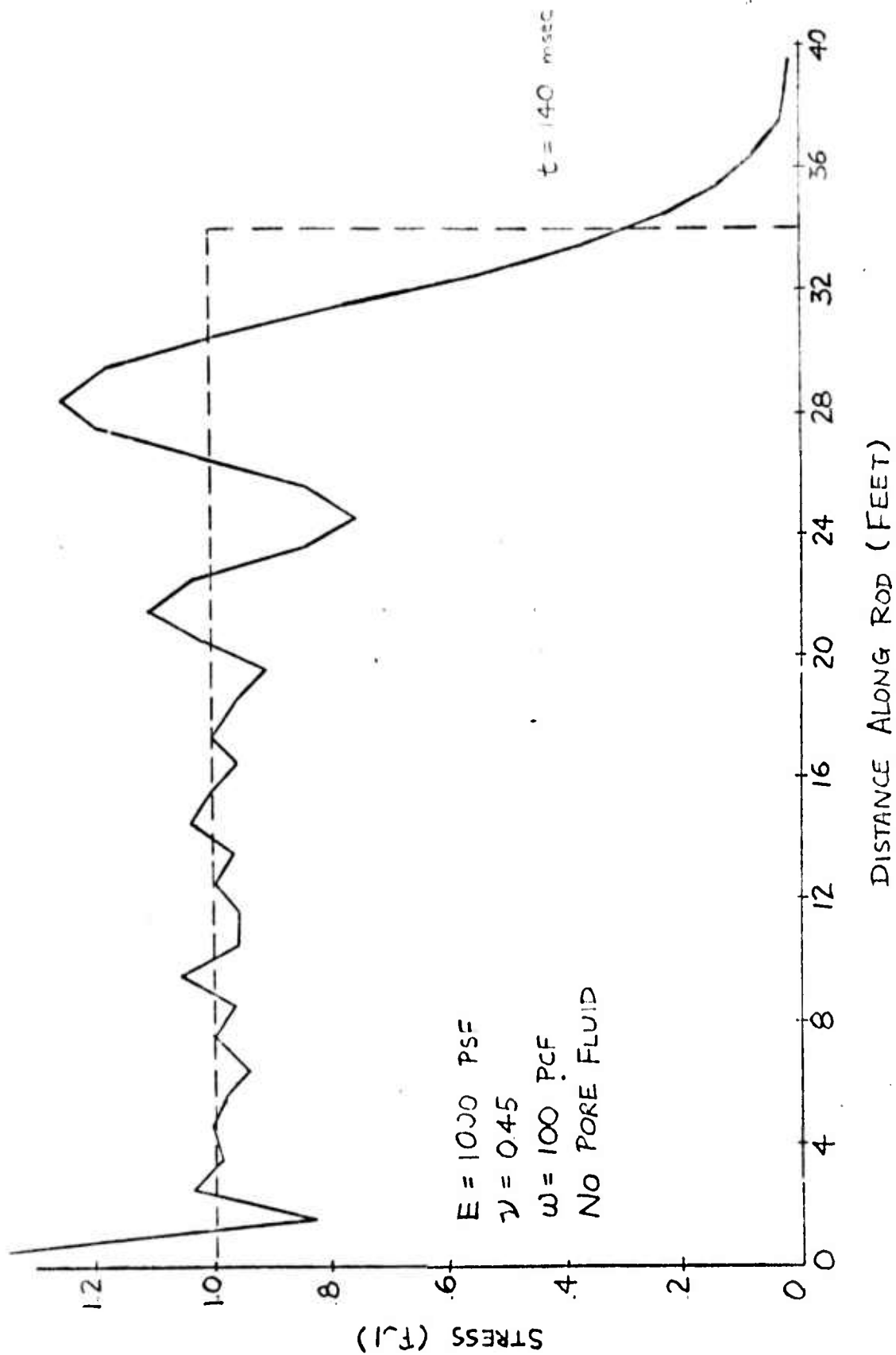Fig. 26 Wave Front Propagation Through Soil Column, No Pore Fluid

4.6
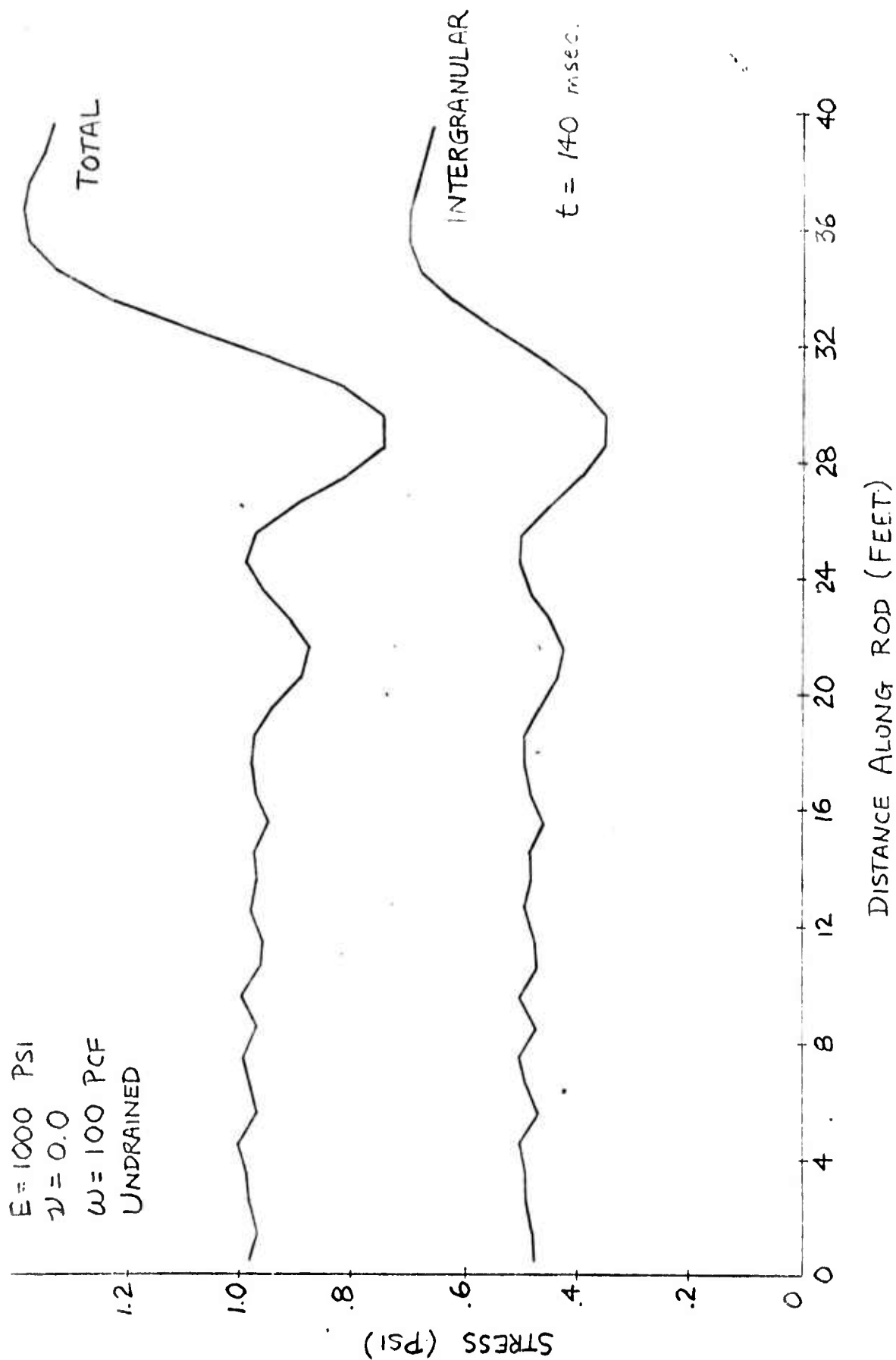
Fig. 27. Stress Profile Along Soil Column, No Pore Fluid

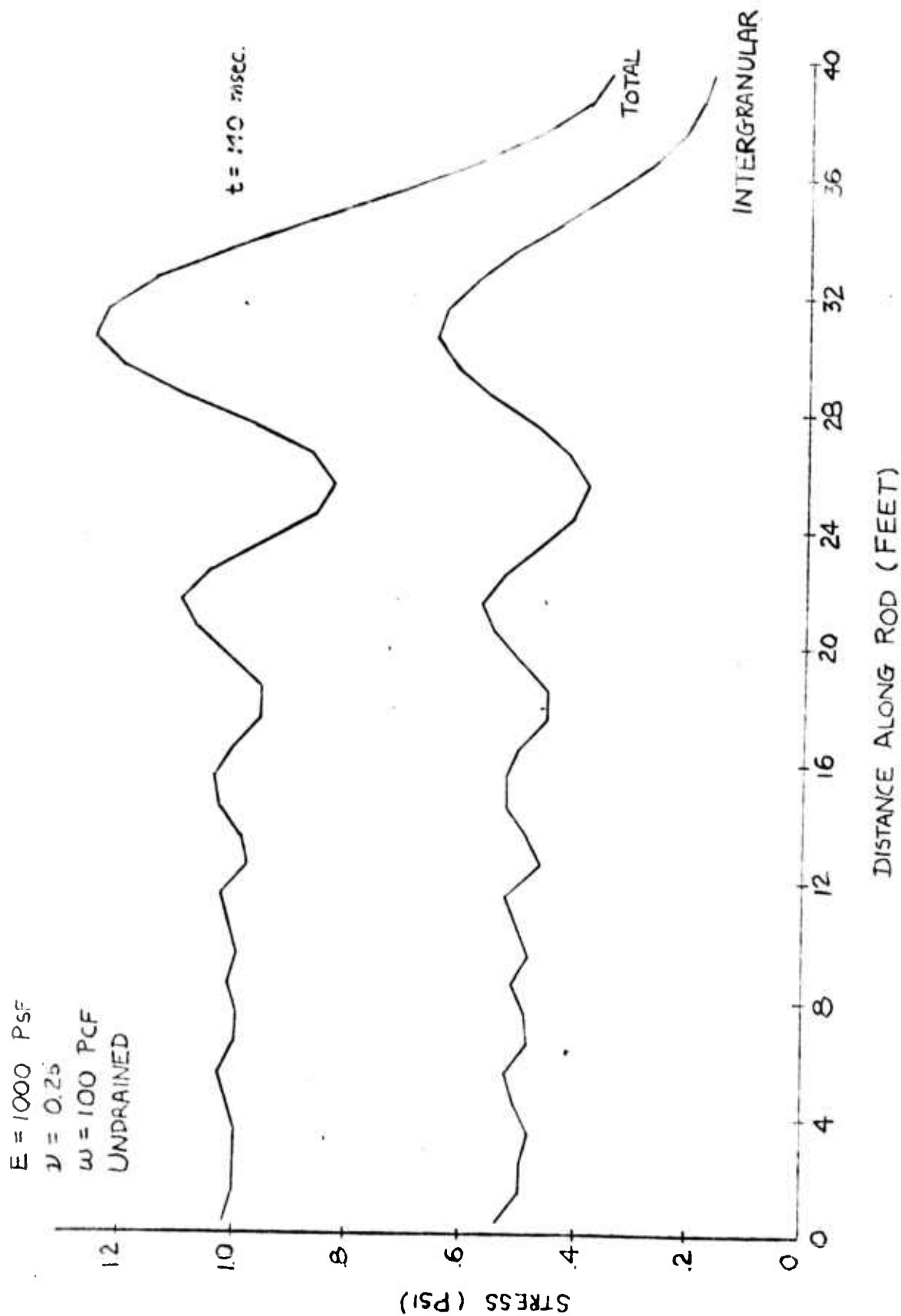4.7

Fig. 28. Stress Profile Along Soil Column with Pore Fluid

4.8

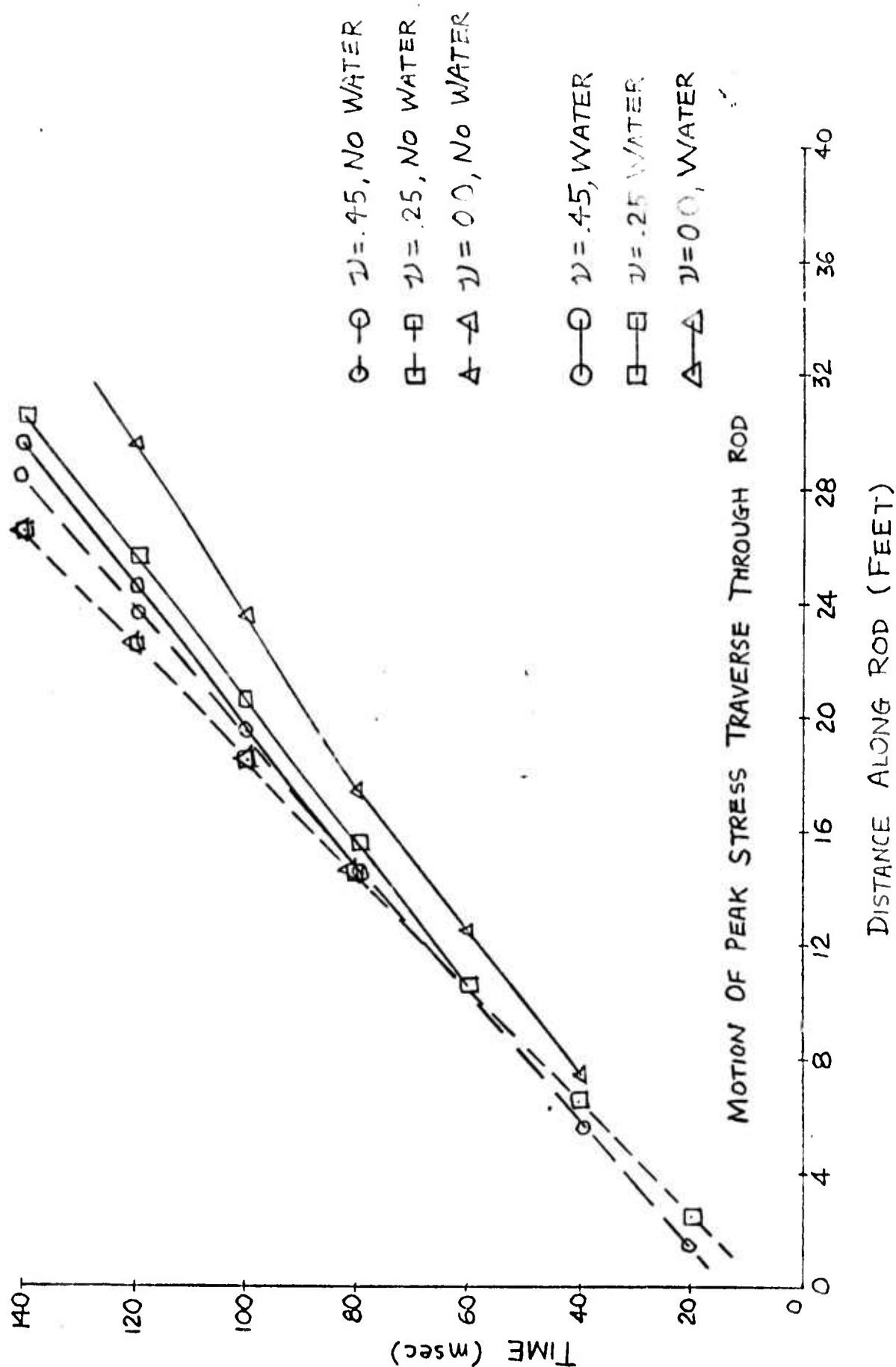Fig. 29 Stress Profile Along Soil Column with Pore Fluid

$E = 1000 \ Psf$
$\nu = 0.25$
$\omega = 100 \ Pcf$
UNDRAINED

$t = 110 \ msec.$

TOTAL

INTERGRANULAR

DISTANCE ALONG ROD (FEET)

STRESS (PSI)

TIME (msec)

140

120

100

80

60

40

20

0

$\nu = .45$, NO WATER
$\nu = .25$, NO WATER
$\nu = 00$, NO WATER
$\nu = .45$, WATER
$\nu = .25$, WATER
$\nu = 00$, WATER

0   4   8   12   16   20   24   28   32   36   40

DISTANCE ALONG ROD (FEET)

MOTION OF PEAK STRESS TRAVERSE THROUGH ROD

Fig. 30   Influence of Pore Fluid on Stress Wave Velocity
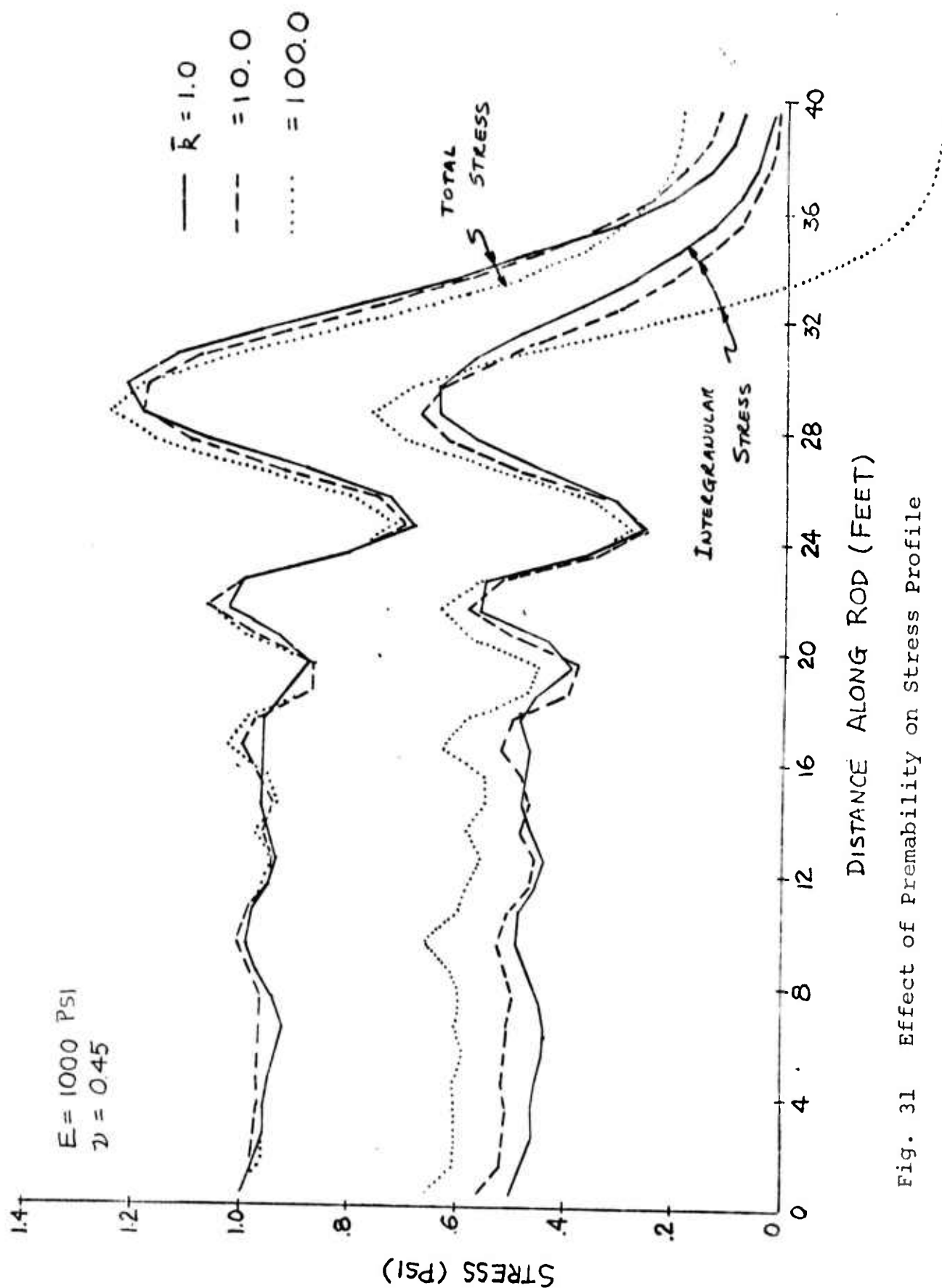
4.10

Fig. 31 Effect of Premability on Stress Profile

4.11

5.0 POTENTIAL FOR WATER WAVE INDUCED SOIL LIQUEFACTION

A problem of considerable interest for off-shore structures is the potential for liquefaction of soils due to storm waves traversing a site. If foundation soils liquefy, then obviously they lose strength and ability to support any applied loads. It is well known (Ref. 11) that pressure changes on the sea floor, associated with passage of an ocean wave, can cause shear failure in soft sediments, this shear failure developing from the effects of both water flow and reduced strength. In actual cases, the waves impose an oscillatory motion on the soft sediments, leading to repeated reversals of shear strength, remolding of the soil with an associated loss of strength.

For this study, an approach has been taken, based upon the combined stress-seepage analysis presented in Section 2.0, which may be used to establish the potential for liquefaction being induced in marine soils due to ocean storm waves. The configuration analyzed is shown in Figure 32, and consists of a half-space of submerged saturated soils to which a differential total stress is applied at the surface equal to the pressure differentials generated by the storm wave. In addition, an excess pore pressure distribution along the surface imposes a seepage condition aggravating the intergranular stress picture in the soil due to the seepage forces generated. In fact, this storm wave is traversing the site at a (say, constant) velocity so that the storm wave pressure distributions at any one location are functions of time.

5.1

An approximate approach to the problem is to freeze the wave at any instant of time and analyze the foundation response to steady load and seepage criteria. This approximation neglects the potential time lag effects which may occur in the foundation soil, but this effect cannot be too significant for pervious soils at the surface of the foundation. If this approach is utilized and if the soils are assumed to behave linearly, the infinite half-space problem can be reduced by required symmetry conditions to analyzing the restricted region shown in Figure 32.

5.1 Applied Pressure Condition

As mentioned above, the loading condition applied to the soil surface consists of equal amounts of total pressures and excess pore pressures. The excess pore pressures will induce seepage to occur from the area of the wave peak to the wave trough and the equal applied surface pressures are applied to maintain proper intergranular stress conditions. This last statement may be amplified by considering a uniform increase in the water level across the site, leading to a uniform increase in pore pressure along the soil surface. No seepage occurs for this condition, but the intergranular stress condition will change unless an equal surface loading is also applied.

As a wave passes a site, an increase in pressure, p, occurs below the crest, while beneath the trough there is a

pressure decrease, -p. The characteristics of the applied pressure pulse used in the analysis was taken as a sine function of the form

$$p = P_o \sin(2\pi x / D) \tag{40}$$

where p is the pressure increase at a given point, Po is the peak water pressure, and D is the wave length or distance between wave peaks. At any point, the corresponding pressure variation with time is

$$p = P_o \sin(2\pi t / T) \tag{41}$$

where T is the period of the wave. The relation between D and T is specified by

$$D = V T \tag{42}$$

where V is the velocity of the wave profile. The magnitude of the peak pressure change, P_o, which is in phase with the wave, depends on the wave length, the depth of water and the wave height. The actual pressure pulse applied by the ocean wave is complex, but using tables based upon linear wave theory (Ref. 12) the following parameters were used

$$
\begin{aligned}
P_o &= 600 \ \text{psf} \\
V &= 37 \ \text{fps} \\
T &= 14 \ \text{sec} \\
D &= 520 \ \text{ft}
\end{aligned}
\tag{43}
$$

5.3

These correspond to a storm wave of about 30 feet occurring in a water depth of about 50 feet. These parameters correspond to design conditions for near shore structures which may be placed on the East Coast.

5.2 Problems Investigated

Returning to Figure 32, the finite element mesh is used only in the region extending across one side of the loading wave, since by symmetry conditions the response on the other side of the loading wave can be deduced. For each soil site considered, two computer runs were generated, the first to obtain the in-situ stress conditions due to the bouyant unit weight of the soil and the second to determine the additional stresses due to the combined effects of the excess pore pressures (seepage stress effects) and applied surface pressures. The final output is then the total stress state due to both the initial and final load conditions. For inelastic soils, the load cycling effect could be estimated by alternating the sign of the applied wave loadings to determine growth of soil strain with time, while for elastic materials, this is not required.

For each phase of the problem, the specified boundary conditions used for the finite element mesh are as shown in Figure 33. For each problem, these conditions satisfy the required symmetry conditions imposed by freezing the wave motion. Three separate soil site configurations were investigated for this problem, in an attempt to estimate general liquefaction behavior, and these sites are shown in Figure 34. The first site consists of a pervious sand stratum overlying a relatively impervious clay

5.4

stratum, the second site consists of a sand/clay/sand configuration, and the third is a clay/sand/clay/sand site, these being typical of offshore sites. The loose surface sands are relatively mobile in that scouring effects transport these soils relatively easily.

For the problems investigated, the coefficients of permeability of the sands was taken to be about 200 times the coefficients of the clay strata. In addition, for each soil layer, the horizontal coefficient of permeability was assumed to be 5 times larger than the vertical coefficient, these values again being rather typical for these soils. For sites 1 and 2, with the surface sand layer, it can be anticipated that the majority of the flow pattern will take place through the sands, leading to large seepage pressures through this zone. In addition, for site 2, a variation of parameter study was made, varying the permeability ratios for the sand/clay strata to determine their effect on liquefaction potential.

5.3 Definition of Liquefaction Potential

For any problem investigated, states of intergranular stress and excess pore pressure distribution can be determined. The problem remaining is to interpret these stress data to determine if any portion of the soil is at or near its peak shear strength. If the computed intergranular stress states are relatively small in comparison to the available soil strength, it can be anticipated that excess strength is available and no liquefaction could take place. If the stress states exceed the available strength, liquefaction obviously occurs and no additional

5.5

strength is available in general to support additional structural loads.

A typical way of defining available strength is to use the Coulomb-Mohr failure criteria defined by equation 18, or

$$\alpha \, J_1 + \sqrt{J_2'} = k$$

(44)

where J_1 is the hydrostatic stress invariant, J_2' is the deviatoric stress invariant (effective shear strength) and the parameters α and k are related to the usual strength parameters, C and $\emptyset$, obtained from a triaxial test series, and are defined by equation 20. This form of the strength law leads to the usual linear Mohr strength envelope used in soil testing and analysis. If an intergranular stress state is specified at a point, the hydrostatic invariant can be computed, and the "available shear strength" defined by

$$\left(\sqrt{J_2'}\right)_{AVAIL} = k - \alpha \, J_1$$

(45)

Comparing this value with the actual applied deviator stress, $\left(\sqrt{J_2'}\right)_{APPLIED}$, one can assess if the stress state is at or near failure. An obvious factor of safety can then be defined as

$$S.F = \left(\sqrt{J_2'}\right)_{AVAIL} \Big/ \left(\sqrt{J_2'}\right)_{APPLIED}$$

(46)

If this factor is near unity, it can be anticipated that no significant strength is available to support structural loads, and liquefaction has occurred.

5.6

5.4 Numerical Results

The finite element mesh used for Site No. 1 is shown in Figure 35, and consists of a relatively uniform mesh. The excess pore pressure distribution pattern is shown in Figure 36, and indicates the magnitude of the pore pressures developed by the ocean wave above the ambient pore pressure condition. Obviously, by symmetry, the pore pressures pattern on the other side of the right boundary of the mesh is just the mirror image of the pattern shown. The horizontal displacement profile under the positive wave is shown in Figure 37 and generally indicates that under this portion, the horizontal stress increments developed by the wave are tensile and tend to reduce the confinement of the soil. Under the negative portion of the wave, the opposite would be true.

The corresponding vertical stress increment due to the storm wave is shown in Figure 38 and as may be noted are relatively small. Similarly shear stresses (Fig. 39) are small. The major effect is then to generate lateral tensile stresses under the crest of the wave, as shown in Figure 42, in the top sand layer. A comparison of available strength with applied effective shear stress is shown in Figure 43, and, as may be noted, near the surface of the sand layer, the available strength approaches the used strength indicating a low factor of safety.

Similar data for Site No. 2 is shown in Figures 44 to 48, with the same general properties of the stress state. Near the surface of the top sand layer, the safety factor approaches 1.0, and in fact under the crest of the wave (left boundary) the

safety factor becomes less than 1.0. For Site No. 3 (Figs. 49 to 54), similar results are obtained with the exception that the safety factors in the top clay and sand layers are higher than those in the previous problems. This indicates that the pore pressure dissipation through the top clay layer is sufficient to reduce the pore pressures and thus radial stress increments in the sand layer which is most susceptible to the pore pressure effects.

As mentioned previously, a variation of parameter study was made for Site No. 2, varying the both the ratio of sand to clay permeabilities as well as the ratio of horizontal to vertical permeabilities. In Figure 55, the safety factor profile under the crest of the wave (left boundary) is shown as a function of depth as the ratio of sand to clay permeability was varied from 1 to 200. In the cases investigated, this crest boundary led to the lowest factor of safety. As may be noted, the safety factors decreased as the ratio increased (more flow restricted to the top sand layer). For this problem, the entire surface sand layer liquefies (or loses all its strength). Figure 56 shows similar data for a variation of horizontal to vertical permeability in each layer. As may be noted, this parameter does not significantly alter the results.
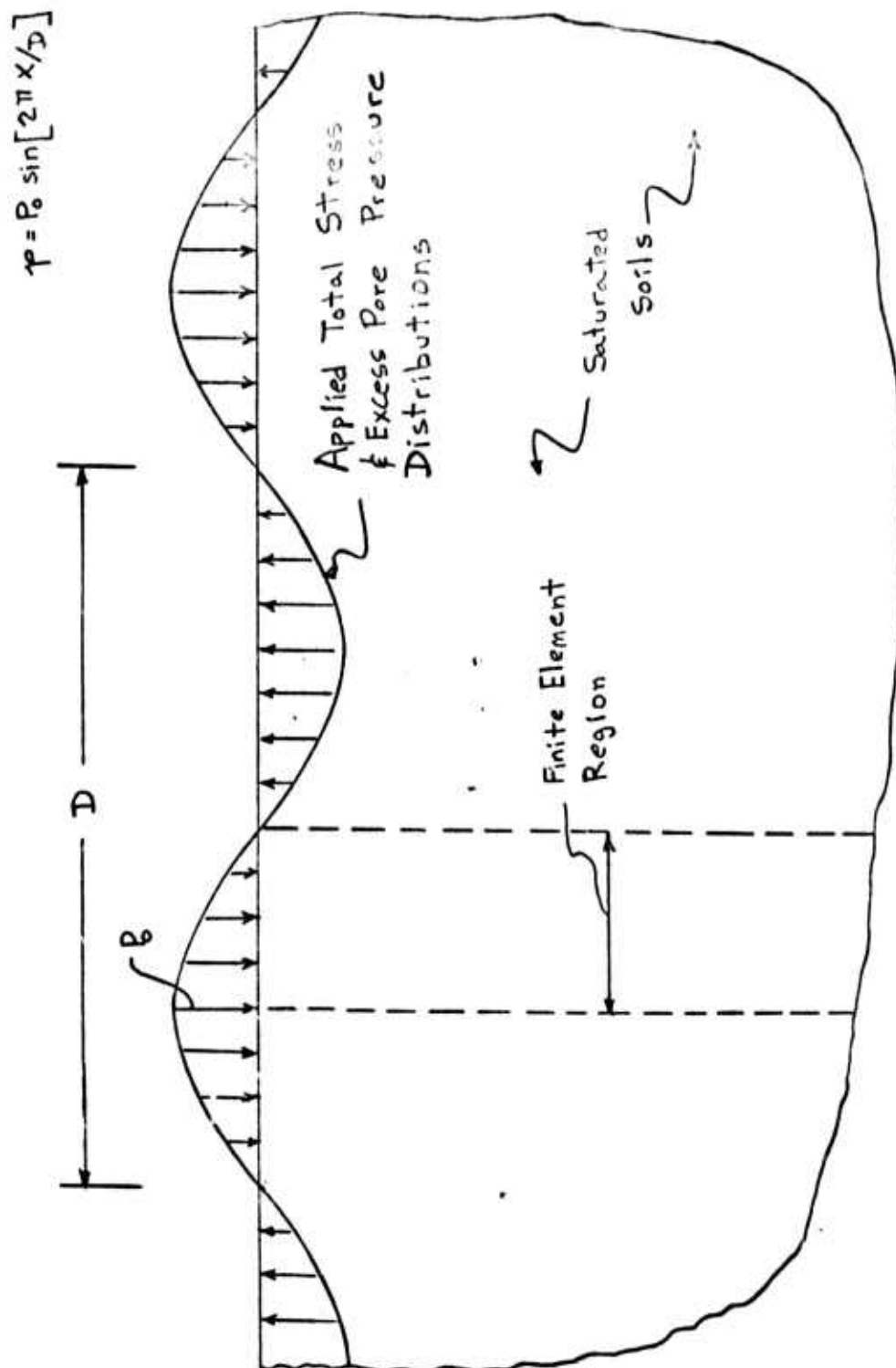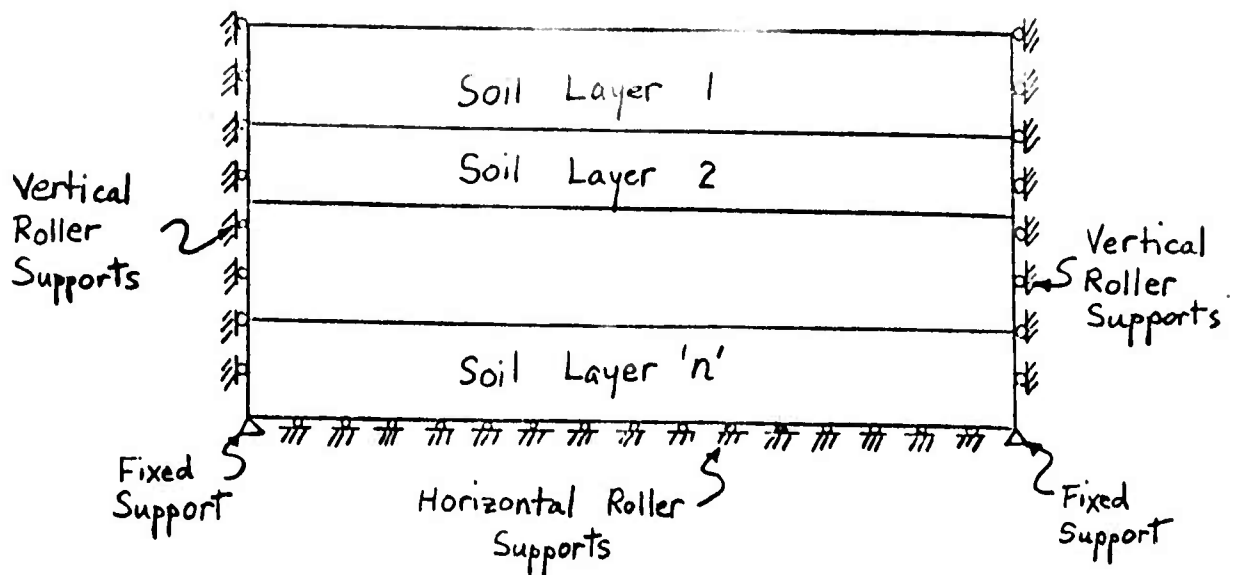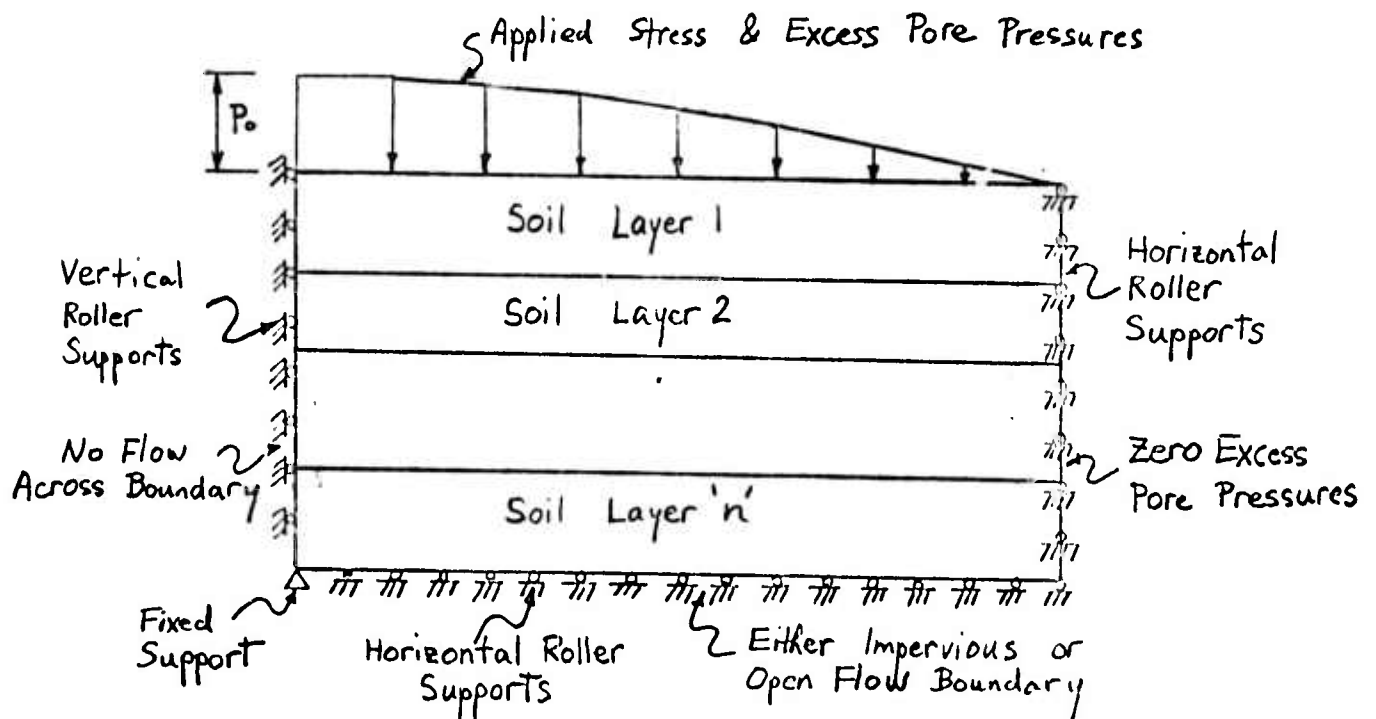
Fig. 32- Two Dimensional Steady State Loading Configuration

(a) Boundary Conditions for Initial Stress Conditions, No Excess Pore Pressures

(b) Boundary Conditions for Additional Stresses Caused by Water Waves.

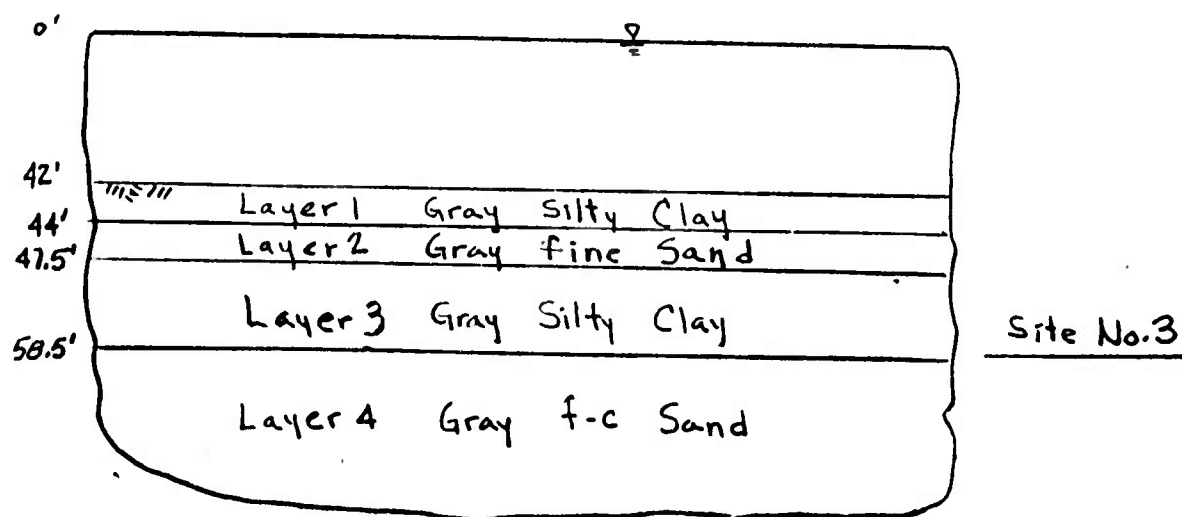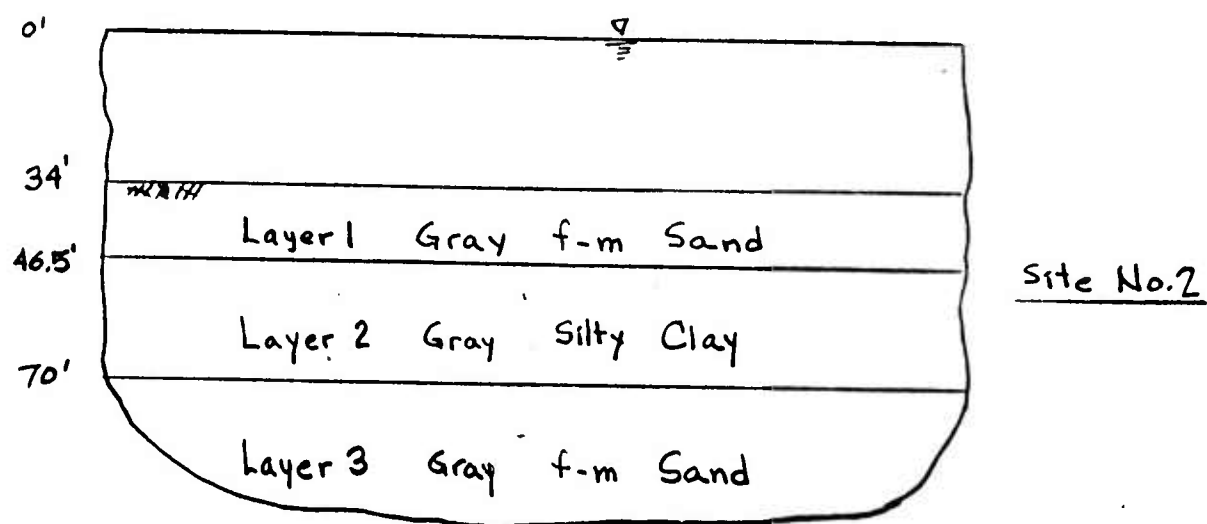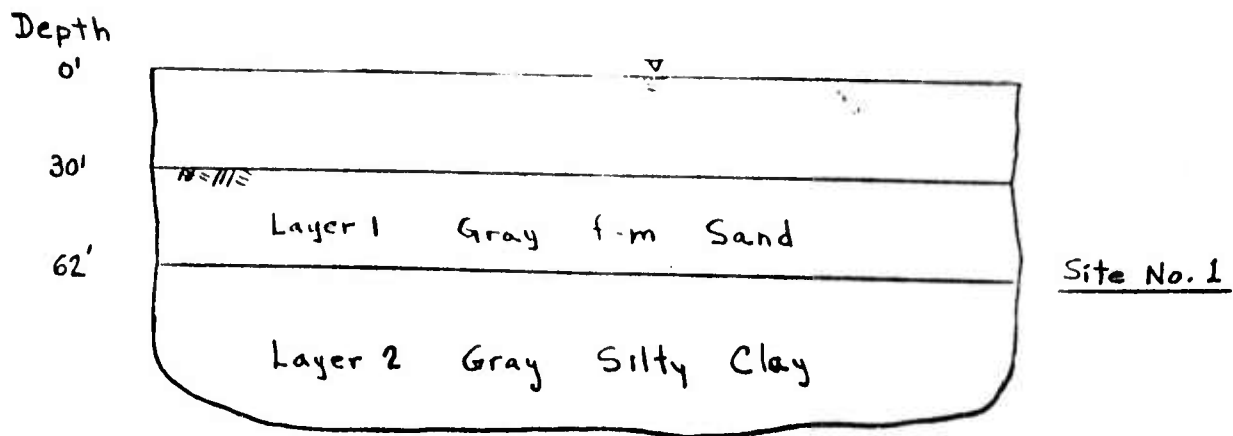Fig. 33- Two Stage Problem Boundary Conditions

Site No. 1

Depth
- 0'
- 30'
- 62'

Layer 1   Gray   f-m   Sand

Layer 2   Gray   Silty   Clay

Site No. 2

- 0'
- 34'
- 46.5'
- 70'

Layer 1   Gray   f-m   Sand

Layer 2   Gray   Silty   Clay

Layer 3   Gray   f-m   Sand

Site No. 3

- 0'
- 42'
- 44'
- 47.5'
- 58.5'

Layer 1   Gray   Silty   Clay

Layer 2   Gray   fine   Sand

Layer 3   Gray   Silty   Clay

Layer 4   Gray   f-c   Sand

Fig. 34- Site Configurations Investigated

5.11

4 @ 8' = 32'

2 @ 9' = 18'

Impervious Boundary

13 @ 10' = 130'

Soil Layer No. 1

Soil Layer No. 2

Depth 30'

62'

60'

Soil Layer 1
Gray f-m SAND
$E = 8 \times 10^5$ Psf
$\nu = 0.35$
$\gamma_{bouy} = 56$ Pcf
$k_V = 10$ ft/day
$k_H = 50$ ft/day

Soil Layer 2
Gray Silty CLAY
$E = 4 \times 10^5$ Psf
$\nu = 0.45$
$\gamma_{bouy} = 48$ Pcf
$k_V = 0.05$ ft/day
$k_H = 0.25$ ft/day
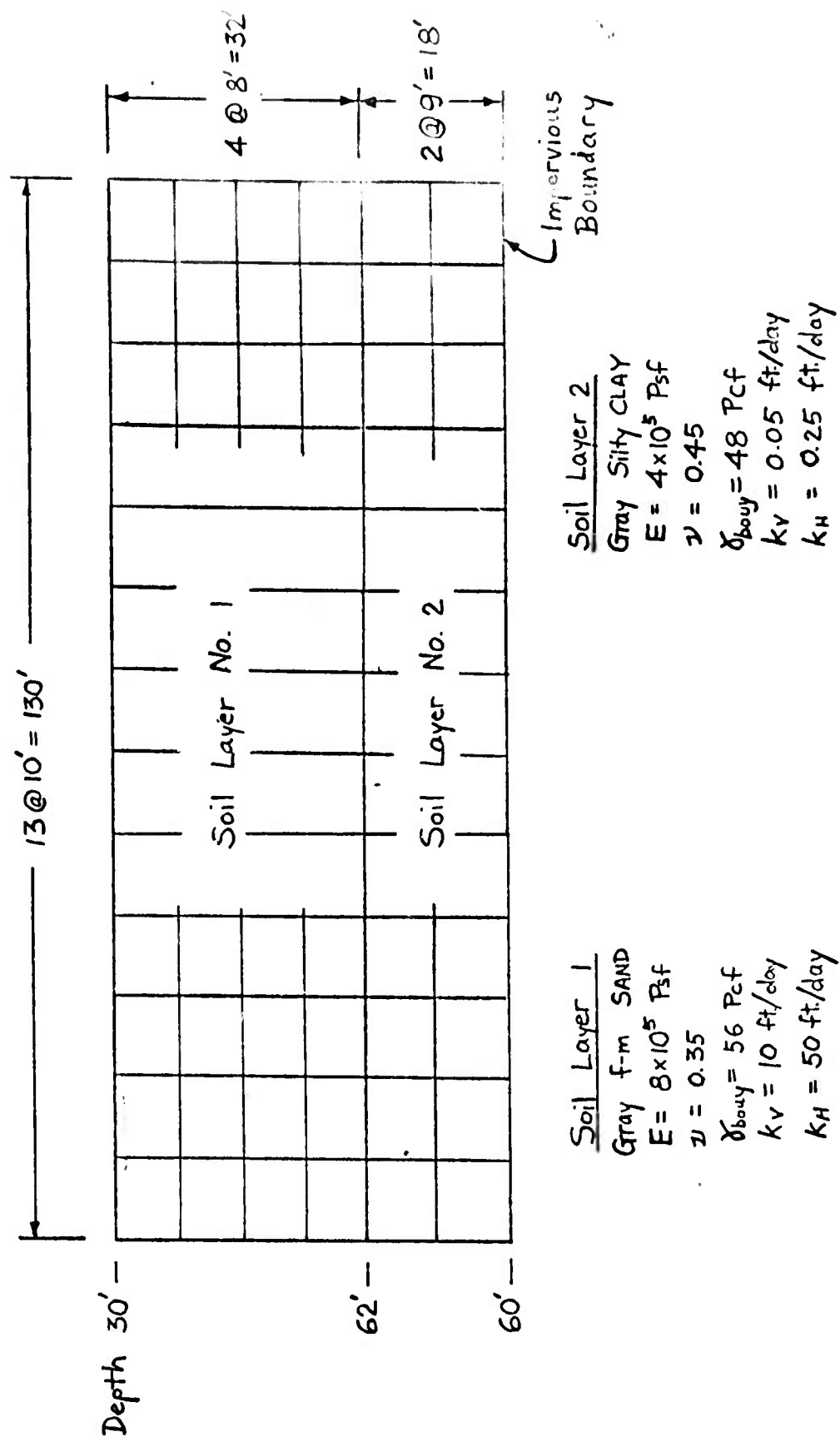
Fig. 35- Finite Element Mesh for site No. 1

5.12
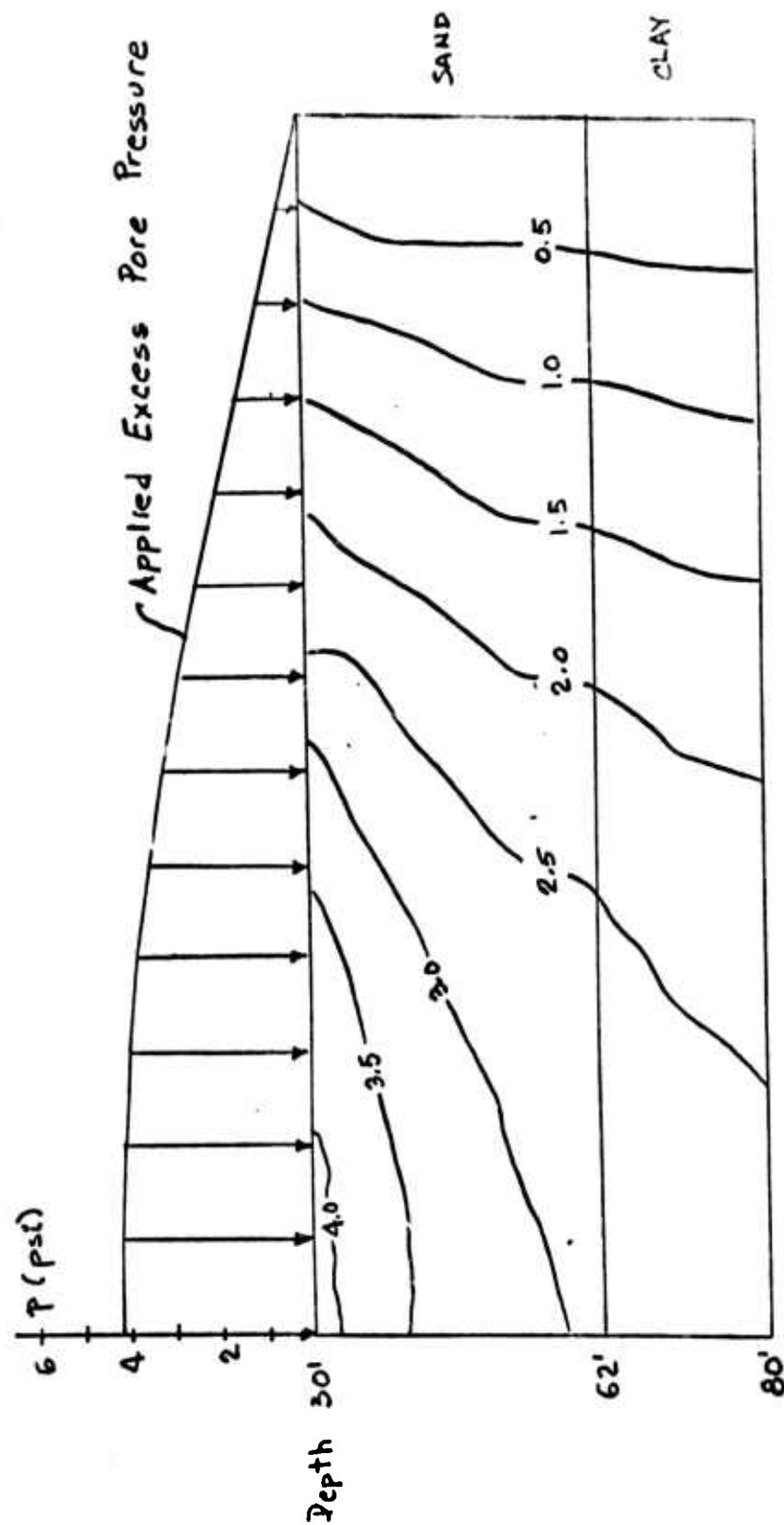
Fig. 36– Excess Pore Pressure Distribution, Site No. 1
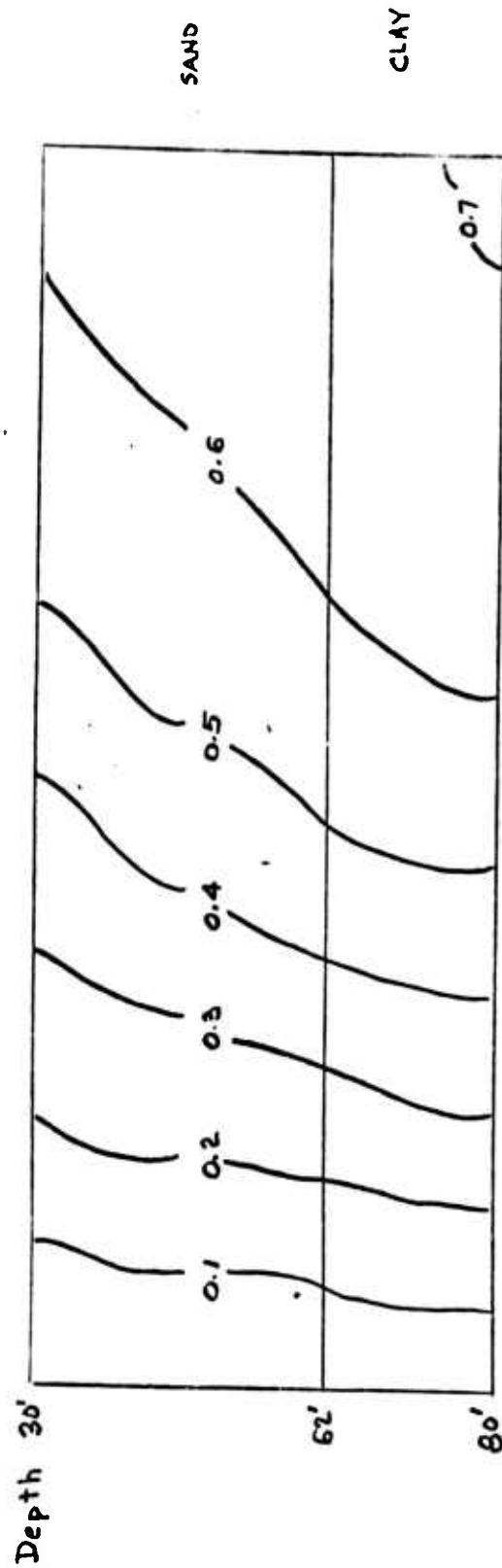
Fig. 37— Horizontal Displacement Profile (Inches)   Site No. 1
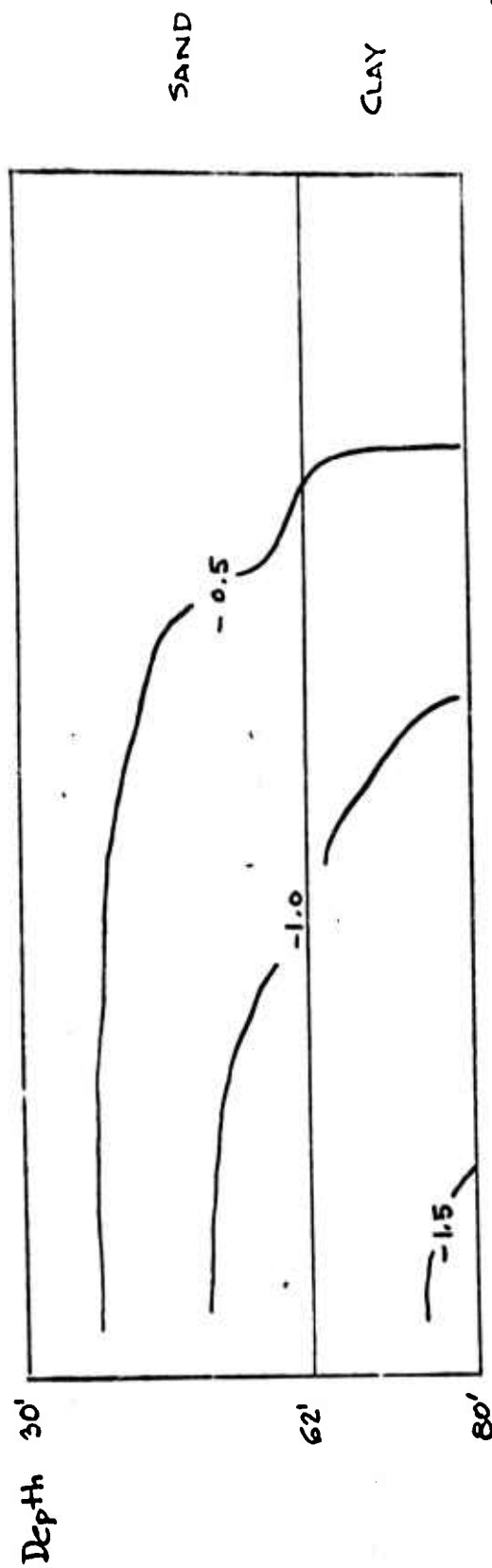
Fig. 38- Vertical Intergranular Stress Increment (Psi)   Site No. 1
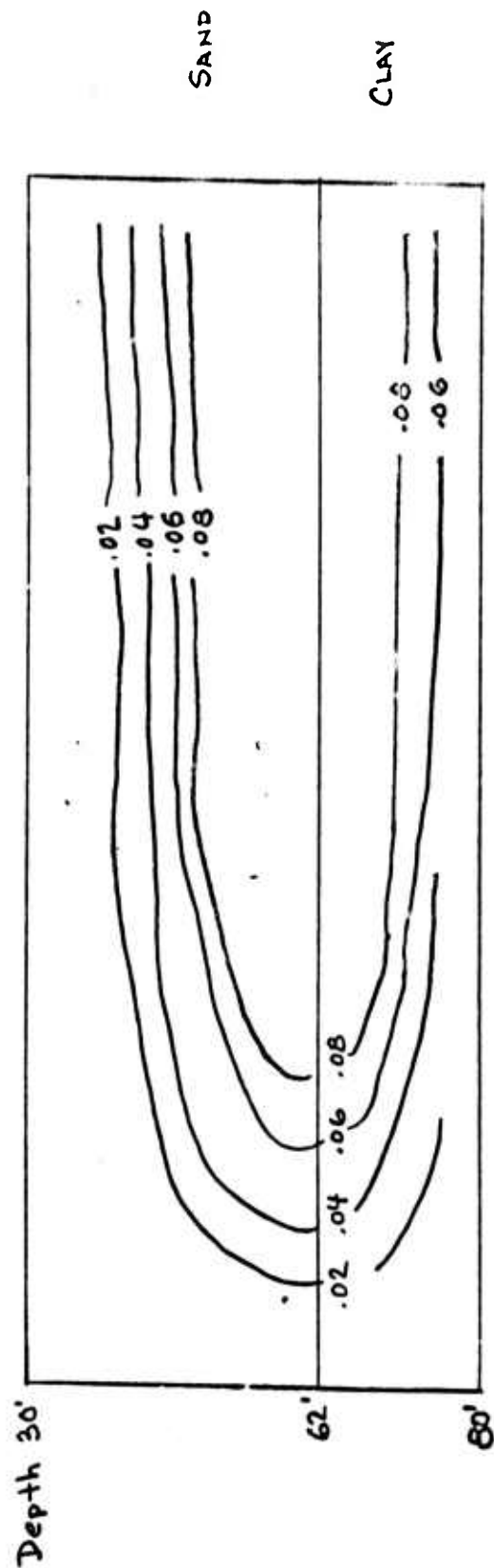
5.15

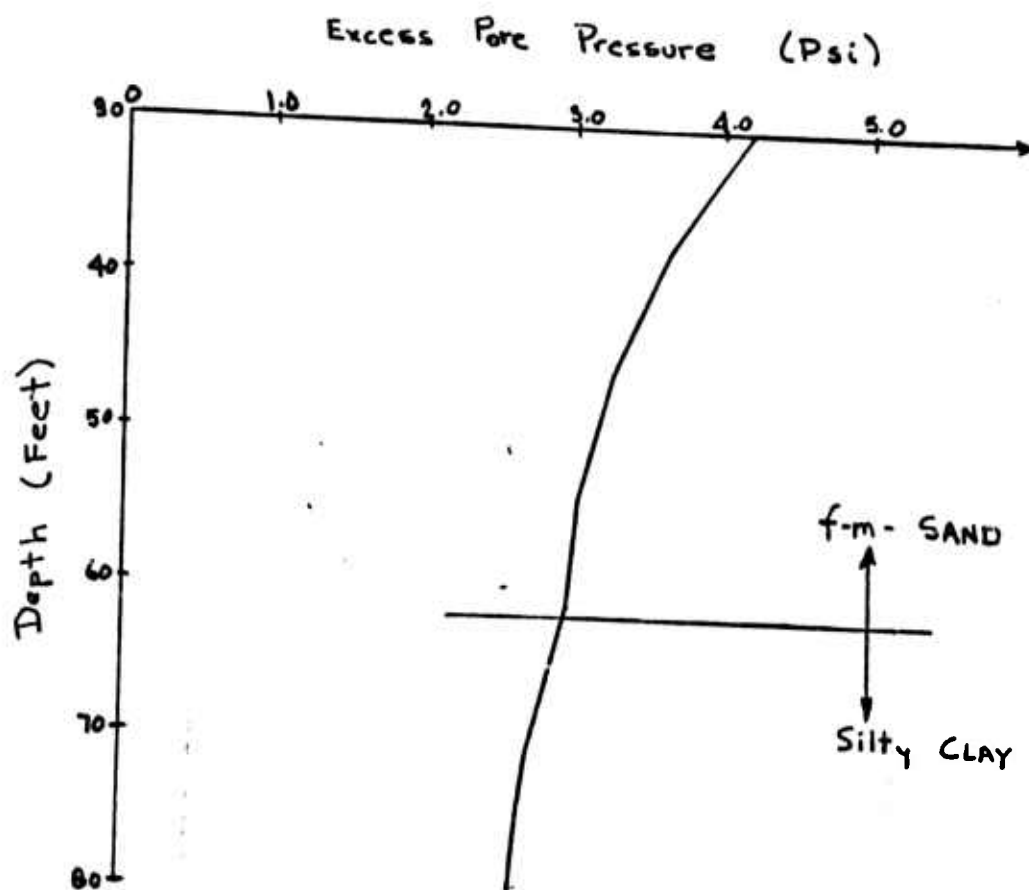Fig. 39   Shear Stress Distribution (Psi)   Site No. 1

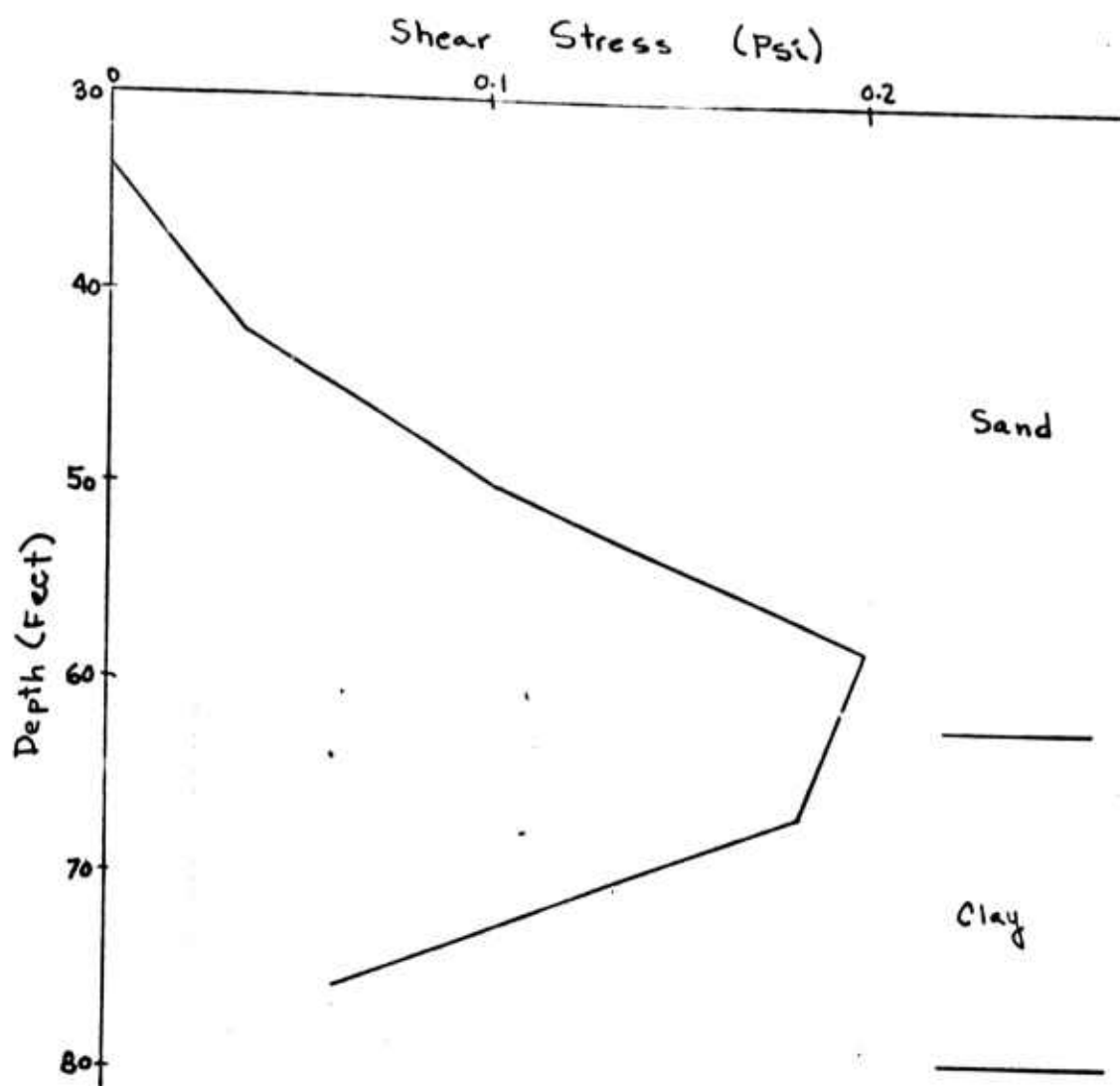Fig. 40- Excess Pore Pressures, Left Boundary, Site No. 1
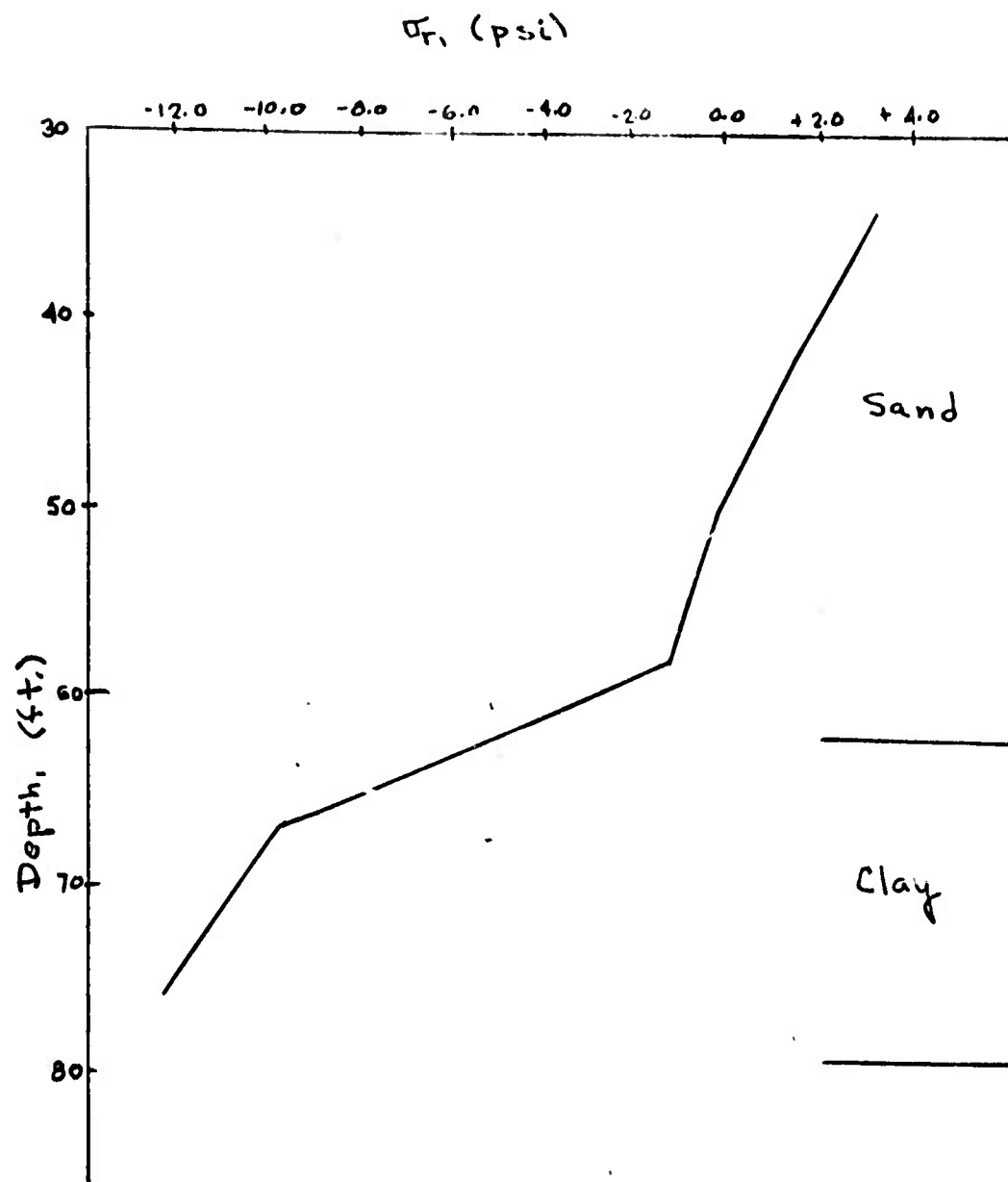
Fig. 41- Shear Stress, Right Boundary, Site No. 1

5.18

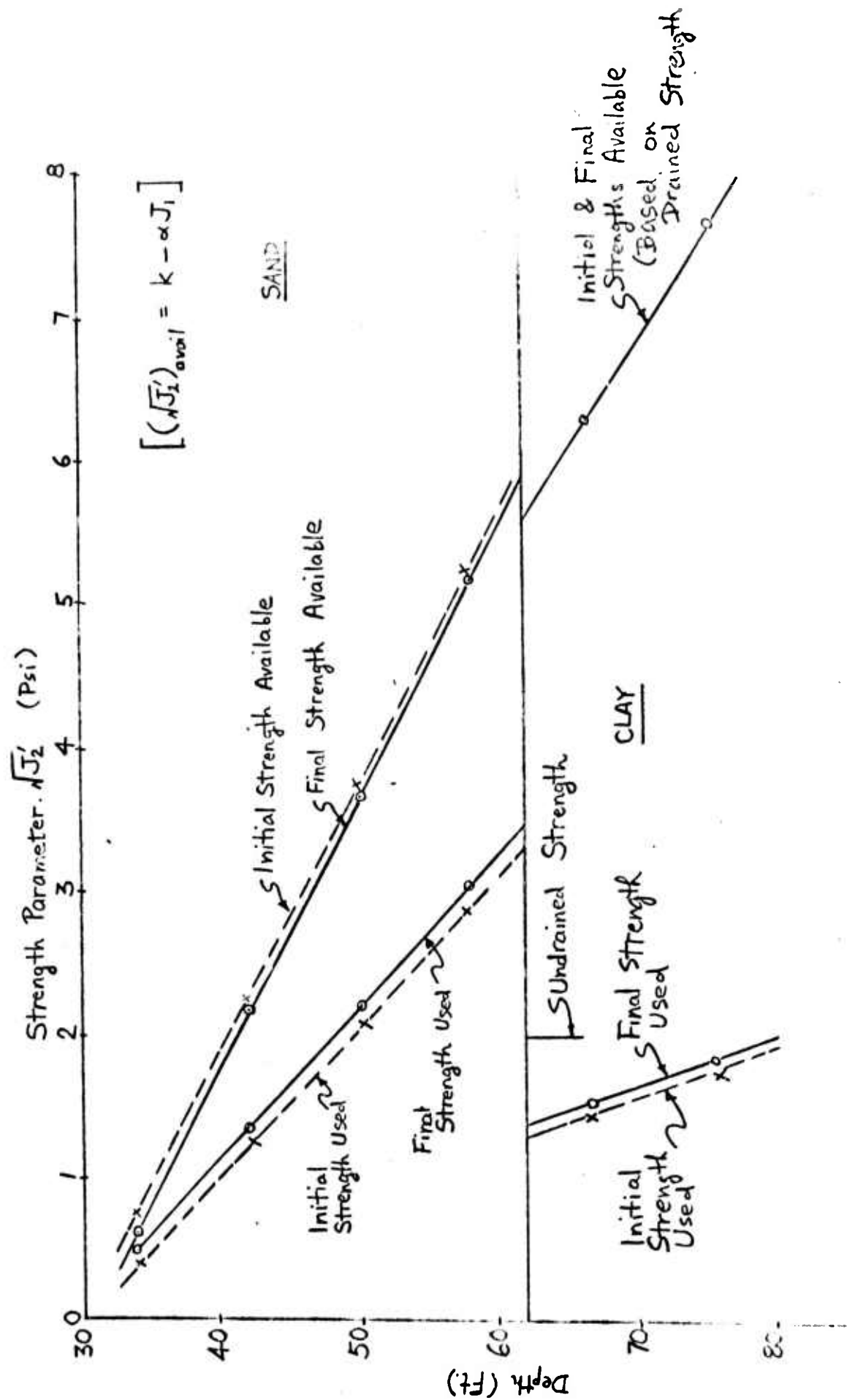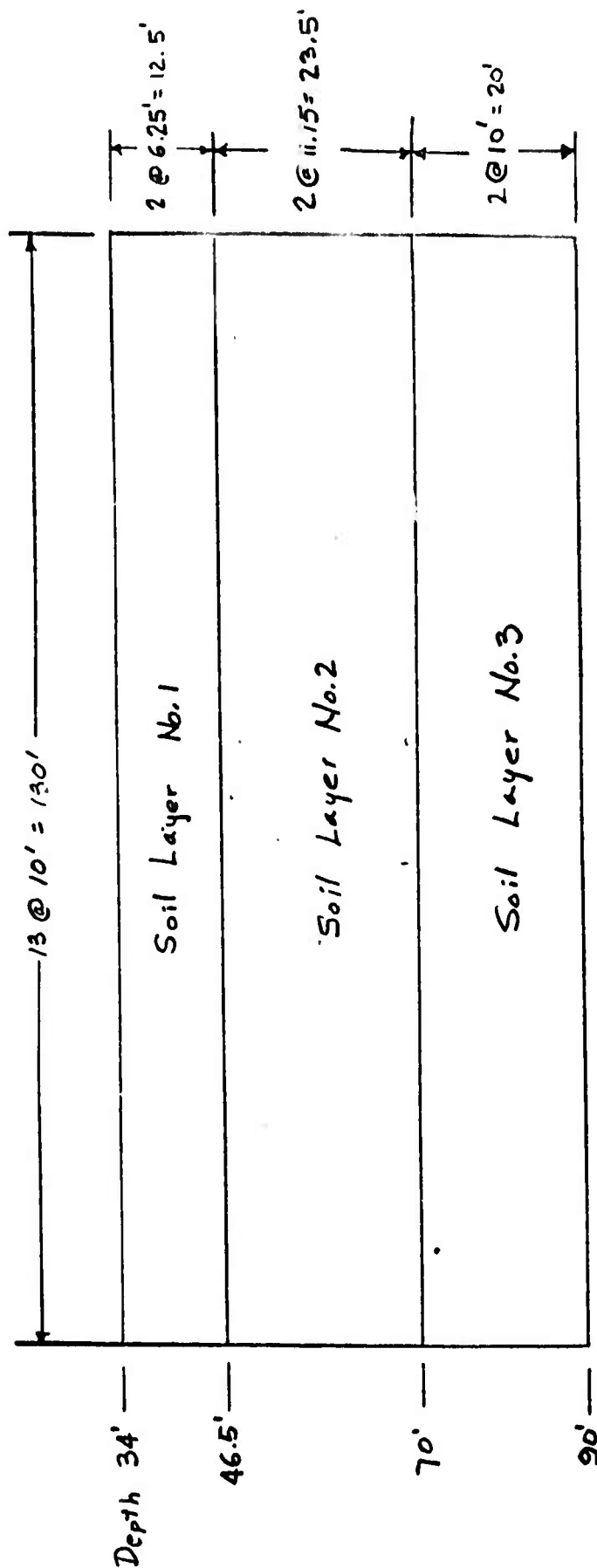Fig. 42- Radial Stress vs. Depth - Left Boundary - Site No.1

Fig. 43- Shear Strength Parameter, Right Boundary,   Site No.1

5.20

13 @ 10' = 130'

Depth 34'

46.5'

70'

90'

2 @ 6.25' = 12.5'

2 @ 11.75 = 23.5'

2 @ 10' = 20'

Soil Layer No.1

Soil Layer No.2

Soil Layer No.3

Soil Layer 1
Gray f-m SAND
$E = 8 \times 10^5$ Psf
$\nu = 0.35$
$\gamma_{bouy} = 56$ pcf
$k_v = 10$ ft/day
$k_H = 50$ ft/day

Soil Layer 2
Gray Silty CLAY
$E = 4 \times 10^5$ Psf
$\nu = 0.45$
$\gamma_{bouy} = 48$ Pcf
$k_v = 0.05$ ft/day
$k_H = 0.25$ ft/day

Soil Layer 3
Gray f-m SAND
$E = 10 \times 10^6$ Psf
$\nu = 0.35$
$\gamma_{bouy} = 56$ Pcf
$k_v = 10$ ft/day
$k_H = 50$ ft/day
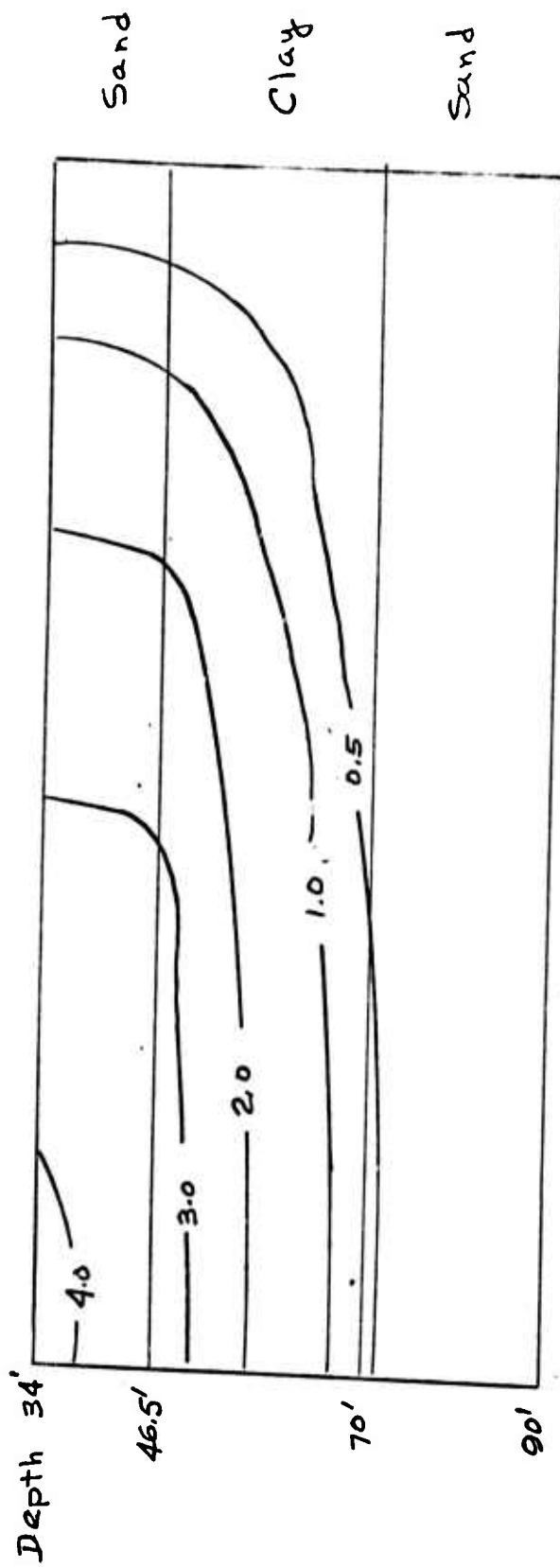
Fig. 44- Soil Property Data, Site No.2

5.21

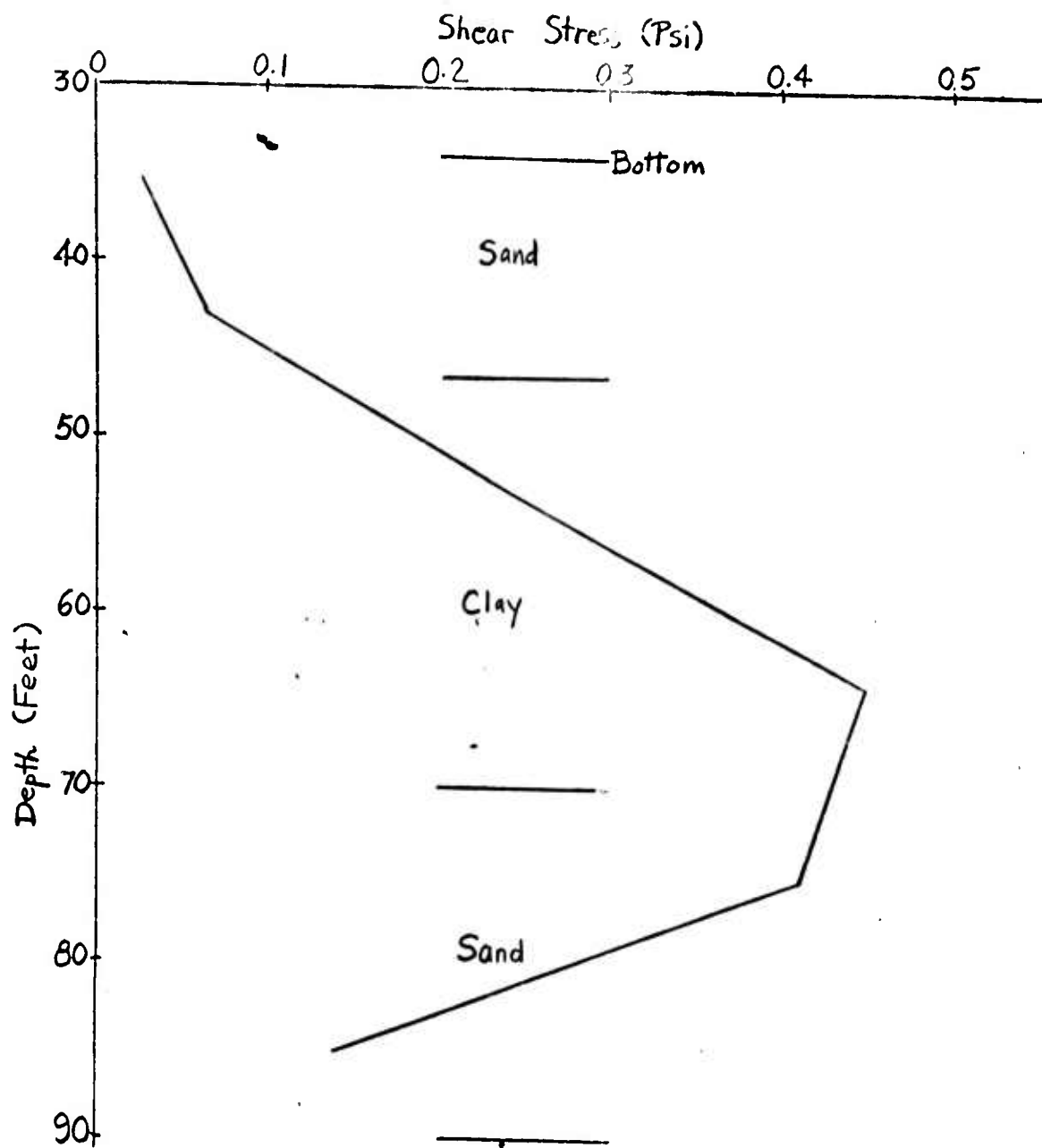Fig. 45- Excess Pore Pressure Distribution (Psi) . Site No.2

5.22

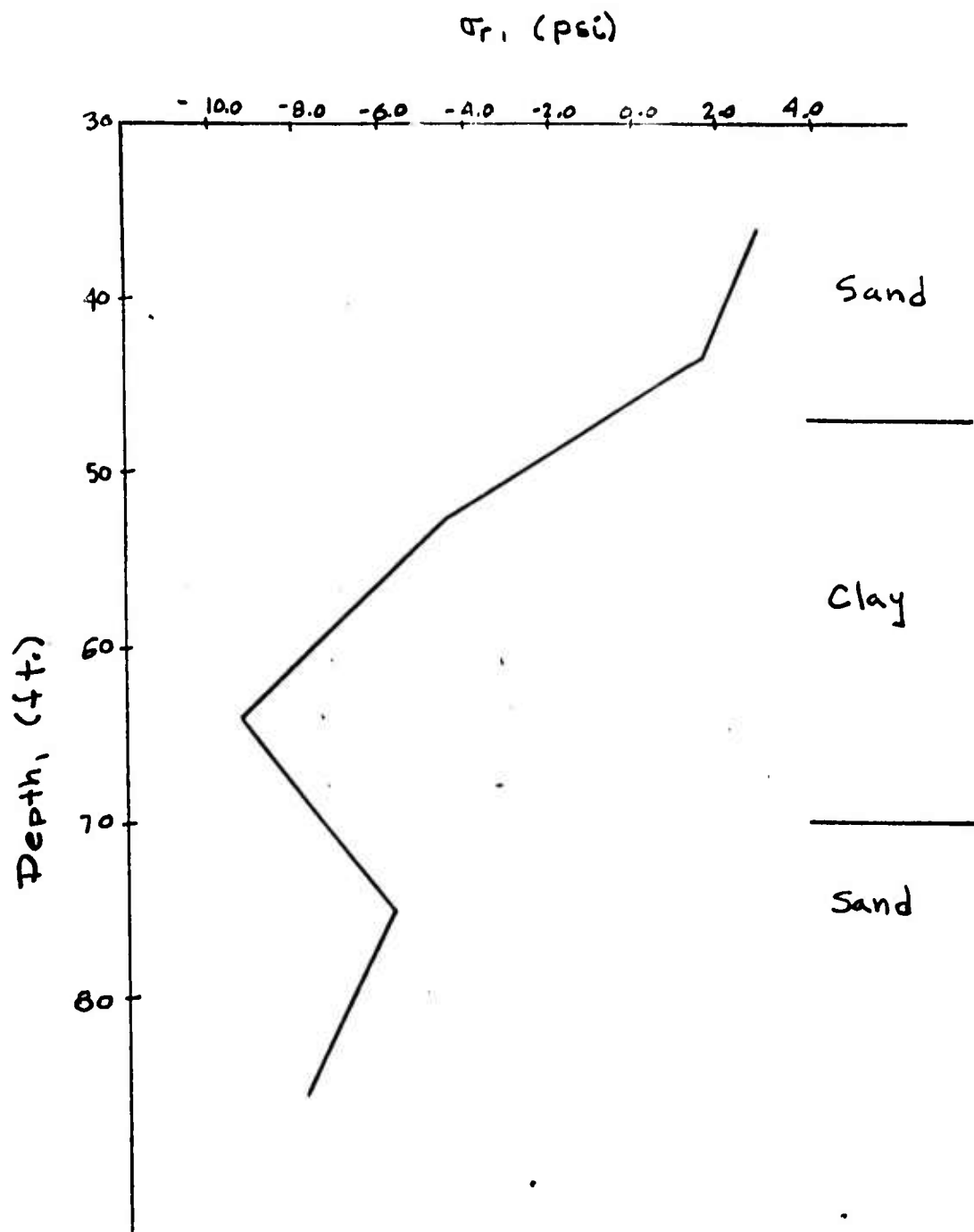Fig. 46- Shear Stress Distribution, Right Boundary, Site No.**2**

Fig. 47- Radial Stress vs. Depth, Left Boundary, Site No.2

5.24

Fig. 48- Shear Strength Parameter, Right Boundary, Site No.2

5.25

Fig. 49- Soil Property Data, Site No.3

Depth 42'
44'
47.5'
58.5'
70.5'

13@10' = 130'

5@2'
1@3.5'
2@5.5'
2@10'

Soil Layer 1
Soil Layer 2
Soil Layer 3
Soil Layer 4

Soil Layer 1
Gray Silty Clay
$E = 4 \times 10^5$ Psf
$\nu = 0.45$
$\gamma_{buoy} = 48$ Pcf
$k_v = 0.05$ ft/day
$k_H = 0.25$ ft/day

Soil Layer 2
Gray f. Sand
$E = 8 \times 10^5$ Psf
$\nu = 0.35$
$\gamma_{buoy} = 56$ Pcf
$k_v = 10$ ft/day
$k_H = 50$ ft/day

Soil Layer 3
Gray Silty Clay
(Same as 1)

Soil Layer 4
Gray f-c Sand
$E = 10 \times 10^5$ Psf
$\nu = 0.35$
$\gamma_{buoy} = 56$ Pcf
$k_v = 10$ ft/day
$k_H = 50$ ft/day

Fig. 50- Excess Pore Pressure Distribution (Psi)   Site No.3

5.27
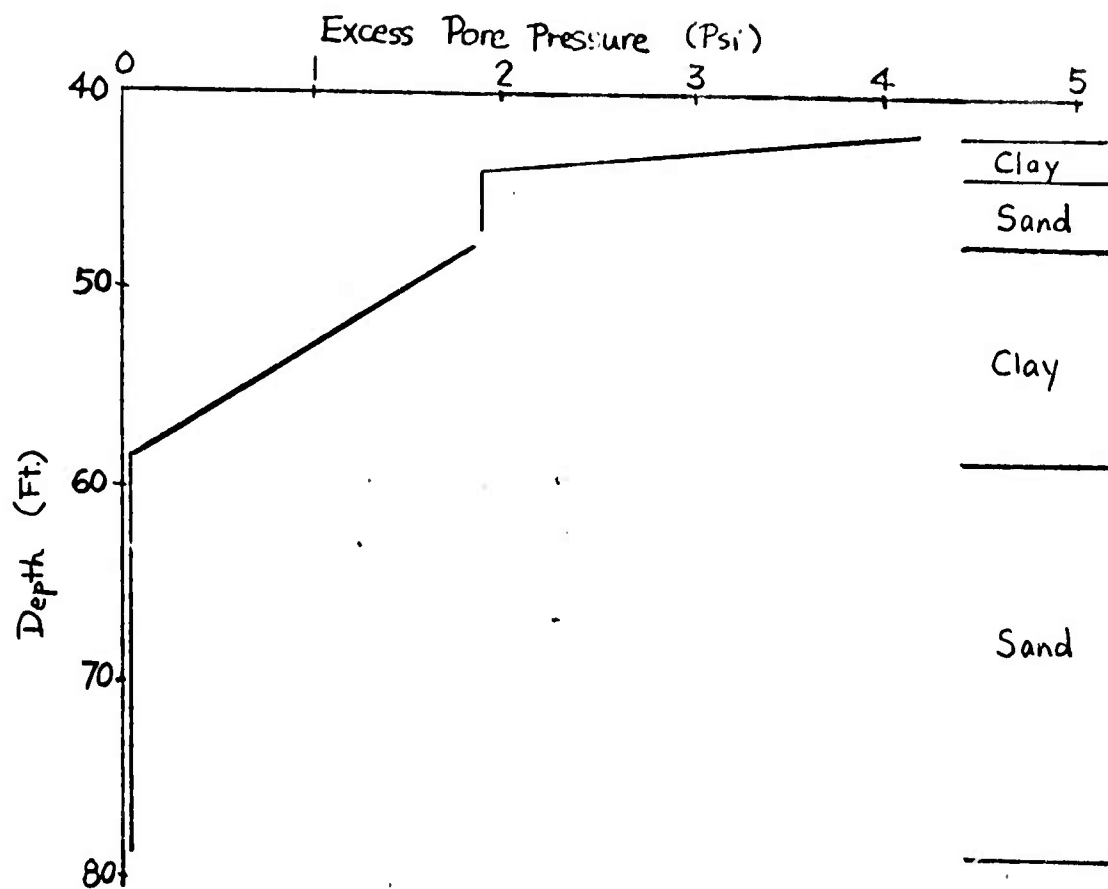
Fig. 51- Excess Pore Pressure, Left Boundary, Site No. 3
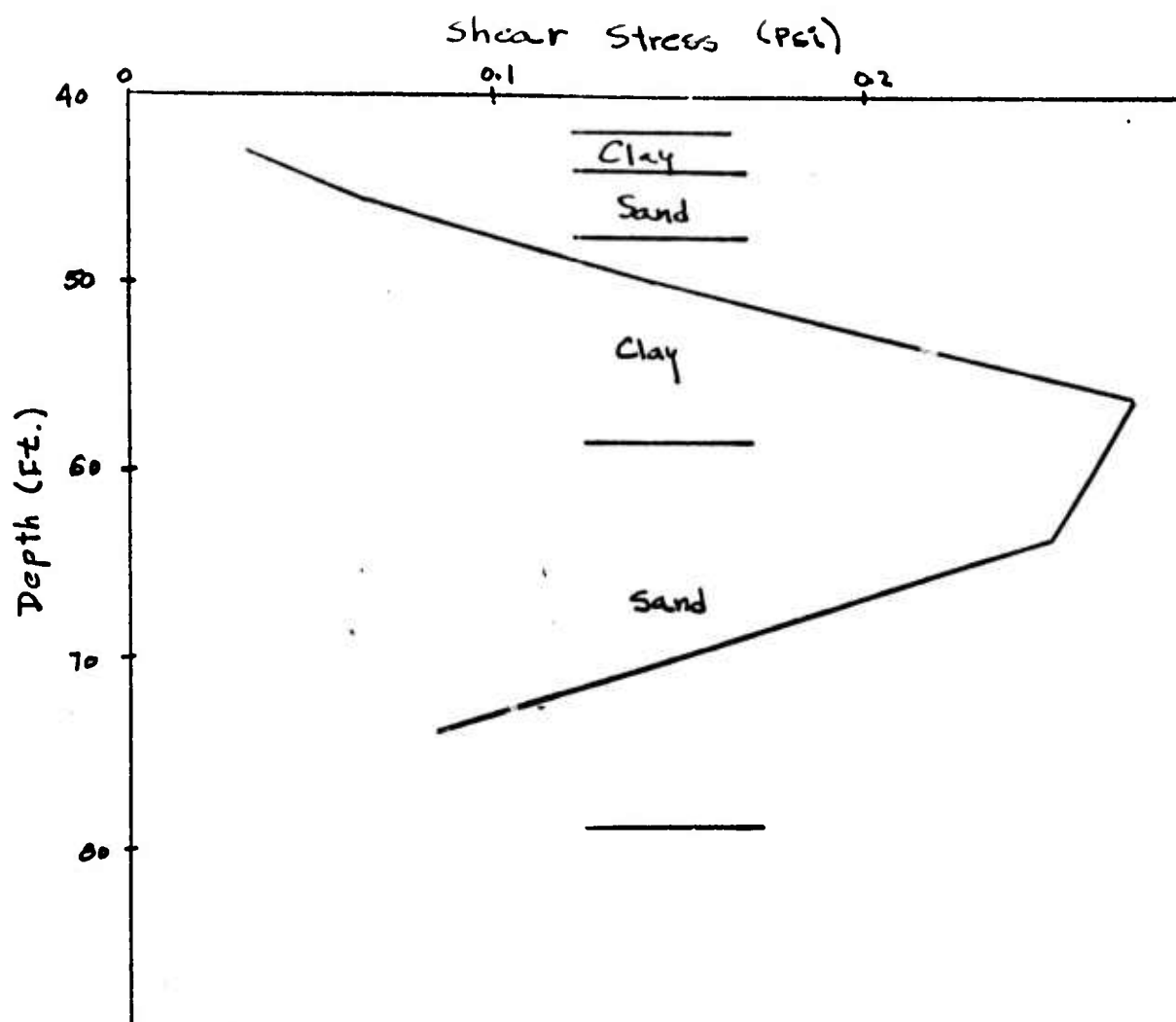
Fig. 52- Shear Stress Distribution, Right Boundary, Site No.3

Fig. 53- Radial Stress vs. Depth, Left Boundary, Site No. 3

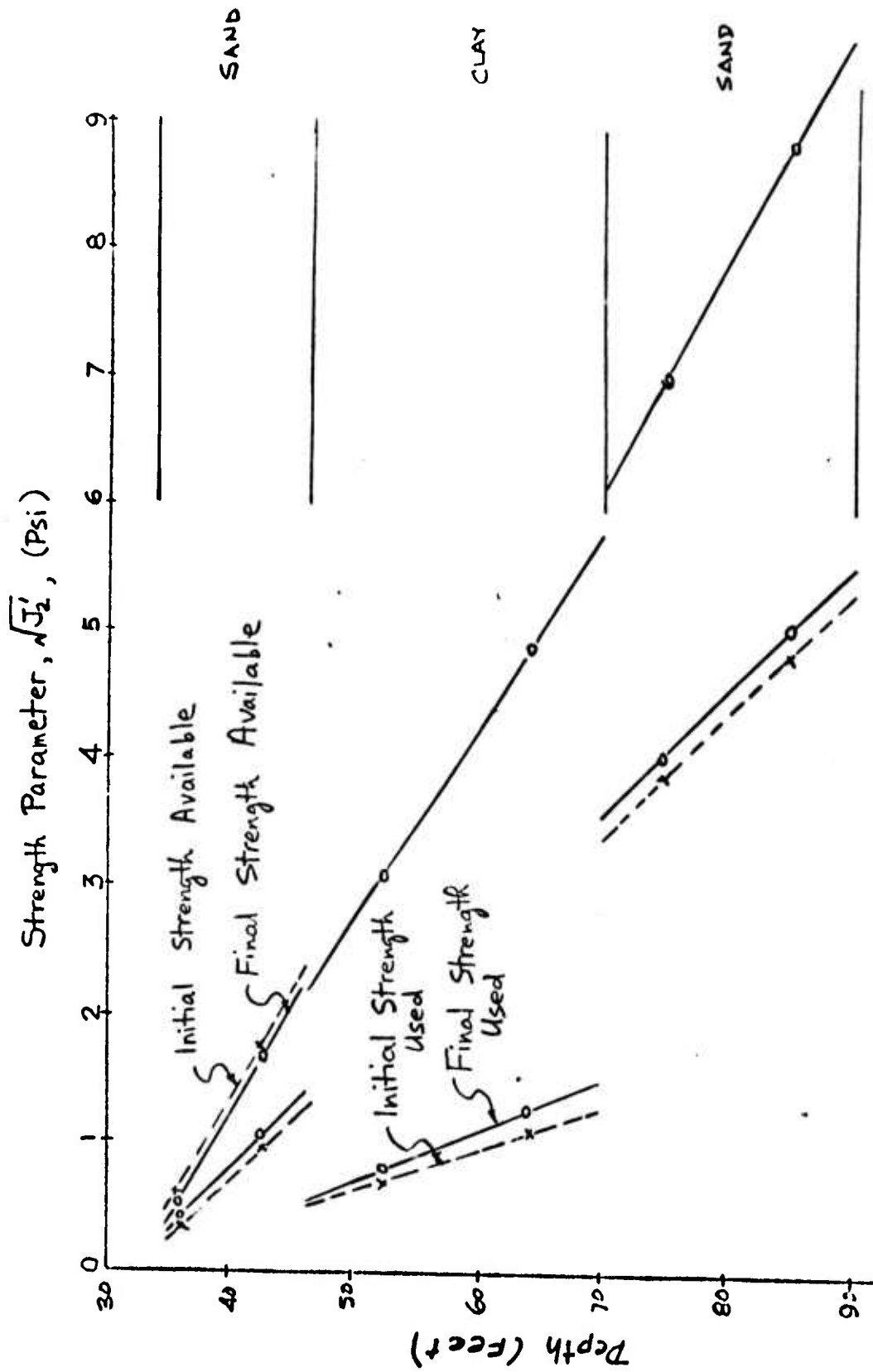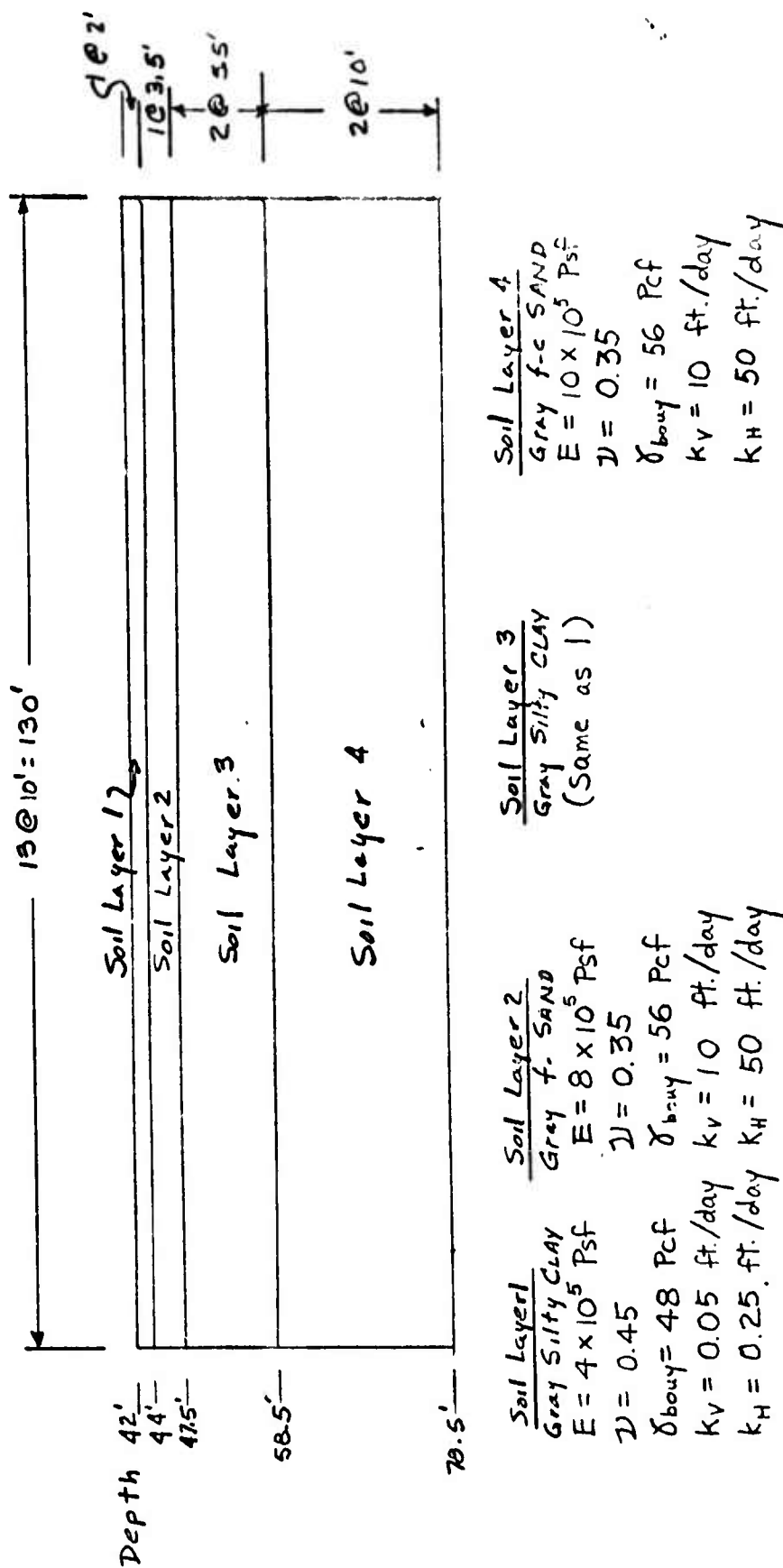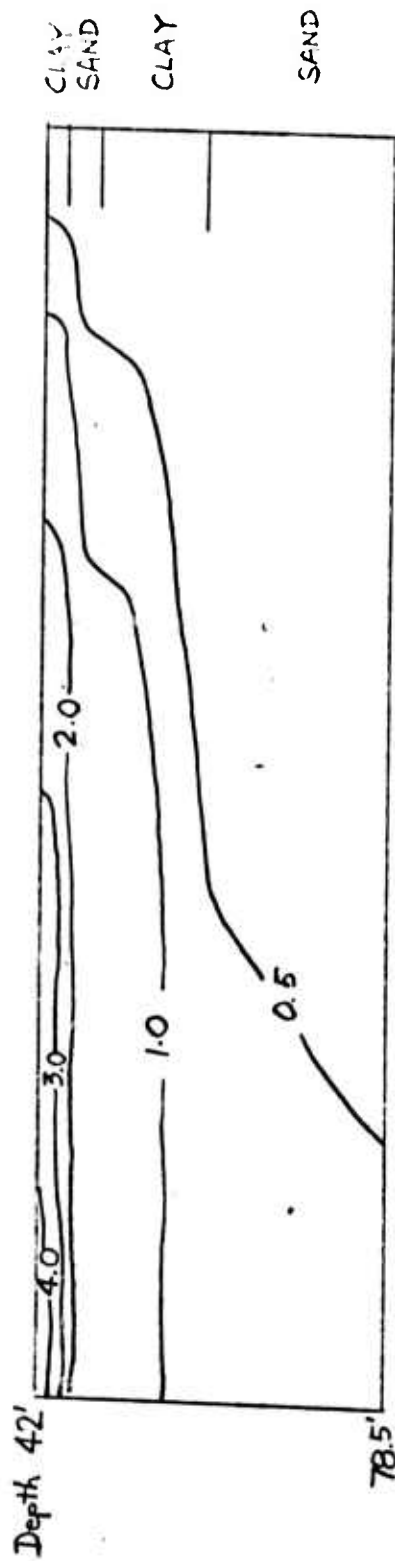Fig. 54- Strength Parameter, Right Boundary, Site No.3

FIG. 55   Influence of Sand/Clay Permeability Ratio on Safety Factor,
Left Boundary, Site No. 2 (k_{xx}/k_{yy} = 5 for all layers)

5.32

FIG. 56 Influence of Horizontal/Vertical Permeability Ratio on Safety Factor, Left Boundary, Site No. 2 ($k_{sand}/k_{clay} = .10$)

5.33

6.0 EMBANKMENT STABILITY TO OCEAN WAVES
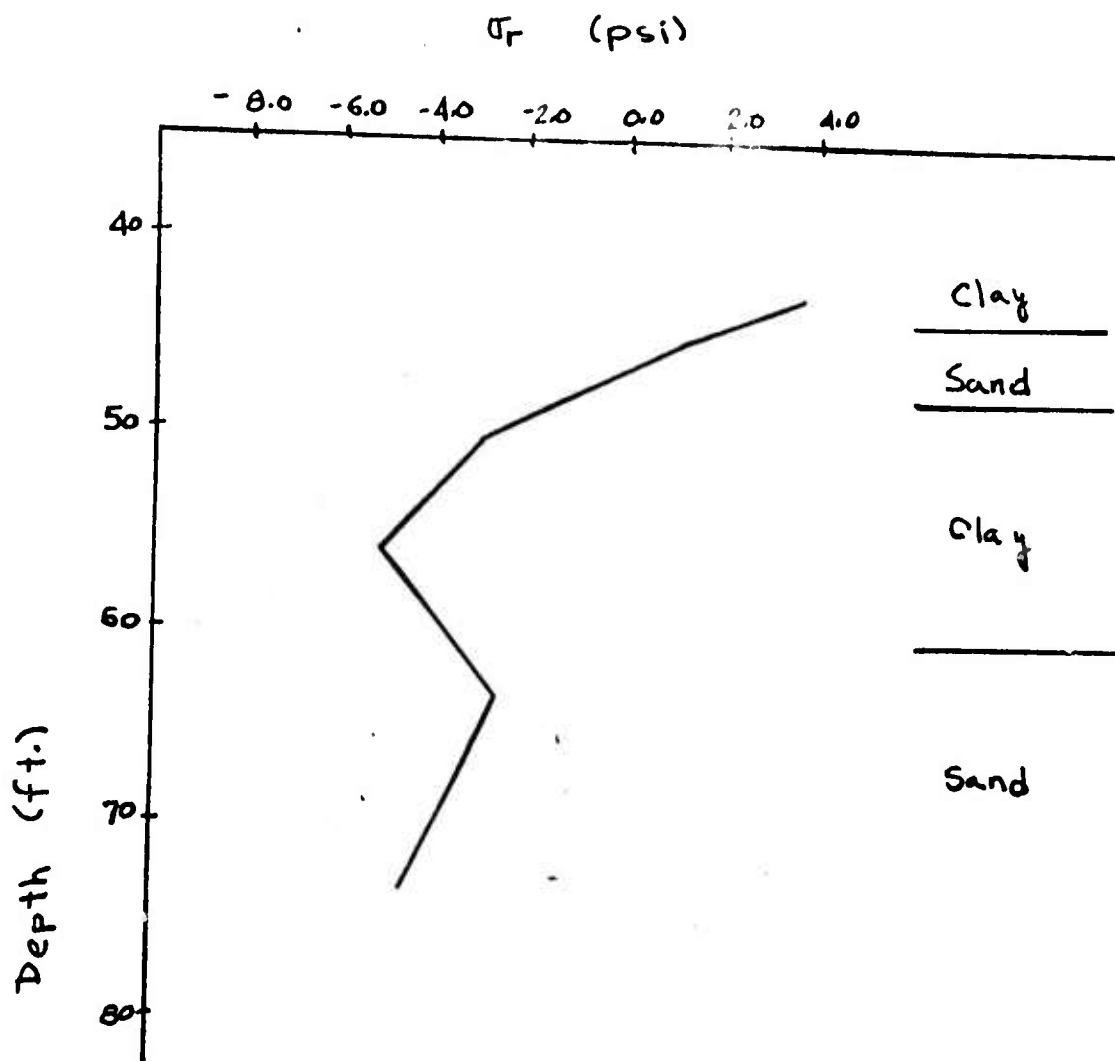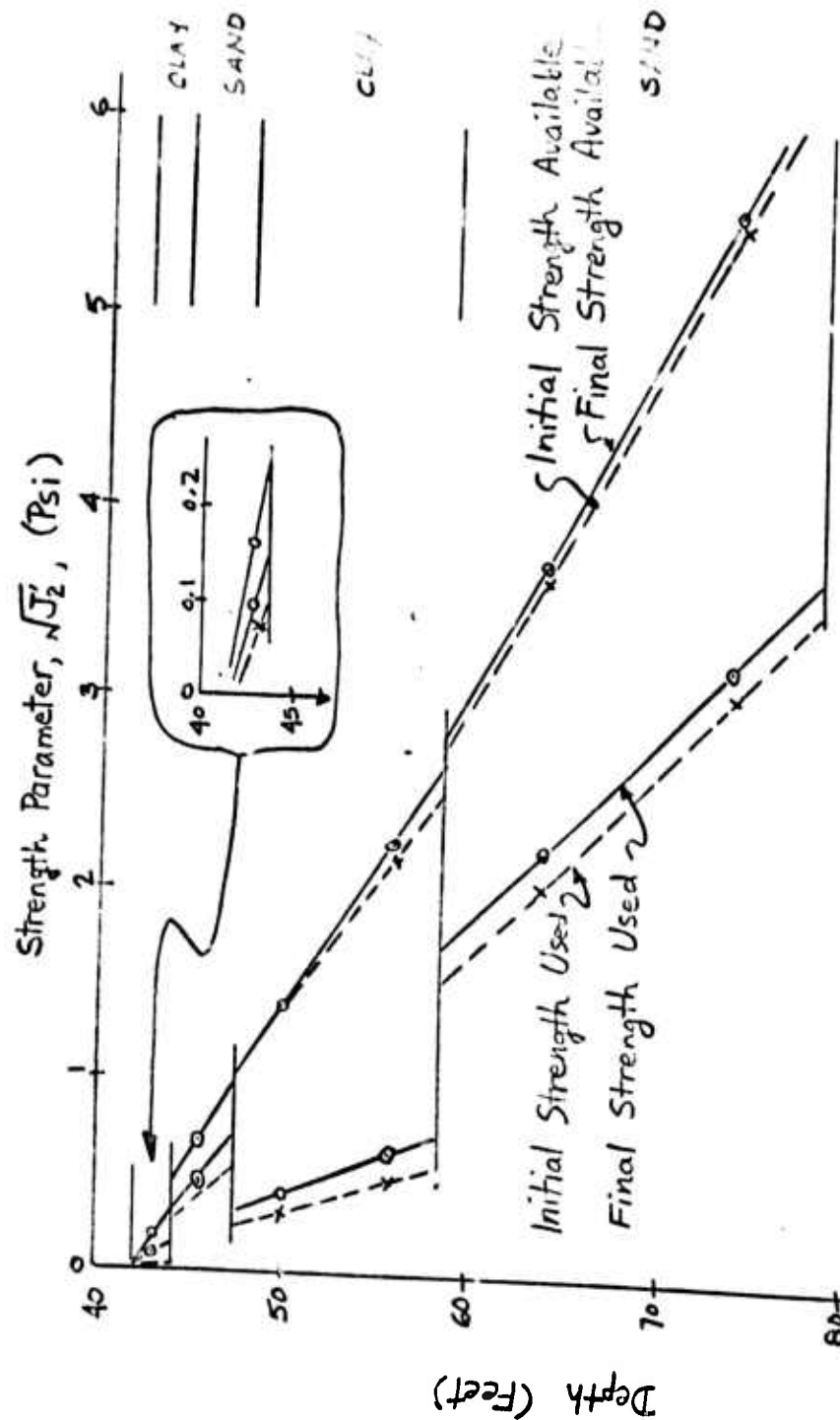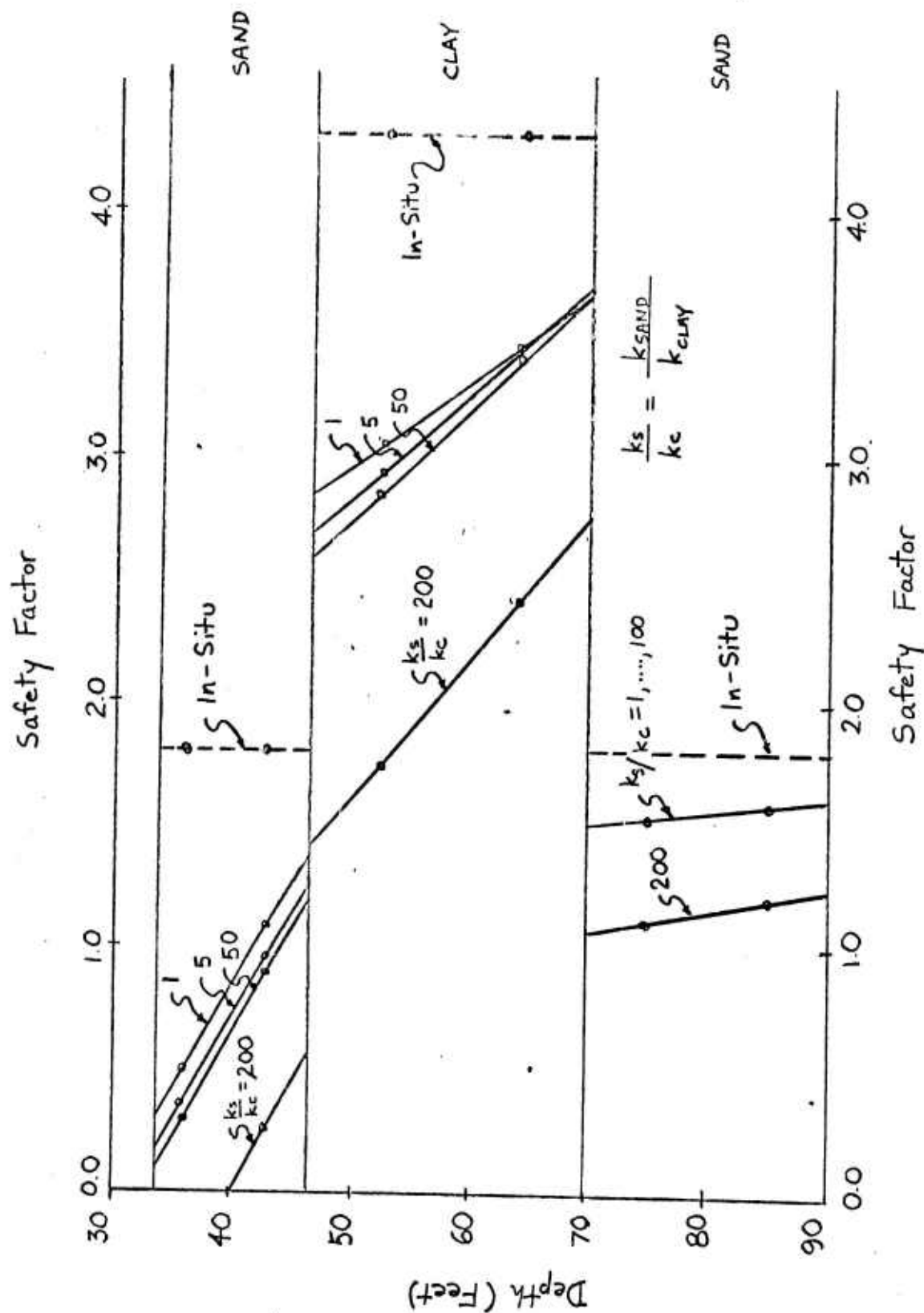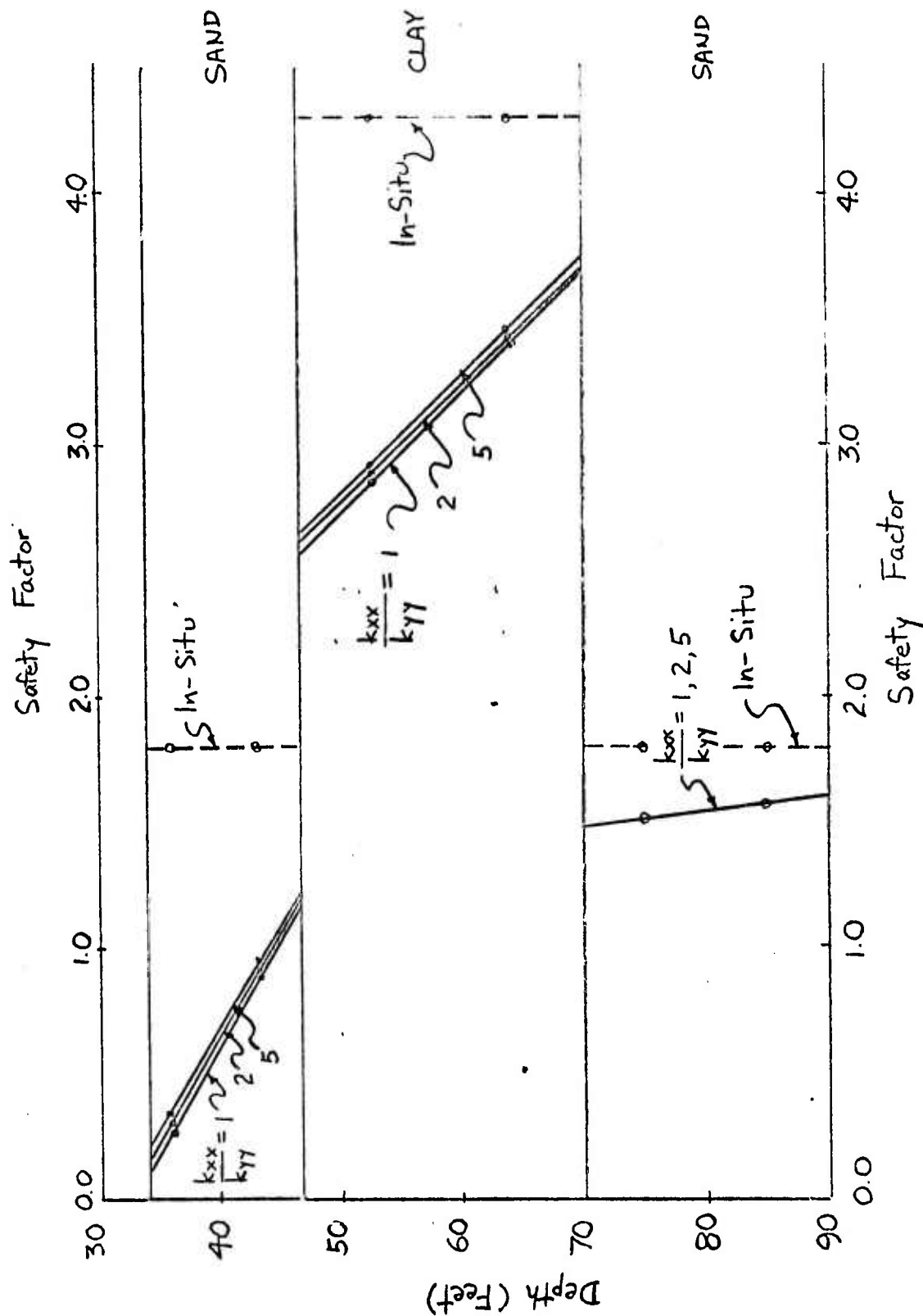
In t is section of the report, the stability analysis of an off-shore embankment is presented, this embankment being subjected to an ocean storm wave similar to that used in the previous problem. The profile of the embankment is shown in Figure 57 and consists of a concrete caisson protected on the seaward side by an embankment of coarse material varying from gravel to large "dolose" pieces on the external side. This embankment is placed atop a foundation similar to Site No. 2 of Section 5.0 and subjected to a large storm wave approaching from sea (right of Figure 57). The objective, of course, is to determine the adequacy of the embankment in protecting the caisson and landward zone within the embankment, by estimating the safety factor against a potential outward slide caused by the wave.

From Section 5.0, it was determined that the surface sand layer will liquefy under the crest of the wave, so that as the crest approaches the toe of the embankment, a potential slide may occur since the sand layer has little available shear strength to support the embankment. Since it was anticipated that a potential failure condition existed near the toe of the embankment and could spread inward into the center of the embankment, influencing overall stability, a complete nonlinear analysis of the embankment was conducted.

To perform the nonlinear analysis, the problem was conducted in two phases, the first being concerned with the dead load stresses developed by construction of the embankment, and the second phase being concerned with the stresses generated by

the storm wave. At all times in the analyses, total intergranu-
lar stresses were maintained to assess the nonlinear behavior of
the soil materials. The dead load solution, in addition, was
conducted in three stages, corresponding to the potential con-
struction loading schedule of the embankment. A portion of the
finite element mesh used for these analyses is shown in Figure 58.

6.1 Material Properties

For the various soil types of the problem, three dif-
ferent soil models were used in the analyses. For the embankment
materials (gravel, stone, dolose), a Coulomb-Mohr material law
was used as outlined in Section 3.3. For the foundation mate-
rials (sand and clay strata) nonlinear soil models were used
which produced stiffening under increasing confining pressures
and softening under increasing deviatoric stresses or shear load-
ings. These soil models are similar to the nonlinear models of
Section 3.4. In these cases, formulas based on experimental data
(Ref. 13) were generated for typical sand/clay materials, relat-
ing bulk and shear moduli for the soils to J_1, J_2' , initial void
ratio, etc. For the clay soil, a hyperbolic stress-strain model
was used.

6.2 Dead Load Analysis

The dead load analysis proceeds in the usual manner as
follows. A finite element mesh is superimposed on the zone of
interests, properties of each element specified by the (in gen-
eral) nonlinear stress strain relations of the materials and
suitable boundary conditions applied to the boundary modes. The

6.2

analysis then determines the solution to the following system of
equations.

$$\{F^A\} = [K]\{x\} - \{F^N\} \tag{47}$$

where $\{F^A\}$ is the vector of applied loadings. For this problem,
the applied loading is simply the dead loads caused by the mate-
rial weight. The vector $\{x\}$ is the vector of node displacements
(unknown) while the matrix $[K]$ is the effective stiffness matrix
of the finite element mesh determined from the initial moduli of
the materials. The vector $\{F^N\}$ are correction forces which ac-
count for the fact that the material stress-strain relations vary
with applied stresses and are nonlinear. To solve equations (47)
an iterative technique is used to generate the nonlinear correc-
tion forces with node displacement.

The zone of interest consists of six material zones and
the caisson. The caisson was simulated by including the finite
element mesh through the structure but using relatively high
stiffness properties to determine rigid body response. As can be
noted in Fig. 57, the material zone was considered to a depth of
130 feet below MLW, through the second relatively stiff founda-
tion sand material. For the static analyses, this zone cutoff
was considered adequate since the top sand and clay layer are
relatively soft and will cause the majority of the caisson set-
tlements. In addition, from the previous wave pore pressure so-
lution (Section 5.0), it was determined that wave pore pressure
effects will not extend past the foundation clay layer. Thus
this same zone definition should be adequate for the wave

liquefaction analysis.

The lateral extent of the zone of interest used in the analysis is larger than shown in Figure 58, and provided a foundation extent of about 200 feet on either side of the embankment cross-section. This extent was deemed adequate to allow any stability failures, if generated, from occurring. The boundary conditions on the lateral boundaries were specified as vertical roller supports while on the horizontal boundary they were specified as horizontal rollers.

The finite element mesh consists of both quadrilateral as well as triangular elements. For the foundation materials, single element thicknesses were provided through the top foundation sand and clay layers while two elements were used through the bottom foundation sand thickness. For this study, this fineness of the mesh was deemed adequate although the mesh through the clay zone should probably be improved in more refined analyses.

In order to determine settlement characteristics simulating actual constructive procedures, a four-stage analysis was considered. The first stage was concerned with determining the initial stress and strain state in the material overburden without the embankment. This was accomplished by using a zero unit weight for all the embankment zones. Once this solution was available, the following loadings were placed on the structure in the sequence that could be used during actual construction. During each of the four-stage analyses, a double iteration procedure was used to improve the accuracy of the results. Applied loadings during each stage were applied in three increments and

numerical interation (equation 47) was used during each load
increment.

The first construction stage loading considered the ap-
plication of the loads caused by the caisson plus a 15-foot thick
layer of the fill material as shown in Figure 59. The factors of
safety computed in each element are also shown in the figure.
The factor of safety is defined as shear strength available (due
to the hydrostatic compression stress) divided by the effective
shear stress applied. As may be noted from Figure 59, the fac-
tors of safety throughout the zone are adequate (greater than
1.0) except in the gravel material immediately below the caison.
This indicates that the properties assumed for this material are
too soft to adequately restrain the caisson. A factor of safety
of 1.0 indicates that the stress state is on the yield surface
and relatively large deformations are possible. Preliminary in-
vestigation indicated that the properties used in the analyses
are conservative and higher stiffness and strength properties
could be used. However, this also implies that the placement of
this material must be such as to ensure the adequacy of the
properties.

The second construction stage loading is shown in
Figure 60 and the results are similar to the above, namely that
the safety factors in the gravel are about 1.0. The final con-
struction stage loading is shown in Figure 61 together with all
the safety factors throughout the embankment. As may be noted,
the conservative property estimates for the gravel fill material
lead to low factors of safety throughout the zone.

The settlement profile of the caisson during each loading stage is shown in Figure 62. The results indicated that the "elastic" properties assumed for the caisson were adequate in that the caisson moved essentially as a rigid body. As can be seen, the settlements predicted for the caisson vary from 7.5 inches on the inside (left side of the mesh) to 14.6 inches on the side toward the embankment centerline. This large settlement is due primarily to the settlements caused by the shear flow indicated by the low safety factors in the gravel materials. Again, using stiffer values for this data will lead to correspondingly smaller caisson motions but placement conditions must be such so as to guarantee the availability of the properties.

6.3 Wave Liquefaction Analysis

Prior to starting the liquefaction analysis, several modifications were made to the intergranular soil properties of the embankment fill materials. The initial elastic moduli of these materials were increased by 50% while the friction angle for the quarry run material was increased from 40° to 45°. This was done since the safety factors in the gravel material were 1.0 (stress points on the yield surface) and initial liquefaction analyses indicated that the embankment could not withstand any significant wave motion. To properly include this effect, the dead load solution should be rerun, to obtain a consistant set of initial conditions for the liquefaction analysis. However, for this demonstration investigation, it was felt that this improvement was unnecessary.

For this embankment problem, pore pressure time

6.6

histories were specified along the top of the foundation sand since it was felt that the permeability effects through the coarse embankment materials were sufficiently nonlinear as to preclude a realistic analysis based upon D'arcy's law. Thus seepage flow assumed to occur within the foundation soils only and not through the embankment materials. Excess pore-pressure histories were specified at the locations shown in Figure 57. These pressures were specified by essentially taking the storm wave pressures and scaling them linearly with distance into the embankment and adding a small time lag to phase the pressures. It is clear that to properly analyze this problem, experimental data would be required to ascertain a complete set of pore pressure boundary conditions.

The problem was started with the wave applied upstream of the embankment (right side of the mesh) and moved into the embankment in relatively small time steps. The numerical results shown are referenced to time zero occurring when the wave crest is approximately above the toe of the embankment. Figures 63 through 70 indicate the factors of safety computed in each element as the wave progresses into the embankment. Numerical stability problems appear to begin when the negative pore pressures are generated on the right side of the mesh (above the toe). The displacements computed indicate the clay layer under the embankment moving down and to the right with the material to the right of the toe moving upward, causing a general decrease in the factors of safety in the embankment materials. Further computation tends to exaggerate these results leading to an eventual collapse of the embankment. Thus the calculations

6.7

indicate an erosion of the foundation material strengths under the toe of the embankment. This is caused by the seepage pressures generated from the water flow moving from under the embankment (positive pore pressures).

RANGE (FEET)

ZONE
1   Top Foundation Sand
2   Foundation Clay
3   Bottom Foundation Sand
4   Gravel
5   Stone
6   Dolose
7   Caisson

⊗ Location at which Pore
   Pressure are specified
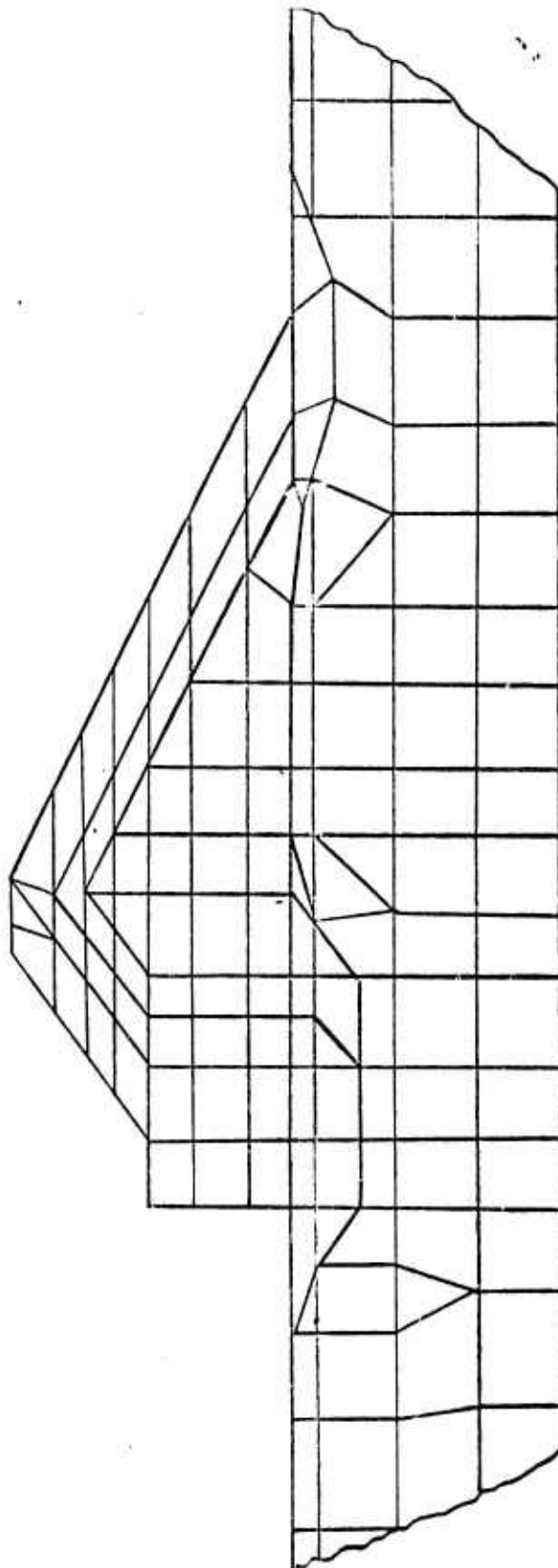
MLW

DEPTH (FT)

FIG. 57   Material Zone Description

6.9

FIG. 58 Part of Finite Element Mesh
Through Embankment
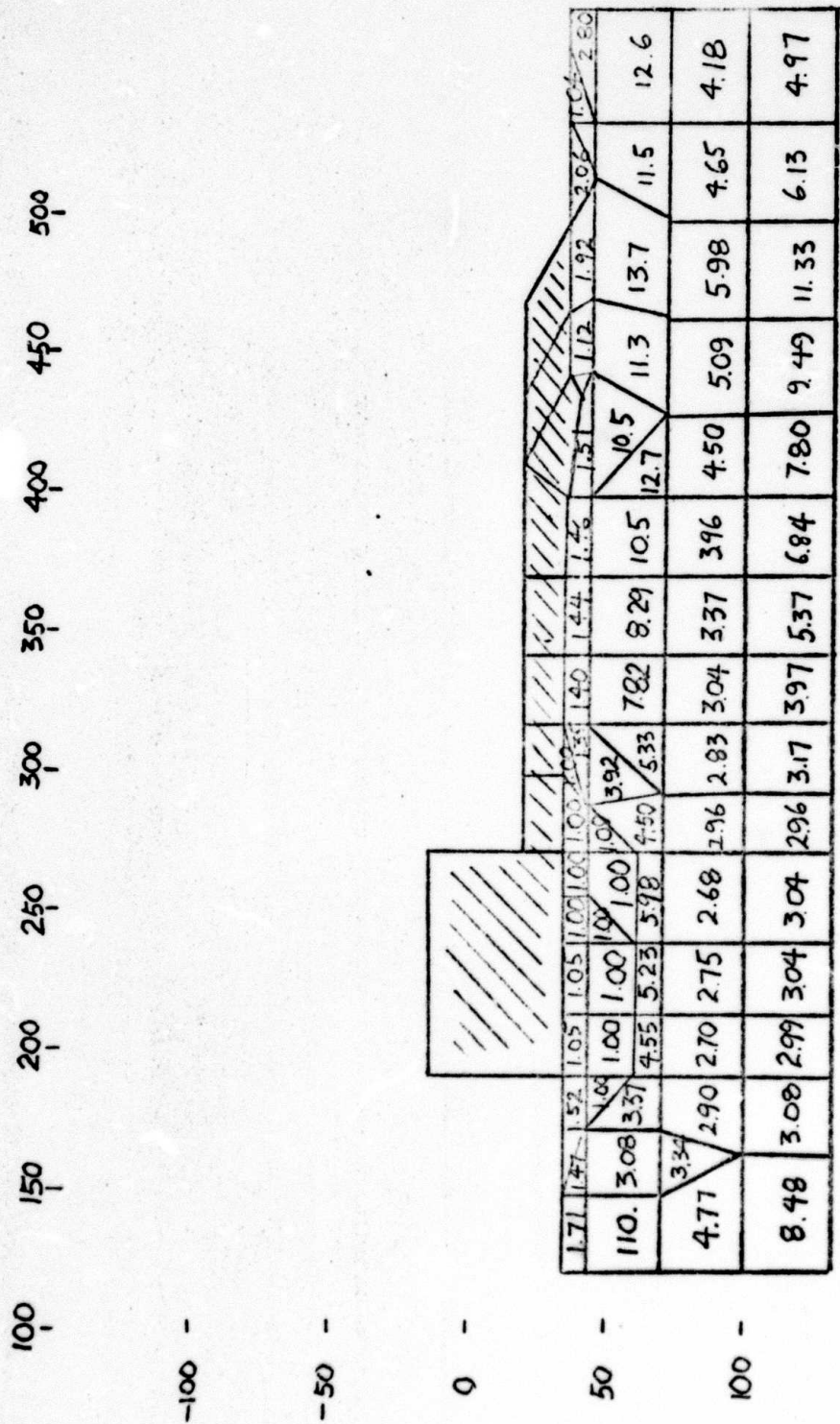
FIG. 59   Safety Factor Profile, Stage 1 Loading

6.11
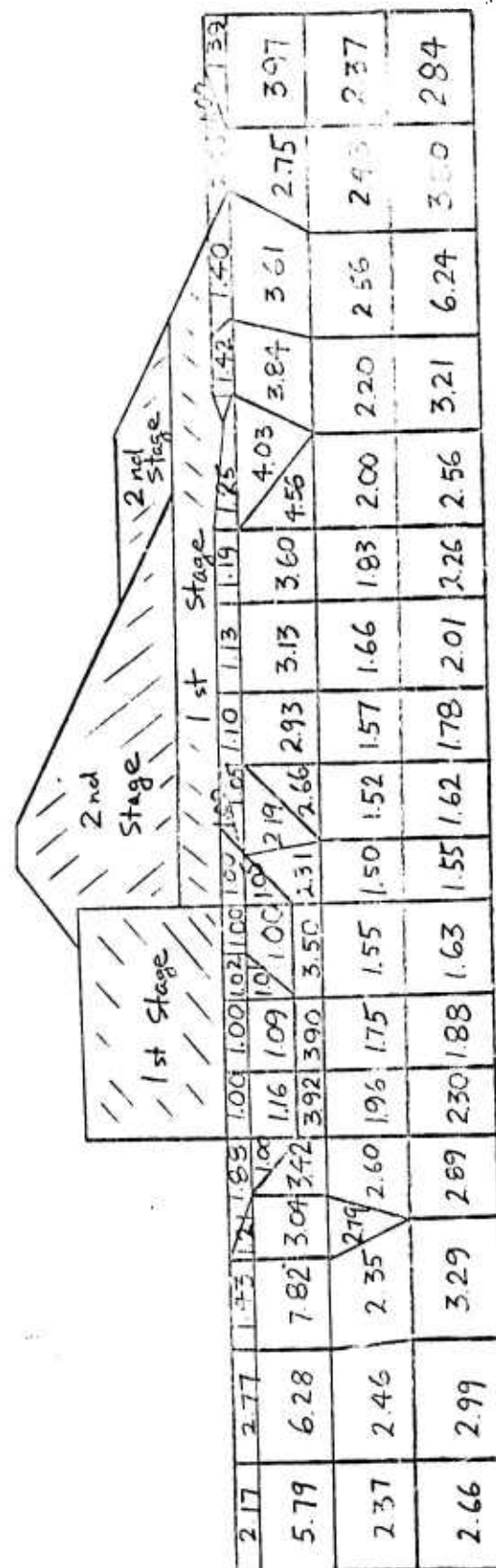
FIG. 60 Safety Factor Profile, Stage 2 Loading
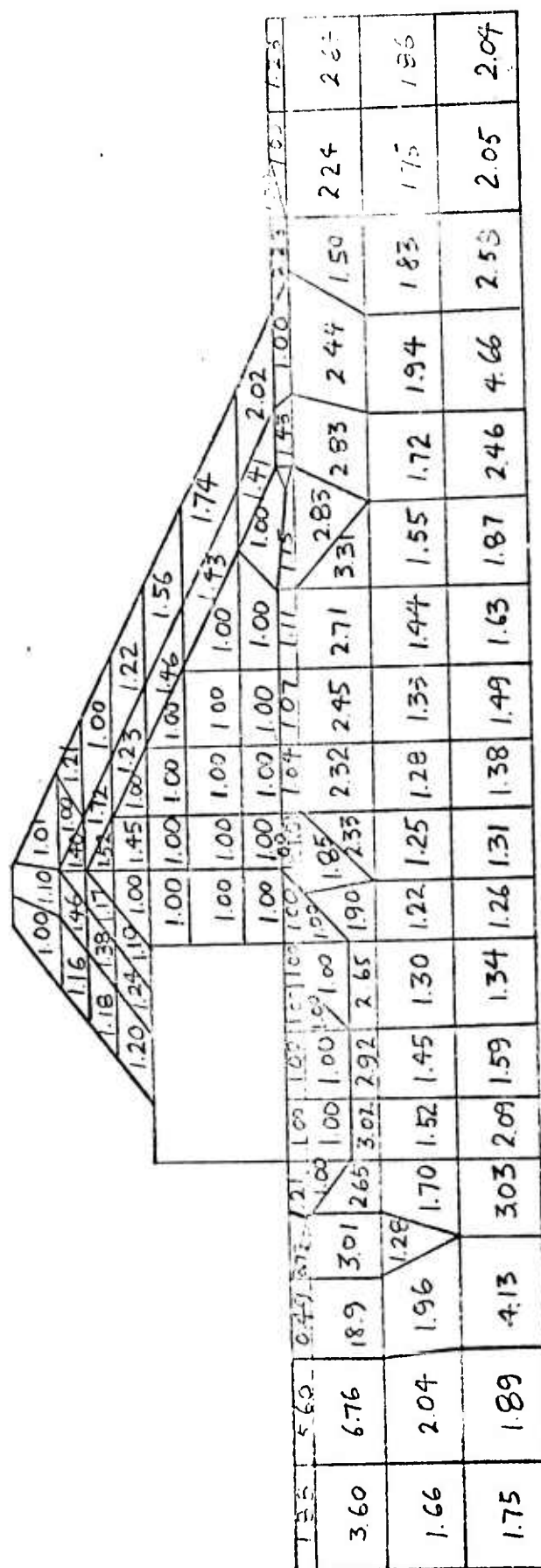
FIG: 61 Safety Factor Profile, Final Stage
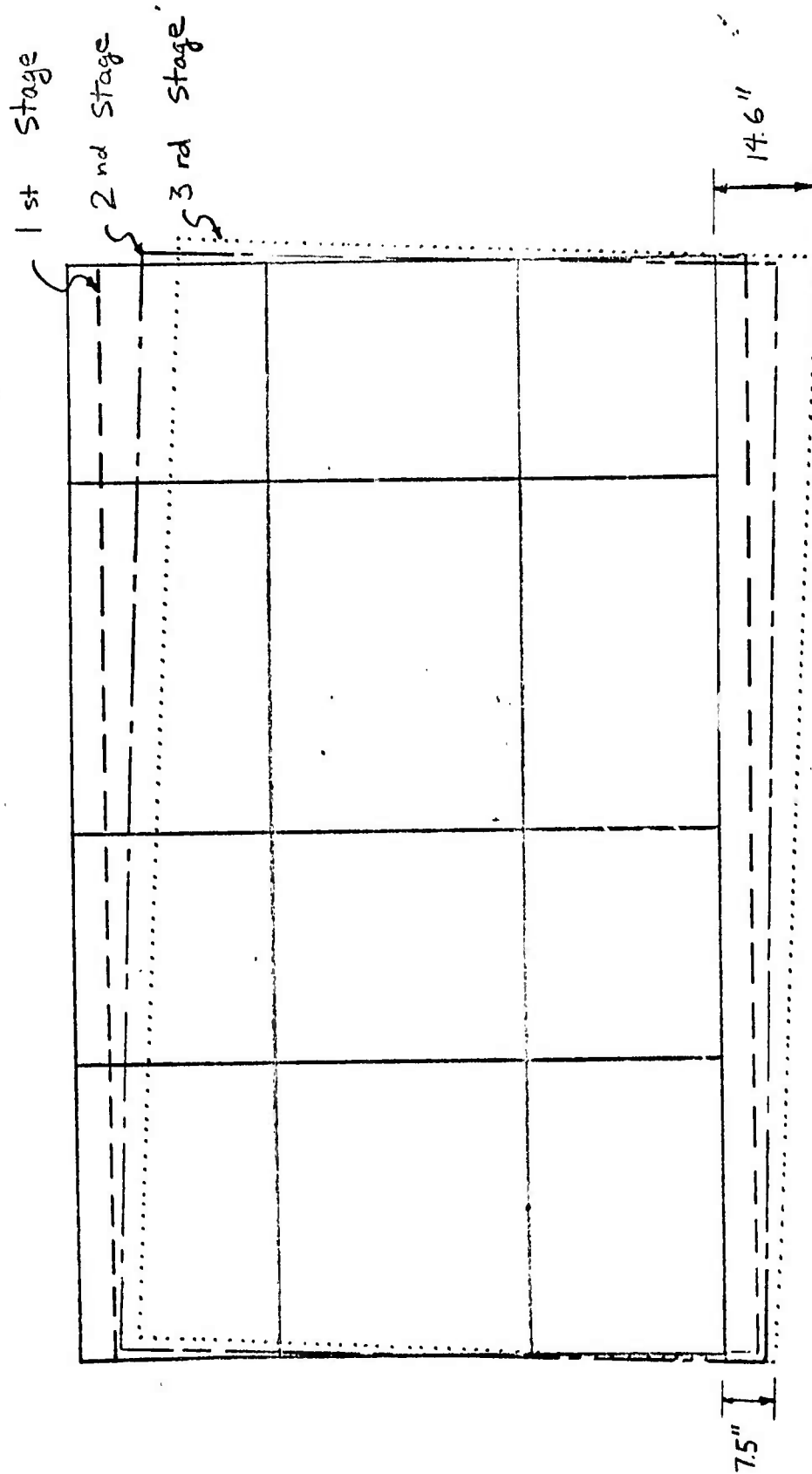
FIG. 62 Caisson Settlements During Stage Construction

1st Stage

2nd Stage

3rd Stage

14.6"

7.5"

FIG. 63 Factor of Safety Profile at 1 sec.

Pore Press.
(Psi above MLW)

+10

0

-10

+

T = 1 Sec.

FIG. 64 Factor of Safety Profile at 2 sec.

Pore Press.
(Psi above MLW)

+10
0
-10

6-16

T= 2 sec

Pore Press. (Psi above MLW)

+10

0

-10

FIG. 65 Factor of Safety Profile at 3 sec.

6.17

T = 3 sec

Pore Press.
(Psi above MLW)

+10

0

-10

FIG. 66. Factor of Safety Profile at 4 sec.

Pore Press.
(Psi above MLW)

+10
0
-10

FIG. 67 Factor of Safety Profile at 5 sec.

6.19

FIG. 68 Factor of Safety Profile at 6 sec.

Pore Press.
(Psi above MLW)

+10
0
-10

FIG. 69 Factor of Safety Profile at 8 sec.

Pore Press.
(Psi above MLW)

+10

0

-10

T = 8 sec

Pore Press.
(Psi above
MLW)

+10

0

-10
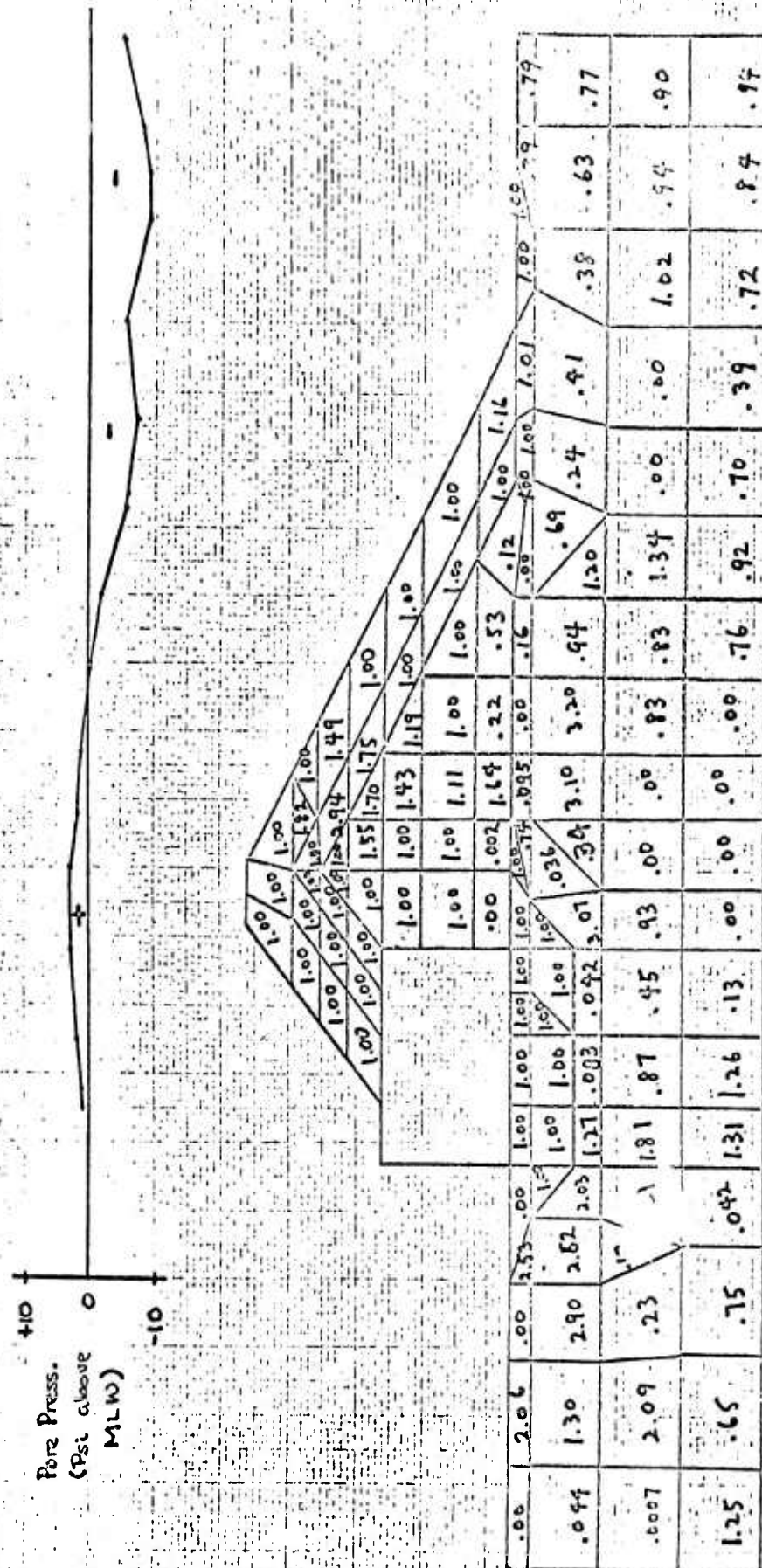
FIG. 70. Factor of Safety, Profile 12 sec.

T = 12 sec.

6-22

7.0 SUMMARY

This report has presented the results of a study to include the effects of pore water on the response of soils to transient loadings. Numerical results have been presented for problems which fall into different categories, in an attempt to span the problem areas of general interest. The first set of problems was concerned with computation of soil response to loadings in configurations which would be encountered in the laboratory, namely, triaxial and uniaxial configurations.

The second set of problems was concerned with the impact of entrapped pore fluid on wave propagation velocities. As goes without saying, the wave motion is completely governed by the boundary conditions since the fluid has been assumed incompressible. For the problem conditions assumed, the wave speeds in the soil are much smaller than the actual wave speeds in water, so that the incompressible assumption for the water appears reasonable. For the case where soil wave speeds approach that of the entrapped fluid, this assumption becomes questionable and at least fluid compressibility must be included in the analysis.

The last two problem sets have to do with a study of submerged, off-shore soils to transient ocean storm waves, a problem area receiving more and more consideration as off-shore construction increases (platforms, nuclear reactor stations, protective dikes, etc.). The approaches used appear to offer an attractive solution technique to this important class of problems.

One aspect of the numerical computation problem which has not been discussed in this report concerns the stability of

the computations. It is quite clear that such considerations were made during the course of the study to arrive at an acceptable computation, but no formal study of the problem was conducted during this project. The stability considerations have to do with the types of problems which may be studied as well as the time step required for the transient analyses to achieve a successful integration procedure. Some information has appeared in the literature concerning the first problem (Refs. 9 and 10) while no information on the second has been seen. Thus approximate rules of thumb have been devised for specific problem types but are not general enough as yet to be considered adequate.

8.0 REFERENCES

1. C. J. Costantino, "Stress Wave Propagation Through Earth-Water Systems" Interim Report No. 70-409-1, The City College Research Foundation for Advanced Research Projects Agency, Contract No. DAHC 19-69-C-0032, March, 1970.

2. D. W. Taylor, "Fundamentals of Soil Mechanics," John Wiley and Sons, Inc., 1948.

3. D. C. Drucker, W. Prager, "Soil Mechanics and Plastic Analysis or Limit Design," Quarterly of Applied Mathematics, vol. 10, 1952.

4. I. Nelson, "Investigation of Ground Shock Effects in Nonlinear Hysteratic Media; Report No. 2, Modeling The Behavior of a Real Soil," U. S. Army Waterways Experiment Station, Report No. S-68-1, July, 1970.

5. C. J. Costantino, "Two-Dimensional Wave Propagation Through Nonlinear Media," Journal of Computational Physics, August, 1969.

6. C. J. Costantino, "Finite Element Approach to Stress Wave Problems," Journal, Engineering Mechanics Division, ASCE, April, 1967.

7. C. J. Costantino, "Stress Waves in Layered Arbitrary Materials," Air Force Space and Missile Systems Organization Report No. SAMSO TR-68-225, September, 1968.

8. O. C. Zienkiewicz, "The Finite Element Method in Engineering Science," McGraw-Hill Book Co., 1971.

9. Y. Yokoo, et al, "Finite Element Method Applied to Biot's Consolidation Theory," Japanese Society of Soil Mechanics and Foundation Engineering, vol. 11, No. 1, March, 1971.

10. Y. Yokoo, et al, "Finite Element Analysis of Consolidation Following Undrained Deformation," Japanese Society of Soil Mechanics and Foundation Engineering, vol. 11, No. 4, December, 1971.

11. D. J. Henkel, "The Role of Waves in Causing Submarine Landslides," Geotechnique, vol. 20, No. 1, pp. 75-80, 1970.

12. R. L. Wiegel, "Oceanographical Engineering," Prentice-Hall, 1964.

13. A. S. Vesic, G. W. Clough, "Behavior of Granular Materials Under High Pressures," Journal, SMFD, ASCE, vol. 94, SM 3, May, 1968.

APPENDIX A

FORMULATION OF SYSTEM EQUATIONS

In the following presentation, the analysis will be carried forth for a typical element of the free-field mesh. The displacement field for the element is assumed to be linear and the displacement of any point within the element can be written as

$$u(r,z) = \{g\}'\{\alpha\}$$

$$w(r,z) = \{g\}'\{\beta\} \tag{A.1}$$

where (u,w) are the horizontal and vertical displacement components and $\{\alpha\}$, $\{\beta\}$ are each a set of arbitrary coefficients, with the number of coefficients equal to the number of element vertices to provide the proper number of degrees of freedom for the element.

The vector $\{g\}$ is formed by a proper set of element functions and depend upon the element type being considered. For a typical triangular element (Fig. A.1) this vector is

$$\{g\} = \{1, r, z\} \tag{A.2}$$

while for a typical rectangular element (Fig. A.2)

$$\{g\} = \{1, r, z, rz\} \tag{A.3}$$

For a general **quadrilateral** element (Fig. A.3) the vector $\{g\}$ specified by equation A.3 is used in the transformed coordinate system. By substituting the coordinates of the nodes into equation A.1, the coefficients $\{\alpha\}$, $\{\beta\}$ can be replaced as unknowns by the node point displacement components, or

$$u(r,z) = \{g\}'[D]\{u\}$$
$$w(r,z) = \{g\}'[D]\{w\}$$

(A.4)

This simple displacement function assumed for the element allows for determining any interior displacement in terms of the nodal displacements and ensures that the displacements between any two adjacent elements will be continuous for any arbitrary specification of nodal displacements. Higher order element formulations are also available to satisfy the above criteria.

The strains developed at any point within the element can be determined from the strain displacement relations for the particular configuration, or

$$\{\epsilon^T\} = [B_u]\{u\} + [B_w]\{w\}$$

(A.5)

where $\{\epsilon^T\}$ is the strain vector with components

$$\{\epsilon^T\} = \{\epsilon_r^T, \epsilon_\theta^T, \epsilon_z^T, \gamma_{rz}^T\}$$

(A.6)

The superscript T in equation A.6 indicates total strains.

A.3

For the combined stress/pore pressure problem, the intergranular stress are related to the pore pressure by

$$\{\sigma\} = \{\bar{\sigma}\} - \pi\{I\} \tag{A.7}$$

where $\{\sigma\}$ are the total stress in the body defined by

$$\{\sigma\} = \{\sigma_r, \sigma_\theta, \sigma_z, \tau_{rz}\} \tag{A.8}$$

$\{\bar{\sigma}\}$ are the effective or intergranular stresses and π is the pore pressure. The vector $\{I\}$ is defined as $\{1, 1, 1, 0\}$. The effective stresses are related to the strains through the general stress strain relations

$$\{\bar{\sigma}\} = [C]\{\epsilon^T - \epsilon^N\} \tag{A.9}$$

where $\{\epsilon^N\}$ are defined as the nonlinear components of the total strain and $[C]$ is the usual elastic stress strain matrix which, for example, can be defined for the axisymmetric problem by

$$[C] = \bar{E} \begin{bmatrix} 1-\nu & \nu & \nu & 0 \\ \nu & 1-\nu & \nu & 0 \\ \nu & \nu & 1-\nu & 0 \\ 0 & 0 & 0 & \left(\frac{1-2\nu}{2}\right) \end{bmatrix} \tag{A.10}$$

and $\bar{E} = E/(1+\nu)(1-2\nu)$

where E is Young's modulus and ν is Poisson's ratio. For relatively simple material models (such as The Mises or Coulomb-Mohr plastic models), the nonlinear strains represent the nonrecoverable or plastic strain components. For more complicated material models, the vector $\{\epsilon^N\}$ represents a fictitious set of strains required to yield the proper stresses.

To satisfy equilibrium conditions at the element nodes with the total stress field within the element, the usual virtual work principal is used. The internal work performed by the stresses on a virtual total strain field is defined by

$$\delta W_i = \int_V \{\delta\epsilon^T\}'\{\sigma\}\, dV \tag{A.11}$$

where the integral is taken over the element volume. The corresponding external work performed by forces applied at the nodes is

$$\delta W_e = \{\delta u\}'\{R_u\} + \{\delta w\}'\{R_w\} \tag{A.12}$$

where $\{R_u\}$ are the horizontal force components at each node and $\{R_w\}$ are the corresponding vertical force components. Equating the internal and external work expressions and making us of the definitions previously described, the force components that must be applied at each node point to maintain equilibrium with the total stress within an element are

$$\{R_u\} = [k_{uu}]\{u\} + [k_{uw}]\{w\} - \{R_u^N\} - \{R_u^P\}$$

$$\{R_w\} = [k_{wu}]\{u\} + [k_{ww}]\{w\} - \{R_w^N\} - \{R_w^P\}$$

(A.13)

The matrices $[k_{uu}]$, $[k_{uw}]$, etc. are the usual elastic stiffness matrices and are defined by

$$[k_{ij}] = \int_V [B_i]'[c][B_j] \, dV$$

(A.14)

where the subscripts (i,j) take on the values of (u,w). The terms $\{R_u^N\}$, $\{R_w^N\}$ represent the correction forces to account for material nonlinearity and are defined by

$$\{R_i^N\} = \int_V [B_i]'[c]\{\epsilon^N\} \, dV$$

(A.15)

where again the subscript (i) takes on the values (u,w). The terms $\{R_u^P\}$, $\{R_w^P\}$ represent the effects of pore pressure on the equilibrium equations and are defined by

$$\{R_i^P\} = \int_V \pi [B_i]'\{I\} \, dV$$

(A.16)

In the computer program developed, the pore pressure variation is assumed to be a linear one over the element or

$$\pi(r,z) = \{g\}'[D]\{\pi\}$$

(A.17)

where the vector $\{\pi\}$ represents the nodal point pore pressures. Substituting equation A.17 into A.16 then yields

$$\{R_i^p\} \cdot [\overline{k_i}]\{\pi\} \qquad \text{(A.18)}$$

where

$$[\overline{k_i}] \cdot \int_v [B_i]'\{I\}\{g\}'[D]\,dV \qquad \text{(A.19)}$$

where the subscript i represents both the u and w directions.

To relate the pore presusres to the node point displacements (or velocities), seepage effects are considered. The seepage equations are obtained by minimizing the functional (Ref. 8).

$$\Omega = \int_v \left\{ \tfrac{1}{2}\left[k_{rr}\left(\frac{\partial \pi}{\partial r}\right)^2 + 2k_{r_3}\left(\frac{\partial \pi}{\partial r}\right)\left(\frac{\partial \pi}{\partial_3}\right) + k_{33}\left(\frac{\partial \pi}{\partial_3}\right)^2 \right] - \pi Q \right\} dV \qquad \text{(A.20)}$$

The permeability components k_{rr}, k_{r_3}, k_{33} are related to the principal permeability coefficients by

$$k_{rr} = k_1 \sin^2\theta + k_2 \cos^2\theta$$

$$k_{r_3} = \sin\theta \cos\theta\,(k_2 - k_1) \qquad \text{(A.21)}$$

$$k_{33} = k_1 \cos^2\theta + k_2 \sin^2\theta$$

where (k_1, k_2) are the principal coefficients in two orthogonal directions and θ is the angle from the $_3$-direction to the r-direction positive in the clockwise sense.

For a particular element, the variation of pore pressure over the element is assumed to be linear or

$$\pi(r,z) = \{g\}'[D]\{\pi\} \qquad\qquad (A.22)$$

Substituting equation A.22 into A.20, the functional can be written as

$$\Omega = \tfrac{1}{2}\{\pi\}'[D][S][D]\{\pi\} - \{\pi\}'[D]'\{J\} \qquad\qquad (A.23)$$

where the matrix $[S]$ is defined by

$$S_{ij} = \int_v \left\{ k_{rr}\frac{\partial g_i}{\partial r}\frac{\partial g_j}{\partial r} + 2k_{rz}\frac{\partial g_i}{\partial r}\frac{\partial g_j}{\partial z} + k_{zz}\frac{\partial g_i}{\partial z}\frac{\partial g_j}{\partial z} \right\} dV \qquad\qquad (A.24)$$

The vector $\{J\}$ is defined as the volume integrals

$$\{J\} = \int_v Q\{g\}\, dV \qquad\qquad (A.25)$$

where Q is the volume decrease per unit volume per unit time.

The solution to the seepage problem is obtained by minimizing the function Ω with respect to the nodal pressures leading to the conservation equation

$$[D]'[S][D]\{\pi\} = [D]'\{J\} \qquad\qquad (A.26)$$

or to further condense notation

$$[H]\{\pi\} = [D]'\{J\} \qquad\qquad (A.27)$$

The vector $\{J\}$ can be evaluated by considering the volume compression of the solids plus that of the water, or

$$Q = -\{\dot{\epsilon}^T\}'\{I\} + \frac{1}{E_v}\pi \tag{A.28}$$

where E_v is the effective bulk modulus of water and the vector $\{\dot{\epsilon}^T\}$ is the total strain rate vector. The strain rates are related to the nodal velocities by

$$\{\dot{\epsilon}^T\} = [B_u]\{\dot{u}\} + \lfloor B_w \rfloor\{\dot{w}\} \tag{A.29}$$

Substituting the above into the conservation equation leads to

$$[H]\{\pi\} = -[\bar{k}_u]'\{\dot{u}\} - [\bar{k}_w]'\{\dot{w}\} + [H^*]\{\pi\} \tag{A.30}$$

where
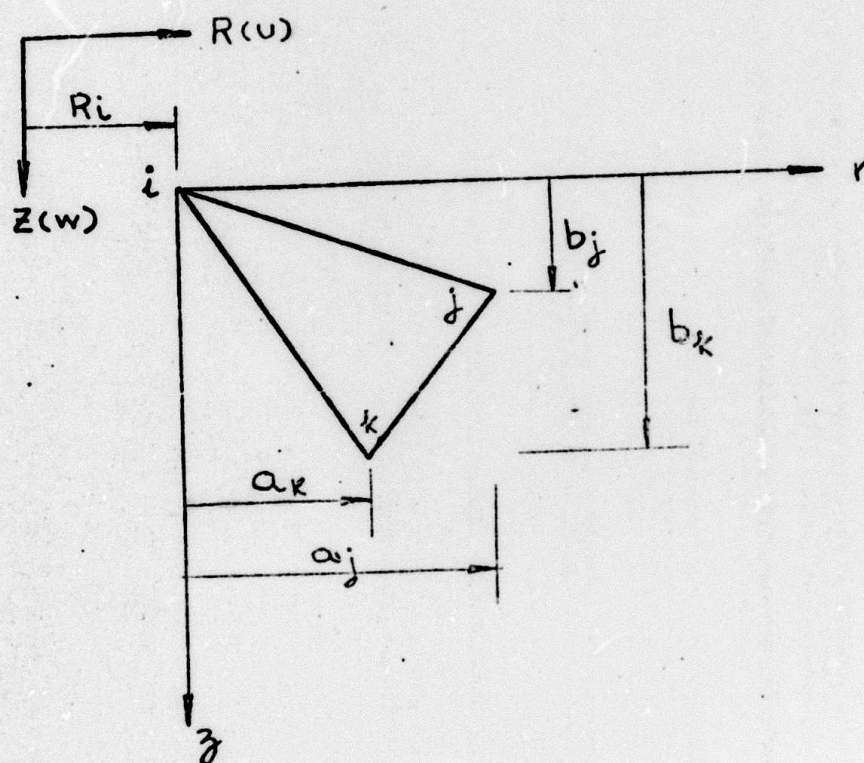
$$[H^*] = [D]'[T][D]$$

and

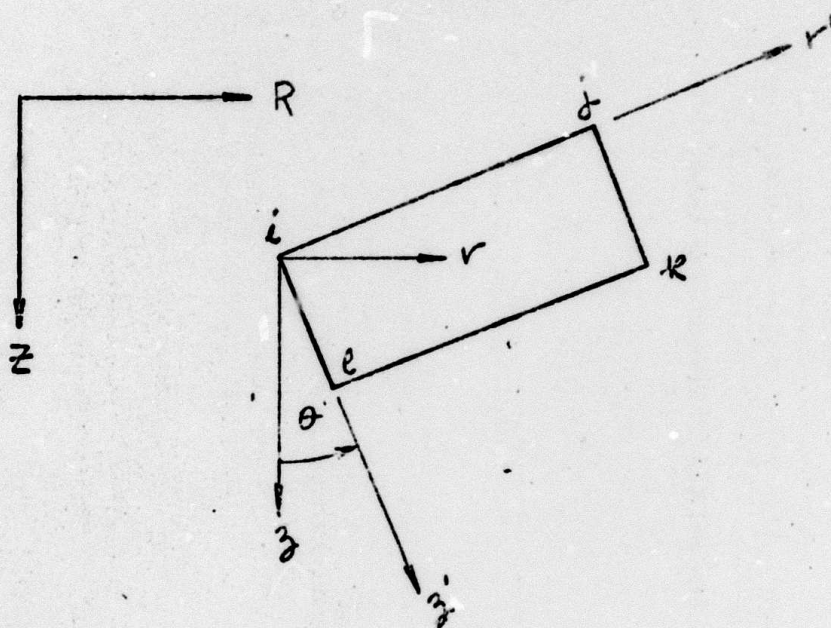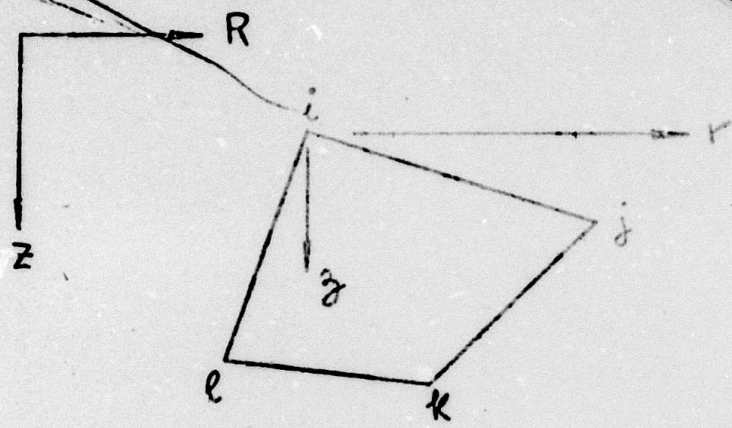$$[T] = \frac{1}{E_v}\int_v \{g\}\{g\}' dV$$

Fig. A.1 General Triangular Element

Fig. A.2   General Rectangular Element

(a) Original Coordinates
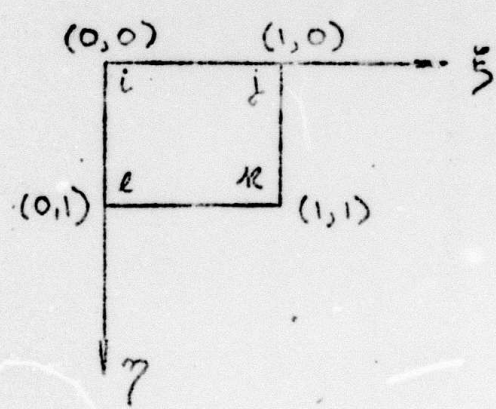
(b) Transformed Coordinates

Fig. A.3 .General Quadrilateral Element

THE CITY COLLEGE of THE CITY UNIVERSITY of NEW YORK

Convent Avenue at 138th Street, New York, New York 10031

———————————

Telephone: (212) 281-0470; (212) 368-1444

The City College Research Foundation

The City College Office—Research Foundation of The City University of New York